A plasmon ruler to probe conformational transitions of single molecules in real-time

Citation for published version (APA):
Horácek, M. (2020). *A plasmon ruler to probe conformational transitions of single molecules in real-time*. [Phd Thesis 1 (Research TU/e / Graduation TU/e), Applied Physics and Science Education]. Technische Universiteit Eindhoven.

Document status and date:
Published: 30/09/2020

Document Version:
Publisher's PDF, also known as Version of Record (includes final page, issue and volume numbers)

Please check the document version of this publication:

- A submitted manuscript is the version of the article upon submission and before peer-review. There can be important differences between the submitted version and the official published version of record. People interested in the research are advised to contact the author for the final version of the publication, or visit the DOI to the publisher's website.
- The final author version and the galley proof are versions of the publication after peer review.
- The final published version features the final layout of the paper including the volume, issue and page numbers.

Link to publication

General rights
Copyright and moral rights for the publications made accessible in the public portal are retained by the authors and/or other copyright owners and it is a condition of accessing publications that users recognise and abide by the legal requirements associated with these rights.

- Users may download and print one copy of any publication from the public portal for the purpose of private study or research.
- You may not further distribute the material or use it for any profit-making activity or commercial gain
- You may freely distribute the URL identifying the publication in the public portal.

If the publication is distributed under the terms of Article 25fa of the Dutch Copyright Act, indicated by the "Taverne" license above, please follow below link for the End User Agreement:

www.tue.nl/taverne

Take down policy
If you believe that this document breaches copyright please contact us at:

openaccess@tue.nl

providing details and we will investigate your claim.

Download date: 17. Nov. 2023

A Plasmon Ruler to Probe Conformational Transitions of Single Molecules in Real-Time

Matěj Horáček

A PLASMON RULER TO PROBE CONFORMATIONAL TRANSITIONS OF SINGLE MOLECULES IN REAL-TIME

PROEFSCHRIFT

ter verkrijging van de graad van doctor aan de Technische Universiteit Eindhoven, op gezag van de rector magnificus prof.dr.ir. F.P.T. Baaijens, voor een commissie aangewezen door het College voor Promoties, in het openbaar te verdedigen op woensdag 30 september 2020 om 13:30 uur.

door

Matěj Horáček

geboren te Vyškov, Tsjechoslowakije

Dit proefschrift is goedgekeurd door de promoteren en de samenstelling van de promotiecommissie is als volgt:

Voorzitter: prof. dr. ir. G.M.W. Kroesen
1e promotor: dr. P. Zijlstra
copromotor: prof. dr. ir. M.W.J. Prins
Leden: prof. dr. P. Kukura (University of Oxford)
prof. dr. M. Lippitz (University of Bayreuth)
dr. S.C.J. Meskers
dr. ir. S. Faez (Universiteit Utrecht)

Het onderzoek of ontwerp dat in dit proefschrift wordt beschreven is uitgevoerd in overeenstemming met de TU/e Gedragscode Wetenschapsbeoefening.

The work summarized in this thesis was performed at the Faculty of Applied Physics of Eindhoven University of Technology, and was part of the research programme of the Foundation for Fundamental Research on Matter (FOM), which is part of the Dutch Research Council (NWO).

Matěj Horáček: *A Plasmon Ruler to Probe Conformational Transitions of Single Molecules in Real-Time*

A catalogue record is available from the Eindhoven University of Technology Library
ISBN: 978-90-386-5076-0

Printed by: Marek Novoměstský
Cover design by: Matěj Horáček

© Matěj Horáček 2020

Dedicated to my family

for being with me despite being far away

SUMMARY

A PLASMON RULER TO PROBE CONFORMATIONAL TRANSITIONS OF SINGLE MOLECULES IN REAL-TIME

Biopolymers such as proteins and nucleic acids participate in many biological mechanisms such as catalysis, gene expression or DNA recombination. To execute their function biomolecules fold into their characteristic three-dimensional structures. Folding and refolding of biopolymers are crucial ways of regulating biological activity and have an essential role in biomolecular recognition. The life-time of a conformational state is typically seconds or longer, but the transition between two conformations occurs on microsecond timescales. The folding mechanisms are heterogeneous therefore resulting in a broad distribution of (un)folding pathways and pathtimes which cannot be observed in ensemble studies without synchronization. Therefore, the single-molecule sensitivity is essential to resolve unsynchronized processes as molecular folding and explore molecule-to-molecule differences. Full-atom simulations have predicted the folding mechanism and speed, however direct experimental proof of these predictions has not been given yet. Techniques as optical tweezers or atomic force microscopes require micron-sized beads or cantilevers applying external force on a molecule and thus precluding microsecond timescales. Traditional force-free molecular ruler based on Förster resonance energy transfer (FRET) on single molecules remains a formidable challenge due to the photophysics of fluorescent labels.

In this thesis, we propose a different approach based on plasmonic particles to probe biomolecular folding on microsecond timescales and at zero-force conditions. A small gold nanosphere is tethered to a larger gold particle by a molecule of interest, which herein is single stranded DNA (ssDNA) sequence forming a hairpin structure. The conformational change of the molecule modulates the interparticle distance resulting in a shift of the plasmon resonance. Plasmon rulers require no specialized equipment but can be probed on existing dark-field microscopes equipped with a fast camera. The layout of the thesis is as follows:

i. In the first part of the thesis we study the functionalization of gold nanorods with thiolated ssDNA at the single-particle level. We exploit the sensitivity of the plasmon resonance to the local refractive index induced by ssDNA binding using single-particle spectroscopy. We find that the ssDNA coverage varies considerably from particle-to-particle, beyond the expected variation due to Poisson statistics. Interestingly, the functionalization process itself is unexpectedly heterogeneous and we report rate constants varying by almost an order of magnitude from particle-to-particle. This strong heterogeneity could not be explained by the particle size dispersion alone. Instead, we attribute the dominant origin of the kinetic heterogeneity to variations in the effective charge on the particle surface.

ii. In part two we further explore the process of nanoparticle functionalization using quantitative single-molecule interaction kinetics to count the absolute number of ligands on the surface of individual particles. By analysing the waiting-time between single-molecule binding

events we quantify the particle functionalization both accurately and precisely for a large range of ligand densities. We observe significant particle-to-particle differences in functionalization which are dominated by the particle-size distribution for high molecular densities, but are substantially broadened for sparsely functionalized particles. Time-dependent studies showed ligand reorganization on long timescales drastically reducing the heterogeneity, a process that has remained hidden up to now in ensemble-averaged studies.

The work done in first and second part provides an understanding of interactions of gold nanoparticles with DNA molecules. The given results yield insight into the DNA functionalization process at the single particle level, and highlight that significant particle-to-particle heterogeneity has to be taken into account in applications of functional particles. Importantly, our work provides a direct route for quantification and optimization of coupling protocols. The obtained knowledge on ssDNA functionalization was then applied to assemble DNA-linked nanodimers to study conformation dynamics.

iii. The third part of the thesis focuses on a numerical study combining Brownian dynamics with electromagnetic simulations to model the optical signal of the plasmonic nanoruler. We find that the temporal resolution is not limited by shot noise but rather by the diffusion of the tether particle that introduces fluctuations of the optical signal. Integration times of 1 μs can be achieved, providing the capability to identify transition paths at the single-molecule level in real-time. The proposed method offers a unique opportunity to study molecular conformational dynamics in real-time and compare measurements to full-atom simulations, where computational demands limit the simulation time.

iv. The final part of the thesis focuses on delivering a method to experimentally assemble the plasmonic rulers consisting of nanorod-nanosphere heterodimers interconnected by a ssDNA hairpin. We probe the assembly process and the consequential hairpin switching dynamics using an optical scattering microscopy on dozens of dimers simultaneously with a resolution of tens of milliseconds. We observe dynamic behavior that we classify based on the characteristic timescales in the autocorrelation function. Further we extract dwell times in the open and closed molecular states for individual rulers and found them to be exponentially distributed in line with the single-molecule switching behavior. Their corresponding mean dwell times show an excellent agreement with theoretical predictions for a hairpin with a stem-region of 10 nt used here. For the right function of the plasmonic rulers it is particularly challenging to suppress non-specific interactions between the different components in the system, and to obtain yield controlled monovalent functionalization of nanoparticles with molecular ligands as the current molecular coupling protocols are not yet developed well enough.

CONTENTS

1 INTRODUCTION 1

1.1 MOLECULAR FOLDING 1
1.2 SINGLE-MOLECULE METHODS TO STUDY MOLECULAR FOLDING 4
  1.2.1 Force spectroscopy 5
  1.2.2 Electrical methods 6
  1.2.3 Single-molecule fluorescence 7
  1.2.4 Tethered particle motion 7
  1.2.5 Accessible timescales 8
1.3 THIS THESIS 9
  1.3.1 Structure of the thesis 10

2 OPTICAL PROPERTIES AND APPLICATIONS OF PLASMON RULERS 13

2.1 INTRODUCTION 14
2.2 OPTICAL PROPERTIES OF ISOLATED PARTICLES 15
2.3 OPTICAL PROPERTIES OF PLASMON RULERS 17
2.4 PLASMON RULERS TO PROBE CONFORMATIONAL DYNAMICS 20
  2.4.1 Conformational changes induced by molecular binding 21
  2.4.2 Conformational dynamics 26
2.5 CHALLENGES AND PROSPECTS 28

3 HETEROGENEOUS KINETICS IN THE FUNCTIONALIZATION OF SINGLE PLASMONIC NANOPARTICLES 31

3.1 INTRODUCTION 32
3.2 MATERIALS AND METHODS 33
  3.2.1 Sample preparation 33
  3.2.2 Experimental setup 33
  3.2.3 Hyperspectral microscopy 34
3.3 RESULTS: END-POINT PLASMON SHIFTS 36
  3.3.1 Effect of chemical conditions 36
  3.3.2 Particle-to-particle variations 37
3.4 RESULTS: KINETICS 41
  3.4.1 Dynamic plasmon shift of individual nanoparticles 41
  3.4.2 Extraction of kinetic parameters 42
  3.4.3 Particle-to-particle variations in kinetics 45
3.5 CONCLUSION 47

4 SINGLE-MOLECULE QUANTIFICATION OF NANOPARTICLE FUNCTIONALIZATION 49

4.1 INTRODUCTION 50
4.2 METHODS 52
  4.2.1 Accuracy and precision of the method 52
  4.2.2 Data post-processing 55
4.3 RESULTS 58

    4.3.1 Specificity of DNA hybridization 58
    4.3.2 Heterogeneous particle functionalization 59
    4.3.3 Contributions to inter-particle heterogeneity 59
    4.3.4 Tuning the number of functional groups 61
    4.3.5 Ligand reorganization at long timescales 62
  4.4 CONCLUSION 64

5 PLASMON RULERS AS A PROBE FOR REAL-TIME MICROSECOND CONFORMATIONAL DYNAMICS 67

  5.1 INTRODUCTION 68
  5.2 METHODS AND IMPLEMENTATION 70
    5.2.1 Probability distribution of tethered particle position 70
    5.2.2 Brownian dynamics simulations 72
    5.2.3 Electromagnetic calculations 73
    5.2.4 Detected optical signal 75
  5.3 RESULTS 76
    5.3.1 Dependence on detector integration time 76
    5.3.2 Characteristic time of the dimer 78
    5.3.3 General contour length change 79
  5.4 CONCLUSION 80

6 A HETERODIMERIC PLASMON RULER FOR SINGLE-MOLECULE CONFORMATIONAL DYNAMICS 83

  6.1 INTRODUCTION 84
  6.2 ASSEMBLY OF A HETERODIMERIC PLASMON RULER 85
    6.2.1 Anti-fouling against nanoparticle-nanoparticle interactions 87
    6.2.2 Anti-fouling against nanoparticle-DNA interactions 89
    6.2.3 Specificity of hairpin conjugation 91
    6.2.4 Complete dimer assembly 93
  6.3 HAIRPIN DYNAMICS 94
  6.4 CONCLUSION 98

7 CONCLUSION AND OUTLOOK 101

  7.1 SUMMARY OF THIS THESIS 101
  7.2 CHALLENGES AND FURTHER RESEARCH 103
    7.2.1 Quantified and specific particle functionalization 103
    7.2.2 Heterogeneous plasmonic response 104
    7.2.3 Improved data analysis 104
    7.2.4 Effect of volume exclusion forces 105

8 REFERENCES 107

9 APPENDICES 125

LIST OF ABBREVIATIONS

AFM	atomic force microscope
BEM	boundary element method
BSPP	bis(p-sulfonatophenyl)phenylphosphine
CCD	charge-coupled device
CMOS	complementary metal oxide semiconductor
CTAB	cetyltrimethylammonium bromide
CV	coefficient of variation
DBCO	dibenzocyclooctyne
DDA	discrete dipole approximation
DNA	deoxyribonucleic acid
dsDNA	double stranded DNA
EGFR	epidermal growth factor receptors
EMCCD	electron multiplying charge-coupled device
FDTD	finite-difference time-domain
FOV	field of view
FRET	Förster resonance energy transfer
MC	Monte Carlo simulations
MD	molecular dynamics
MMP3	metalloprotease 3
MPTMS	3-mercaptopropyltrimethoxysilane
mRNA	micro - ribonucleic acid
NMR	nuclear magnetic resonance
NPoF	nanoparticle on a metallic film
PAINT	point accumulation for imaging in nanoscale topography
PBS	phosphate-buffered saline
PEG	polyethylene glycol
qPAINT	quantitative PAINT
RNA	ribonucleic acid
ROI	region of interest

SAM	self-assembled layer
SLD	superluminescent diode
smFRET	single-molecule Förster resonance energy transfer
SNR	signal-to-noise ratio
SPR	surface plasmon resonance
ssDNA	single stranded deoxyribonucleic acid
STORM	stochastic optical reconstruction microscopy
TEM	transmission electron microscopy
TPM	tethered particle motion
XPS	X-ray photoelectron spectroscopy

1 INTRODUCTION

1.1 Molecular folding

Biomolecules such as proteins and oligonucleotides are the workhorses of cellular function[1] as they participate in many biological mechanisms such as catalysis, gene expression or metabolism. After expression, these biopolymers fold into their characteristic three-dimensional structure, and some undergo conformational changes in their folded form in response to temperature, pH, ionic strength, or ligand-binding.[2–4] Good examples are oligonucleotide aptamers that change their conformation upon binding to a ligand and thereby control on-going biological reactions.[5,6] Overall, folding and unfolding of biopolymers are crucial ways of regulating biological activity[7] and have an essential role in biomolecular recognition.[8] Mechanistic understanding of protein folding and conformational dynamics is therefore key to understanding molecular function, and has great potential impact in molecular biophysics, biochemistry, and medicine.

Visualizing molecular folding and unfolding is however a tremendous task since these transitions happen on a broad range of timescales and involve nanometre length scales.[9,10] Full-atom molecular dynamics (MD) simulations have provided structural and dynamic information required to understand the molecular folding mechanism and to establish an underlying theoretical background.[11–13] Direct experimental proof of the predictions remains however a formidable challenge.[11–15] The large gap in timescales that are accessible with MD simulations (typically microseconds and shorter) and available experimental methods (typically milliseconds and longer) has restricted their direct comparison. High computational demands limit MD simulations to reach experimental timescales.[16] In recent years optimization of the code,[17] atomistic potentials,[18] and developments in computer hardware[12,19] have enabled microsecond simulation times, and thus resolve multiple (un)folding events on several proteins.[20]

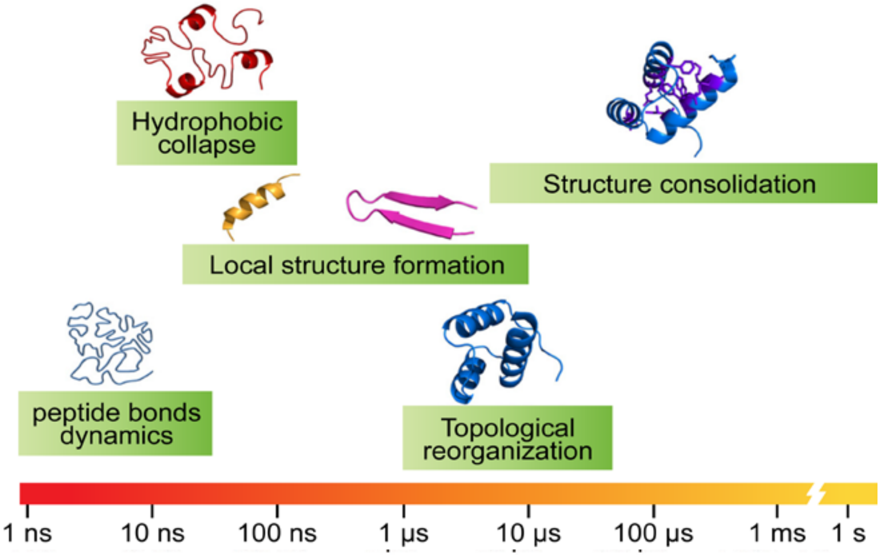

Figure 1.1: Scheme showing the timescales associated with the various structural events that cooperatively take place in protein folding reactions. Figure adapted from the reference.[34]

Figure 1.1 shows schematically the diversity of timescales that have been extracted from such MD simulations for a range of molecular folding processes. One of the most important mechanisms responsible for molecular conformational changes is hydrophobic collapse. Unfolded polypeptides randomly collapse to shield hydrophobic sites from the surrounding polar solvent (often water). The hydrophobic collapse of a molecule happens in the order of 10-100 ns, and thus is considered to be the fastest folding-related process.[21] This initial molecular collapse due to hydrophobic interactions enables further compaction of molecular structure due to electrostatic and van-der-Waals interactions, and hydrogen bonds. The interactions result in formation of local structures which subsequently transform into secondary structures like α-helices and β-strands. This complex conformational reorganization happens at a broad range of timescales of 10 ns – 10 μs. Specifically, the formation of a single α-helix was directly observed to happen in ~150 ns using time-resolved infrared spectroscopy combined with temperature jump experiments on a protein ensemble.[22,23]

Reorganization of these secondary-structure elements into their tertiary structure is a slower process because breaking of pre-formed bonds is necessary to adopt the right conformation of the protein. Frieden et al.[24] found such conformational rearrangements at timescales of several microseconds using a combination of fluorescence self-quenching and correlation spectroscopy on a molecular ensemble. Formation and closure of molecular loops is an important mechanism responsible for this reorganization. The closing of loops was indeed found to happen at timescales of several microseconds using absorption spectroscopy combined with laser-induced denaturation on a solution of proteins.[25]

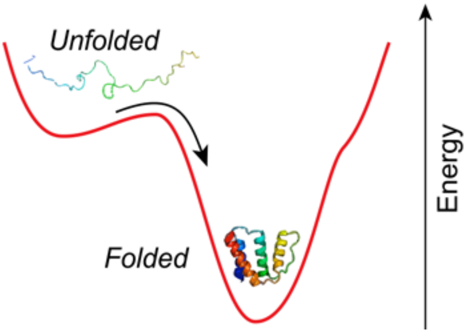

Figure 1.2: Schematic of a two-state protein transition barrier-crossing from the unfolded to the folded configuration.

The complex molecular transition processes cooperatively enable a biomolecule to fold upon itself to produce a specific 3D structure which is capable of performing relevant biological functions. From the energy landscape point of view the molecular folding can be understood as a two-state barrier crossing process (Figure 1.2).[26] The unfolded molecule undergoes a transition over a free energy barrier into the folded state with a certain folding rate and passage time.[26] Transition path times for proteins are expected to depend on their amino acid sequence,[27,28] and increase with the length of their polypeptide backbone.[29–31] The same holds for other molecules like DNA and RNA of which transition path times are determined by sequence complementarity and length.[32]

For a barrier-crossing process the folding transitions occur extremely fast but only rarely. In general, the energy landscape for molecular folding is funnelled towards its native 3D structure but may include local energy minima. This makes the folding process heterogeneous, thus an individual unfolded molecule can form its biologically active structure by means of many different strings of conformational changes (Figure 1.3). Based on this picture biomolecules are thus expected to show a broad distribution of folding and unfolding pathways and their respective transition times.[33]

The importance and consequences of the heterogeneous molecular folding and conformation on biological processes are yet unanswered questions. Experimental progress has been limited due to the heterogeneous nature of molecular folding. The life-time of a conformational state is typically seconds or longer, but the transition between two conformations involves barrier crossing that occurs on microsecond timescales. Considering many individual conformational states of a single molecule and thus many possible transition pathways one obtains a broad distribution of transition times.

To experimentally approach molecular transitions the field has relied for many years on ensemble measurements, where many molecules are monitored simultaneously. The folding transition of each molecule however does not start at the same time unless synchronized by an external stimulus like laser-induced heating.[34] The following transitions are then usually monitored by differential absorption, fluorescence spectroscopy, nuclear magnetic resonance (NMR) or surface plasmon resonance (SPR) on timescales of nanoseconds to milliseconds.[34] Monitoring an ensemble of molecular transitions however yields averaged results without any insight into intramolecular differences.

Resolving individual (un)folding pathways and their heterogeneity therefore requires a single-molecule method that gives access to a broad span of detectable timescales. Recent technological advances in single-molecule techniques make it possible to study and manipulate molecules one at a time, measure distributions of molecular properties, and characterize the kinetics and thermodynamics of biomolecular processes and reactions.

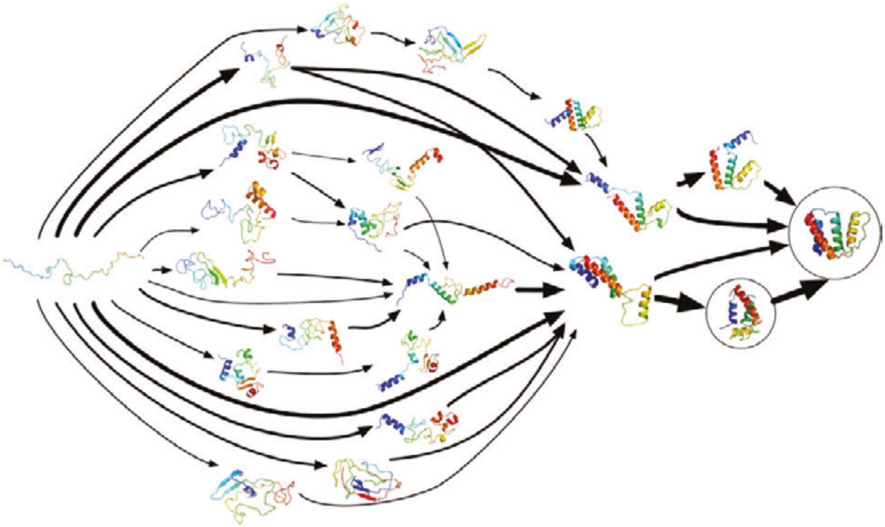

Figure 1.3: Illustration of the predicted heterogeneous molecular folding wherein a protein progresses from an unfolded polypeptide (on the left) toward a fully folded and functional protein (on the right) via a multitude of possible routes. Figure adapted from.[33]

1.2 Single-molecule methods to study molecular folding

To understand the mechanisms underlying molecular conformational transitions, biophysical methods and instruments have been developed that provide information on biomolecular structure and biomolecular interactions. Starting with ensemble techniques like X-ray diffraction, cryo-electron microscopy, Förster resonance energy transfer (FRET), fluorescence spectroscopy, SPR or NMR, all of which provided critical information on molecular structure, affinities, and biomolecular activity.[35,36] Recent technological advances however opened up a possibility to investigate such properties on the single-molecule level uncovering yet hidden heterogeneities in molecular folding. Before discussing the possibilities offered by plasmonic nanostructures to probe conformational transitions in Chapter 2, we first summarize other biophysical methods that have been developed to tackle this challenge. For a detailed overview of these methods we suggest the following reviews.[37–41]

1.2.1 Force spectroscopy

Mechanical methods like atomic force microscop (AFM), magnetic, and optical tweezers, have established themselves as versatile single-molecule tools providing an unprecedented view into biomolecular folding.[38,39,42] In a typical experimental arrangement (Figure 1.4) a single molecule is sandwiched between a stationary surface and a micron-sized cantilever or bead. Mechanical forces and torques are then applied and the displacement of the probes as a function of actuation is measured to extract information like folded-state stability and binding affinities.[43–45]

Using AFM (Figure 1.4a), folding processes of small proteins were studied in real-time with a temporal resolution of microseconds by Perkin's[42,46–48] and Li's[47,49,50] group and others.[51–53] Large cantilevers however undergo substantial hydrodynamic drag when immersed in a solution, complicating the access to these short timescales particularly at forces < 10 pN.[54] These effects can be mitigated by designing smaller and stiffer cantilevers,[46] providing access to even sub-microsecond integration times.[55]

Forces and torques can also be applied using magnetic tweezers (Figure 1.4b). Starting with supercoiling of long DNA molecules,[56–58] magnetic tweezers soon advanced to detect actuated (un)folding of small proteins[59–61] and short ssDNA hairpins.[62] Magnetic tweezers work at similar temporal and force resolutions as AFM, however the method allows for multiplexing by wide-field optical measuring of multiple beads at time.[63]

Optical tweezers on the other hand sandwich a molecule between two micron-sized beads, which are both trapped in a strongly focused laser beam allowing precise manipulation and force measurements (Figure 1.4c). This approach enables a time resolution of ~5 μs with application of an external force of ~ 5 – 20 pN.[64] Neupane et al. extracted single-molecule folding pathtimes of ssDNA hairpins,[65–68] and misfolded proteins.[65,69–71] These measurements directly revealed significant heterogeneity in the (un)folding times.[72–75]

Although corrections to the presence of a large bead or cantilever in force microscopy are being developed[64] the effect of external forces on the transition pathways and their respective times remain unclear. Recently Valle-Orrero et al.[76] showed that proteins under force underwent accelerated ageing on timescales of minutes to days. The need to observe molecular folding without applying an external force has triggered the development of force-free methods.

1.2.2 Electrical methods

Electrical probes built around nanowires and carbon nanotubes are attractive because they enable real-time measurements without the need to label the molecule.[77,78] Such devices are built by multiple nanolithography steps to expose a single well-defined spot on the wire for molecular functionalization. A single molecule coupled to such a device thus acts as a defect (Figure 1.4d), and its (un)folding induces changes in the conductance or capacitance of the device.[79–81] Molecular folding was monitored at very short timescales of ~ 4 µs without applying any external force. He et al.[79] used silicon nanowires decorated by a single ssDNA hairpin (Figure 1.4d), and observed two-level signal fluctuations where the individual levels correlate with the folded an unfolded hairpin conformations. Survival times of these states are found to be heavily dependent on temperature.

Despite remarkable progress these electrical devices suffer from several drawbacks. The effect of electric current on the molecule, as well as the exact

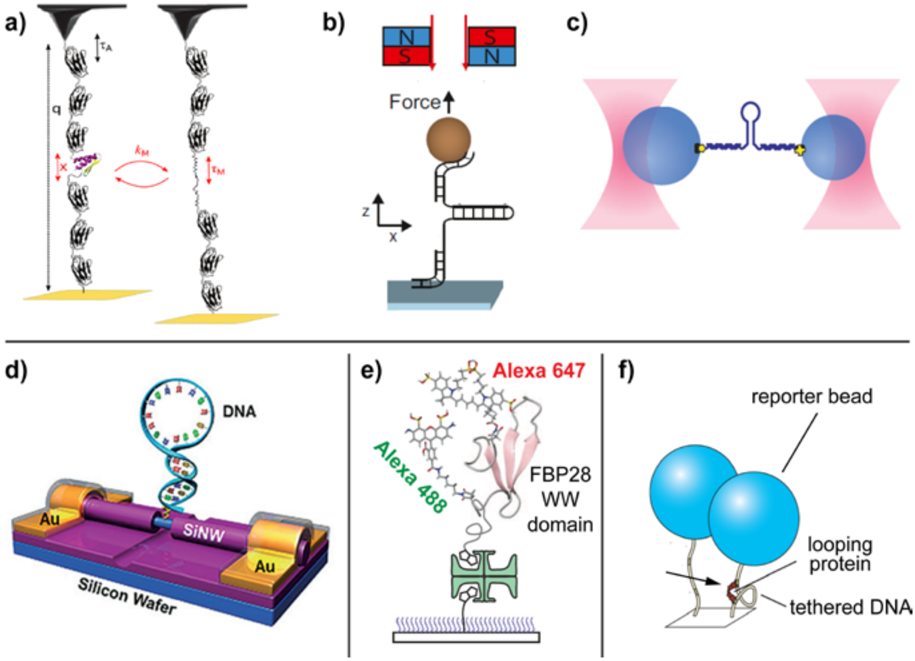

Figure 1.4: Schematics of single-molecule methods for direct dynamic measurements of molecular (un)folding. Mechanical methods including **a)** AFM, **b)** magnetic and **c)** optical tweezers[65–68] rely on large micron-sized cantilever and beads and thus an applied force. **d)** Silicon nanowire decorated by ssDNA hairpin detects changes in electrical current induced by ssDNA (un)folding.[79] **e)** Force-free smFRET detects energy transfer between fluorescent labels, which changes with inter-dye distance as the protein (un)folds.[100] **f)** Protein induced DNA looping changes the contour length of the molecular tether which is read-out from the position and motion of the tethered bead.[118]

detected molecular property are not well understood yet.[77,78] Moreover, interference from charged species in solution restricts their usage in biological environments.

1.2.3 Single-molecule fluorescence

The most-used force-free method to probe molecular folding is single-molecule Förster Resonance Energy Transfer (smFRET). Here, a "donor" and "acceptor" fluorophore are employed as a molecular ruler by strategic chemical labeling to the biomolecule (Figure 1.4e). If the dyes are spatially close (~ $1 - 10$ nm), and the emission spectrum of the donor overlaps partially with the absorption spectrum of the acceptor, the donor dye engages in non-radiative energy transfer to the acceptor dye, producing an acceptor emission signal while the donor emission is quenched.[82,83] The distance-dependence of FRET is well-understood, as the efficiency of the energy transfer scales with $1/d^6$. This permits the real-time monitoring of biomolecular folding providing information on long-lived transition states and their state lifetimes.[82,83] smFRET has been used to monitor molecular (un)folding under force-free conditions and even in living cells.[84,85] Moreover, wide-field optical microscopes allow to record thousands of single molecules giving the method an excellent throughput.

Already in late 90's smFRET was first used to study millisecond folding of ssDNA hairpin loops,[86–89] later followed by works on other molecular species like aptamers,[90,91] DNA origami,[92,93] and metabolite binding proteins.[94,95] Recently, Eaton's group used smFRET to directly observe microsecond folding pathtimes of multiple small proteins,[96–98] and ssDNA hairpins.[99] Detection of short folding pathtimes of ~10 μs was possible only after maximum-likelihood analysis of photon-by-photon trajectories[100] averaged over hundreds of single molecules.[98] Real-time monitoring is however limited to integration times of milliseconds because fluorescence saturation limits the detected photon count rate to $\sim 10^4 - 10^5$ s^{-1}. Moreover high illumination intensities increase the probability of photoblinking and photobleaching of the dye, significantly complicating signal analysis. Photobleaching also sets the limit of smFRET experimental times to only few dozens of seconds. Longer experimental times are not possible without refreshing/replacing the fluorophore.

1.2.4 Tethered particle motion

Single-molecule methods exploiting tethered particle motion (TPM) emerged in the early 1990's and provide a means to monitor conformational dynamics at short time-scales, without the application of external force, and for extended times due to the absence of blinking and bleaching. In these experiments a strongly scattering bead is attached to a substrate via a molecular tether, and properties of the tether are extracted by analysis of the position and motion of the tethered bead.[101] In the earliest experiments, live RNA polymerase activity was measured by tethering a 40 nm gold nanoparticle to a coverslip via a single DNA sequence, and its blurred motion was observed using differential interference contrast microscopy.[102] Since the 1990's, TPM has been employed to quantify DNA/RNA properties like compaction and persistence length,[103–105] and proved to be especially suitable to monitor protein-induced DNA-looping.[106–118]

TPM in the present day is an effective complementary technique to elucidate protein structure and function,[119–121] and has also developed into a promising biosensor.[122] Because the signal in a TPM sensor is generated by a modulation of the position or Brownian motion of the particle, sensitivities have been limited to milliseconds and to conformational changes of ≥ 10 nm due to the large bead size and limited spatial localization precision in an optical microscope.[123–126]

1.2.5 Accessible timescales

In summary, force microscopies like AFM and optical tweezers are well-equipped at extracting folding kinetic constants, mechanical properties and identifying partially-stable folded states. Accessible timescales of mechanical methods span over a large range from microseconds to hours, although the necessity to exert forces in the pico- to nano- Newton range limits the ability to observe the biomolecule under native conditions. Recently emerged single-molecule devices based on electrical signals offer the unique ability to achieve microsecond timescales, although the effects of electrical current on molecules

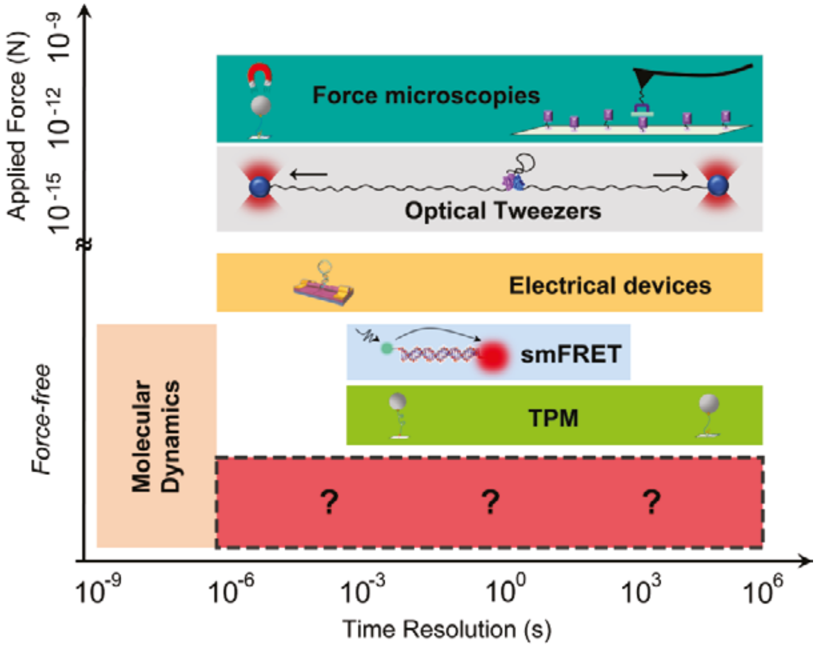

Figure 1.5: Common single-molecule techniques, shown as function of applied force (in Newtons) versus time resolution. The need of an experimental method filling the timescale gap between molecular dynamics and smFRET while still applying no external force is identified.

are not yet understood well. On the other hand, smFRET is certainly one of the most utilized force-free single-molecule techniques with well understood signal dependencies. However, the photophysical properties of organic fluorophores limit the temporal resolution to a few milliseconds, and measurement times to a few minutes at best. As non-fluorescent technique TPM allows for theoretically infinite measurement times, however its time resolution is limited by Brownian diffusion of a large tethered bead.

In Figure 1.5 we compare all mentioned techniques against each other, focusing on the required forces and achievable timescales. There is clearly a need for a single-molecule method to probe conformational dynamics with a microsecond temporal resolution without the application of an external force. An experimental method fulfilling such requirements would enable, in fact, to fill the timescale gap that exists between molecular dynamics simulations (<1 μs) and native measurements (>1 ms for smFRET), and thus to directly compare experiments with theoretical predictions.

1.3 This thesis

In this thesis we explore the use of a "plasmonic nanoruler" to probe conformational changes on single molecules. In plasmonic nanorulers a strongly localized electric field is generated by the proximity of two plasmonic structures, for example two nearby nanoparticles or a nanoparticle on a metallic film (NPoF). The molecule of interest is tethered between the individual plasmonic structures, where its folding induces modulations in spacing between the structures giving detectable plasmon shifts.

We will see that such a nanoruler system indeed mimics a daily used ruler nevertheless with the optical response which is highly sensitive to gap spacing in the range of 0 – 30 nm. Plasmonic nanoruler systems can be conveniently monitored in a standard far-field optical microscope, and do not require any near-field probes or electrical connects. The high scattering cross section of a plasmonic particle warrants photon count rates far exceeding those for single fluorescent dyes, while their photostability enables long observation times. Our proposed implementation of plasmonic nanorulers will possibly enable:

i. *Observation times of hours:* The optical response of plasmonic nanorulers does not blink or bleach, enabling observation times that are only limited by the stability of the microscope. We will use this capability to probe many subsequent transition paths on the same single molecule repetitively.

ii. *Real-time measurements:* The optical response of plasmonic nanorulers is stable, bright and not easily saturated. This, in principle, allows for probing plasmon shifts with microsecond integration times, which matches the biologically relevant timescales of molecular folding.

iii. *Force-free method:* Using the confined Brownian diffusion of a very small particle means no net external force is applied on the (un)folding molecule of interest. This will provide the unique opportunity to investigate molecular conformational changes at their native conditions.

iv. *Medium-range molecular ruler*: Similarly to smFRET the plasmonic nanorulers resemble a molecular ruler, of which sensitivity spans in range of 0-50 nm depending on the dimensions of the employed nanoparticles.

1.3.1 Structure of the thesis

In Chapter 2 we summarize the theory behind particle plasmons and their hybridization in order to create a plasmonic ruler. We give examples of current applications of plasmonic nanorulers and discuss key advances in the field in recent years. To be able to practically design a functional plasmonic nanoruler system based on DNA-linked nanoparticles we develop several experimental, signal processing, and theoretical characterization methods in the following chapters.

In Chapter 3 we study the functionalization of gold nanorods with a thiolated ssDNA at the single-particle level. We exploit the sensitivity of the plasmon resonance to the local refractive index induced by ssDNA binding using single-particle spectroscopy. We characterize the kinetics of ssDNA functionalization and compare the relative densities of ssDNA on the surface of nanoparticles for different chemical conditions.

As the absolute coating density (i.e. the number of molecules per particle) cannot be assessed using plasmon sensing as in Chapter 3, in Chapter 4 we present a method based on quantitative single-molecule interaction kinetics to count the absolute number of ligands on the surface of individual particles. By analyzing the waiting-time between single-molecule binding events we quantify the particle functionalization both accurately and precisely for a large range of ligand densities.

The work done in Chapters 3 and 4 provides a quantitative understanding of the functionalization of single particles. In Chapter 5 we then investigate the performance of the proposed plasmonic nanorulers in terms of the accessible length- and time-scales by combing Brownian dynamics simulations with electromagnetic modelling. We numerically calculate the trajectory of a tethered nanoparticle and the ensuing plasmonic optical signal. These simulations show the possibility to reach microsecond integration times and thus monitor transition paths in real-time.

Finally, in Chapter 6 we assemble a plasmonic ruler that will give access to single molecule folding by conjugating small nanospheres to a single nanorod using a ssDNA hairpin. We observe dynamic behavior which we classify based on the characteristic timescales in the autocorrelation analysis. We further extract the dwell times in the open and closed molecular states, and find them to be exponentially distributed in line with single-molecule switching behavior. Although we clearly detect ssDNA hairpin switching in the signal, it is exceptionally challenging to suppress non-specific interactions between the different components in the system.

The thesis is concluded by identifying the main challenges to be yet overcome, followed by future prospects. We hope to inspire the reader about the potential of plasmonic nanorulers for dynamic single-molecule studies, and critically evaluate its advantages and disadvantages compared to other single-molecule techniques.

2 OPTICAL PROPERTIES AND APPLICATIONS OF PLASMON RULERS*

In Chapter 1 we highlighted the biophysical approaches available to probe conformational dynamics of single molecules. This chapter summarizes the development of plasmon rulers following early experiments on tethered particle motion mentioned in Chapter 1. It gives a brief theoretical overview of the optical properties of plasmon rulers, and describes recent applications of these systems to probe conformational dynamics.

** Parts of this chapter are included in a review "Plasmonic Assemblies for Real-time Single-molecule Sensing", Small, submitted 2020.*

2.1 Introduction

The discovery of the strong interaction of noble metal structures with light led to the development of an emerging and fast-growing research field, plasmonics. The collective oscillations of electrons, so-called plasmons, and their coupling with photons gives rise to strong scattering and absorption by these particles. Humans have used plasmonics without knowing the underlying mechanism from ancient Roman times, where colloidal gold and silver particles (Figure 2.1a) were used to color glass. The first scientific report dealing with the preparation of colloidal plasmonic particles dates back to 1857 to Michael Faraday.[127] Since then a tremendous progress has been achieved in the fabrication and manipulation of nanometer-sized objects of various materials, shapes, and structures.

Classically, the metal nanoparticle can be seen as a lattice of heavy positive ions and an electron gas composed of free conduction electrons. Driven by an external electromagnetic field (light), the conduction electrons shift against the ions generating a restoring Coulomb force, resulting in harmonic oscillations of the electrons. For particles much smaller than the wavelength of the light, electron oscillations are confined by the nanoparticle‘s boundaries and all conduction electrons oscillate collectivelly.[128]

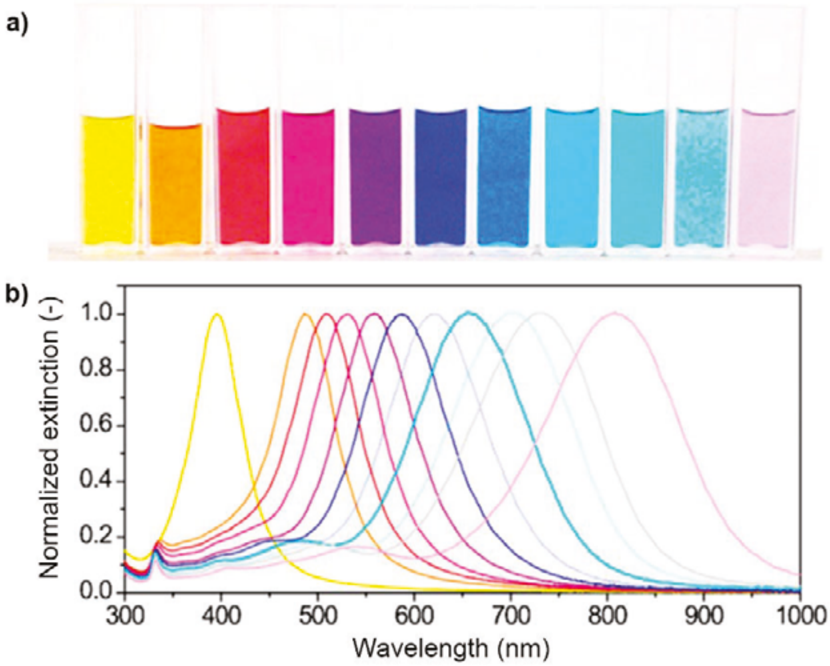

Figure 2.1: Variety of colors of plasmonic nanoparticles. **a)** Solutions of silver nanoparticles (nanoprisms) with varying sizes and **b)** their corresponding extinction spectra. Figure adapted from.[129]

The presence of a plasmon induces a strong interaction of the particle with incoming light resulting in a frequency dependent scattering and absorption cross section. In addition, a strongly enhanced electromagnetic field in the close vicinity of the particle is induced when the particle is illuminated with a wavelength near the plasmon resonance. For the most common plasmonic materials – gold and silver – the plasmon resonances occur at visible-NIR wavelengths of 400 – 1000 nm depending on the shape and size of the particle (Figure 2.1b)[129] making them compatible with standard optical microscopes.

2.2 Optical properties of isolated particles

The simplest example to illustrate the physics of a plasmon resonance is for a spherical particle in a homogeneous environment (Figure 2.2a). The scattering and absorption of light can then be analytically solved using Mie theory.[130] An insightful simplification to first order, termed *the dipole approximation*, can be made for nanoparticles much smaller than the wavelength of light.[131] The polarizability $\alpha(\omega)_{\text{sphere}}$ of a metallic nanosphere in the dipole approximation is given by[128]

$$\alpha(\omega)_{\text{sphere}} = 3V\varepsilon_0 \frac{\varepsilon(\omega) - \varepsilon_{\text{m}}}{\varepsilon(\omega) + 2\varepsilon_{\text{m}}}, \qquad 2.1$$

where V is the volume of the sphere, ε_0 is the vacuum permittivity, $\varepsilon(\omega)$ and ε_{m} are the relative permittivities of the metal and of the medium, respectively. The extinction cross section then follows from $\sigma_{\text{ext}} = \sigma_{\text{abs}} + \sigma_{\text{sca}}$, with the extinction and scattering cross sections given by[128]

$$\sigma_{\text{ext}} = \frac{k}{\varepsilon_0} \text{Im}[\alpha], \text{ and} \qquad 2.2$$

$$\sigma_{\text{sca}} = \frac{k^4}{6\pi\varepsilon_0^2} |\alpha|^2 , \qquad 2.3$$

where k is the wavevector in the medium.

Importantly, the resonant condition occurs when the real part of the denominator is zero ($\text{Im}[\varepsilon(\omega)] = -2\varepsilon_{\text{m}}$). While the magnitude of the optical response is volume dependent, the frequency of plasmon resonance is (in the dipole approximation) determined purely by the nanoparticle material and the dielectric environment, ε_{m}, in which it is immersed. For instance, according to the dipole approximation, gold nanospheres with diameters between 10 and 50 nm in water exhibit a single dipolar plasmonic mode at about 520 nm, whereas the dipolar plasmonic mode for silver occurs at about 400 nm.[132–135]

Interesting behavior arises when we break the particle spherical symmetry by elongating the particle into an ellipsoid. In the dipole approximation the broken symmetry can be accounted for by incorporating a depolarization factor into the polarizability equation.[128] Assuming that the ellipsoid is alligned with the excitation field (*i.e.* the principal axis frame), the polarizability equation takes following shape:[128]

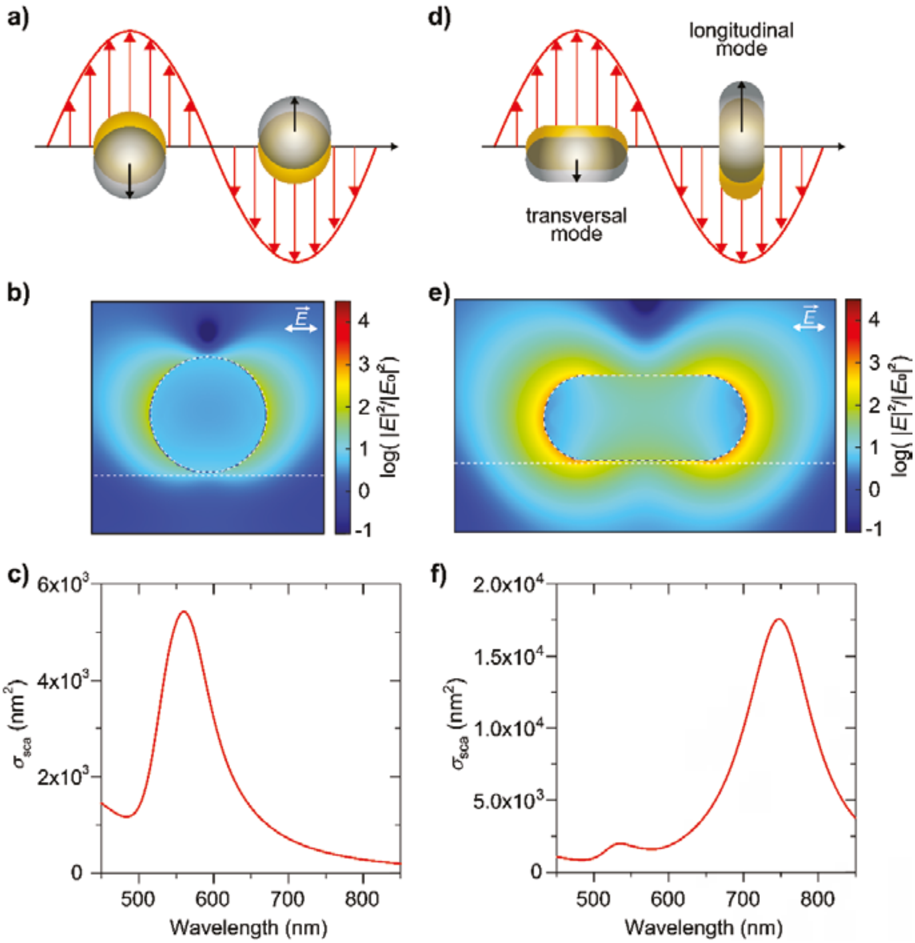

Figure 2.2: a) Schematic showing the effect of an incident electromagnetic field on the electron cloud in a spherical metal nanoparticle. **b)** Near-field intensity enhancement $|E|^2/|E_0|^2$ for a 80 nm gold sphere on a glass substrate (excited at 560 nm with horizontal polarization, calculated using the boundary element method). **c)** Far-field scattering spectrum for this configuration. **d)** Schematic showing two different plasmon modes, transverse and longitudinal, excited by perpendicular polarizations. **e)** Near-field intensity enhancement for a gold nanorod of 55 nm in diameter and 140 nm in length on a glass substrate. The rod is excited at 745 nm with horizontal polarization corresponding to the longitudinal mode. **f)** Orientation-averaged far-field scattering spectrum of the gold nanorod. The transversal plasmon occurs at 530 nm and the longitudinal is significantly red-shifted to 745 nm.

$$\alpha(\omega)_{\mathrm{x,y,z}} = \varepsilon_0 V \frac{\varepsilon(\omega) - \varepsilon_{\mathrm{m}}}{L_{\mathrm{x,y,z}}(\varepsilon(\omega) - \varepsilon_{\mathrm{m}}) + \varepsilon_{\mathrm{m}}}. \qquad 2.4$$

The depolarization factor $L_{\mathrm{x,y,z}}$ depends on the ellipsoid ellongation (defined by the eccentricity e), and for the ellipsoid ellongated along x-axis is given as

$$L_{\mathrm{x}} = \frac{1-e^2}{e^2}\left(\frac{1}{2e}\ln\left[\frac{1+e}{1-e}\right] - 1\right), \; L_{\mathrm{y}} = L_{\mathrm{z}} = \frac{1-L_{\mathrm{x}}}{2}. \qquad 2.5$$

The optical response of a nanorod therefore exhibits two plasmon resonances (Figure 2.2d). The transversal mode is associated with electron oscillations perpendicular to the long axis, and the red-shifted longitudinal mode corresponds electron oscillations along the long axis.[128] In the small-particle limit the resonances are again independent on particle volume, however the longitudinal resonance strongly depends on the nanorod‘s aspect ratio ($AR = 1/e$).[136,137] This strong dependence of the longitudinal plasmon wavelength on aspect ratio allows one to tune the resonance to the near-infrared, away from the interband transitions in gold.[138] This results in a reduction of Ohmic losses and thus a higher quality factor and stronger near-field enhancement, as illustrated in Figure 2.2.[139,140]

As seen intuitively in Equations 2.1 and 2.4 the optical response of a plasmonic particle is determined by the particle material and shape, but also by the dielectric function of the local environment.[131,141] This originates fom the fact that the near-field associated with the plasmon penetrates the medium near the particle (Figure 2.2b,e) and induces polarization charges. This makes the plasmon resonance not only sensitive to the presence of biomolecules[142] [143] but also results in a strongly modified optical response when a second particle or a polarizable interface is nearby. These assemblies exhibit substantially larger near-field enhancements in the gap region, and the coupling between the structures induces large (gap-spacing dependent) modulations of the optical response. In the next section we describe the optical properties of these assemblies of particles and summarize how they have been used as a ruler.

2.3 Optical properties of plasmon rulers

A pair of small spherical nanoparticles immersed in a homogeneous medium with dielectric constant ε_{m} can be approximated analytically using the electrostatic approach. Following the notation in Gluodenis et al.[144] the particles are considered oscillating point dipoles with a given center-to-center distance d.[144] In such a case, the electric dipole moments of individual particles in their respective local electric fields $\vec{E}_{1,2}$ are given by $\vec{\mu}_{1,2} = \alpha_{1,2}\varepsilon_{\mathrm{m}}\vec{E}_{1,2}$, where $\alpha_{1,2}$ are the polarizabilities of nanoparticles. As d increases to infinity, $\vec{E}_{1,2}$ approaches the incident light field $\vec{E}_0$. If the particles are in close proximity, the electric field felt by one nanoparticle depends on both the incoming field and the field arising from the second particle. The total polarizability of the pair of spheres α' is then given as

$$\alpha(\omega)' = \frac{\overrightarrow{\mu_1} + \overrightarrow{\mu_2}}{\overrightarrow{E_0}\varepsilon_{\mathrm{m}}} = \\ = \frac{\alpha_1(\omega)\left(1 + \alpha_2(\omega)\frac{g}{d^3}\right) + \alpha_2(\omega)\left(1 + \alpha_1(\omega)\frac{g}{d^3}\right)}{1 - \alpha_1(\omega)\alpha_2(\omega)\left(\frac{g}{d^3}\right)^2}. \qquad 2.6$$

In this approximation, the value for g is derived from the dimer‘s orientation in the polarized excitation field (see values of g in Figure 2.3a) and identify the bonding or anti-bonding modes.[144–146] Coupling the dipoles in phase results in a strong near-field enhancement and far-field radiation, whereas coupled dipoles oscillating in quadrature result in zero net-dipole moment for a pair of qual particles. It is works by the Nordlander, Stockman, and García de Abajo groups, to name a few,[131,146–149] that have shown this plasmon hybridization can be understood similarly to molecular orbitals.

It is important to emphasize that the electrostatic approach neglects multipole plasmon modes.[144] Additionally, the plasmon hybridization between particles of different shapes is more complicated and often numerical methods are essential in their understanding. Methods for numerical calculation of electromagnetic fields, such as finite-difference time-domain (FDTD),[152–154] discrete dipole approximation (DDA),[155,156] and boundary element method (BEM),[150,151,157,158] are well developed for plasmonics, are available as commercially accessible toolboxes, and have been reviewed extensively before.[159,160]

In close analogy to a metal particle dimer, a particle on a metallic film exhibits similar optical features. Strongly enhanced near-fields are also generated in the gap between the particle and the surface leading to large spectral shifts that depend on the particle-film spacing.[131,161] The close proximity of a highly-polarizable metal substrate breaks the symmetry of the dielectric environment surrounding the nanoparticle, and the particle plasmon couples to the free electrons in the metallic film. This results in a “mirror“ image dipole in the film, thus inducing additional plasmonic modes (Figure 2.3d-f).[131,161–163] Research groups have modeled these NPoF systems via the same numerical methods (i.e. – BEM and FDTD), and it has also been described using a circuit model.[164]The strong dependence of the optical response on the gap spacing has sparked practical applications of plasmonic dimers as a molecular ruler, similar to biophysical uses of FRET. Whereas a classical FRET molecular ruler follows a $1/d^6$ distance dependence, the distance dependence of plasmonic coupling follows ~$1/d^3$ for both the nanoparticle and NPoF systems considered here (Figure 2.4). This allows the molecular ruler based on plasmonic nanostructures to be applied to longer distances of up to ~ 30 nm. The Baumberg and Smith groups have demonstrated this ruler-like spacing dependence

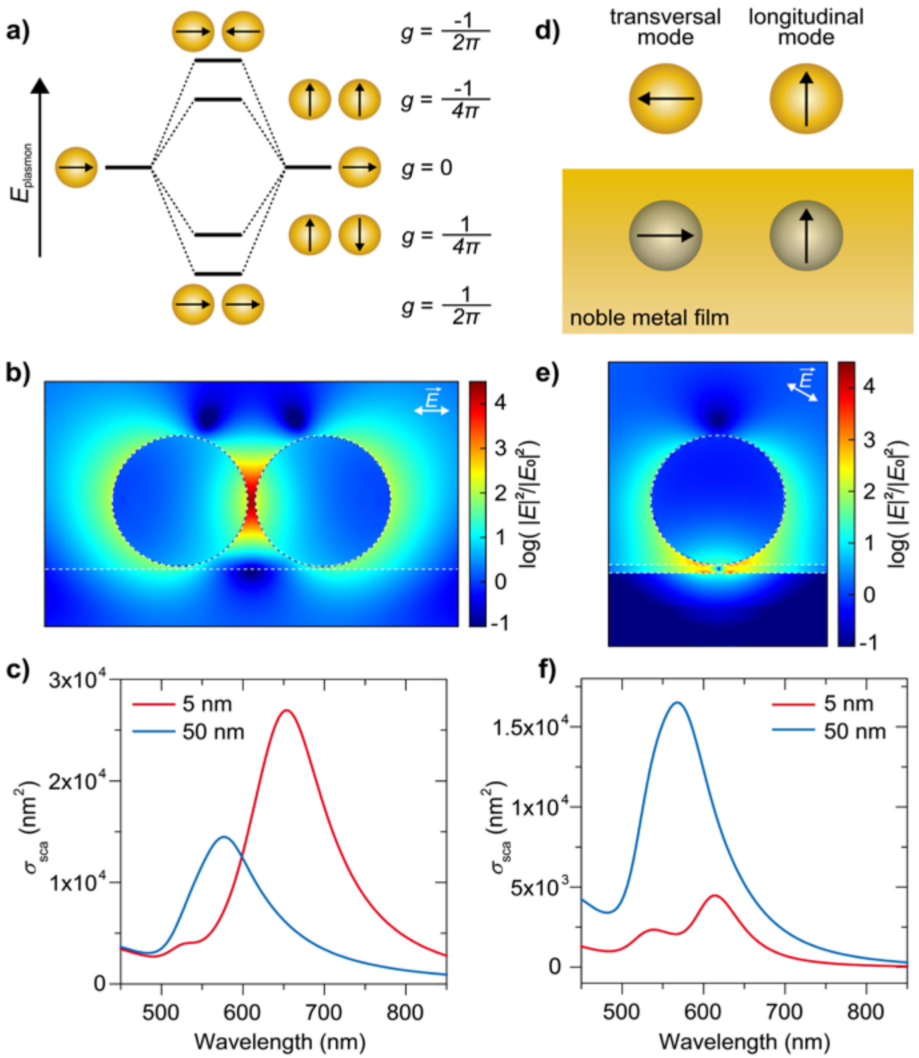

Figure 2.3: a) Scheme of particle plasmon hybridization in a homodimer of spheres, and the corresponding energy levels. **b)** Near-field intensity enhancement near a pair of 80 nm gold spheres separated by 5 nm excited at 650 nm with horizontal polarization. **c)** Far-field scattering spectra for the pair of gold spheres separated by 5 and 50 nm. **d)** Scheme of plasmon hybridization for a spherical particle above a metal film. The particle plasmon induces a mirror image in the metal film giving two distinct modes depending on incident polarization. **e)** Near-field intensity enhancement for a gold sphere above a gold film (thickness of 45 nm) excited at 615 nm at an angle of 70°. **f)** Scattering spectra for the sphere above the gold film for nanorulers of 5 and 50 nm. All examples shown in this figure are numerically calculated using the boundary element method.[150,151]

in NPoF systems. In these studies, the gap spacing was created with polymer layering,[165,166] molecular spacers with precise carbon chain lengths,[167,168] or gradual oxidation of the metal surface,[169] permitting spectral measurements of single nanoparticles at controlled spacings above a metal film. Similarly, early demonstrations of the molecular ruler technique with nanoparticle dimers were shown by Sönnichsen et al.[170] and Reinhard et al.[148] where two gold nanospheres were linked via double-stranded DNA and optical spectra of the dimer reflected this rigid, ruler-like spacing.

Apart from numerical investigations as outline above, the optical properties of individual plasmonic nanoparticles and their assemblies are routinely monitored using standard laboratory microscopes and spectrometers with single-particle resolution.[143,171–174] In principle, the detection scheme of choice then depends on what spectral property is investigated: extinction, absorption, or scattering. Spectroscopy can be performed in brightfield by comparing the transmitted light intensity by a particle to a reference (background) value.[175] Alternatively, the background can be eliminated by employing darkfield microscopy using e.g. a combination of a dark-field condenser and a low-NA objective,[171] or by spatial modulation of the sample combined with lock-in detection.[176] More complex schemes have been employed using pump-probe spectroscopy relying on a change of transmitted or reflected light intensity induced by a (modulated) pump excitation.[177,178] For a detailed description of optical particle detection techniques and methods, we would like to refer the reader to recent review articles. [143,171–174]

2.4 Plasmon rulers to probe conformational dynamics

Extraordinary favorable ratio between scattered signal and volume of plasmonic nanoparticles makes them ideal candidates to be applied in TPM measurements. In this single-molecule technique, a particle is connected to a solid surface via a molecular tether, and properties of the tether are obtained by analysing the position and motion of the particle. We discussed the

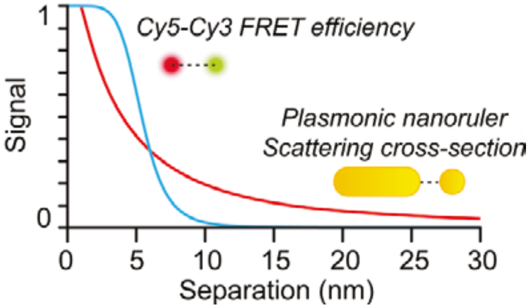

Figure 2.4: Distance-dependence comparison between a common FRET pair, Cy3-Cy5, (red) and the normalized shift of the bonding plasmon resonance in a sphere-sphere dimer (blue). Like a nanoparticle dimer, a NPoF system also approximately follows a ~ $1/d^3$ distance dependence.

TPM method in detail in Section 1.2, and here we mainly emphasize that TPM has been developed into an effective technique to elucidate protein structure and function,[119–121] and a promising biosensor.[122] However, the use of relatively large particles limits the accessible timescales to milliseconds. In addition, conformational changes of the tether are usually extracted by either (1) extracting the relative position of the particle with respect to the microscope's focal plane, or (2) by determining changes in the diffusion coefficient of the particle due to changes in the length of the tether. Both approaches are limited in accuracy and reliably detect changes in tether length of 10 nm and more.

The desire to observe smaller and faster conformational changes triggered the interest in a plasmonic readout. In such implementations a plasmonic nanoparticle is tethered to another plasmonic species and the assembly's plasmon wavelength and/or intensity is monitored using optical microscopy. This system resembles *a plasmonic molecular ruler*, and it provides the ability to measure short distal changes that traditional TPM systems cannot access in range of 0 – 30 nm. Groups invoking plasmonic nanorulers with short biomolecular tethers have already demonstrated success in real-time tracking of telomerase activity,[179] sensing by aptamer-target binding,[180] measuring multivalent antibody binding landscapes,[181] and tracking single protein conformational dynamics in real-time.[182]

As outlined in the previous section the early work on plasmonic nanorulers has focused on the influence of material composition, geometry, and gap spacing on the optical properties. With increasing understanding of these novel materials, the field has turned to exploiting their optical properties in applications. Specifically, plasmonic assemblies featuring a small gap between two particles, or between a particle and a film show exquisite sensitivity to gap spacing as shown in Figure 2.3. This sensitivity has been exploited to detect conformational changes of an interconnecting tether molecule. This conformational change can be induced either by binding of an analyte, or by the presence of multiple metastable conformations of the tether. Here we describe the history of both applications, focusing on advances in the past 5 years. We refer the reader to Ray et al. for a review of progress in the field before 2013,[183] and to Qian et al. for a review that focuses on material aspects of actuatable plasmon rulers.[184]

2.4.1 Conformational changes induced by molecular binding

Plasmonic nanorulers have been exploited to detect molecular binding events by incorporating a linker molecule that functions as a recognition element. Upon binding of target analyte, the time-averaged gap spacing is modulated resulting in a shift of the plasmon resonance. Initial studies have focused on the modification or cleavage of the linker by enzymes such as EcoRV restriction enzyme,[185,186] RNAse,[187] caspases,[188,189] and telomerase.[184] Herein particle dimers were assembled from colloidal solution using methods pioneered by Mirkin[190,191] and Alivisatos[192,193] resulting in assemblies with well-controlled stoichiometry linked by a single molecule of DNA or RNA. Reinhard et al. used double-stranded DNA as a linker, with a sequence that is cleaved by EcoRV restriction enzymes.[185] They monitored hundreds of particle dimers in a wide-field optical microscope and extracted the cleavage kinetics and the bending of DNA prior to cleavage. Later they extended the approach to study the kinetics of RNA cleavage by RNAse.[187] They observed transiently stabilized RNA sub-populations at increased spermidine concentrations, indicating that spermidine stabilizes certain weak secondary and tertiary structural elements in the RNA.[187] Qian *et al* extended the approach by monitoring the kinetics of the extension of the linker DNA by the enzyme telomerase.[179] Long time-scale observation showed that telomerase activity in different cells could be studied at single-molecule level.[179]

Other groups assembled particle-dimers and higher-order assemblies using peptide linkers to monitor their cleavage by caspases. Jun et al. continuously monitored trajectories of caspase-3 activity in live cells for several hours, providing sufficient time to observe early-stage caspase-3 activation.[189]

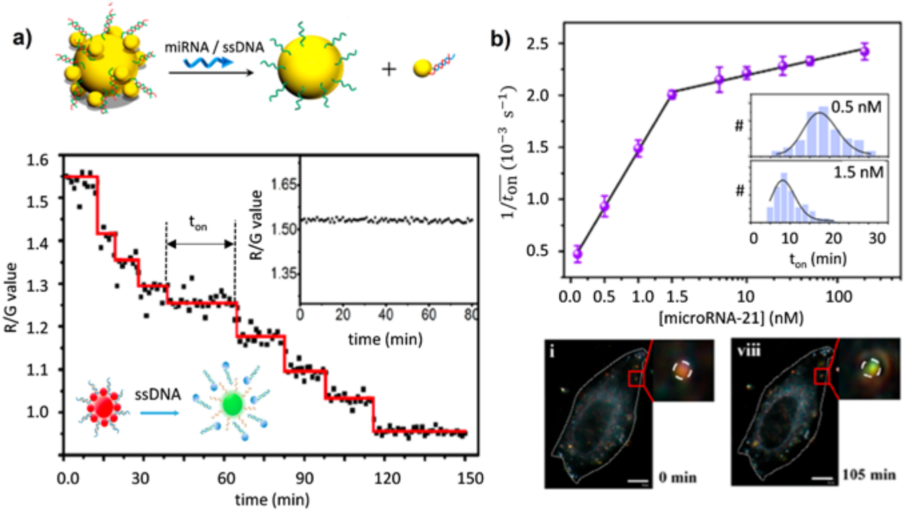

Figure 2.5: a) Detection of DNA-mediated toe-hold exchange. Core-satellite particles are assembled busing double-stranded DNA with a toehold as the interconnecting molecule. When the connecting strand is displaced by a complementary strand from solution, a single satellite particle will detach for each event leading to a stepwise blueshift of the plasmon resonance of the assembly. Reprinted with permission from Ref.[194] © 2018, American Chemical Society. **b)** The same principle can be used to detect micro-RNA, where the time between events t_{on} is Poisson distributed as shown in the inset. The mean waiting time scales inversely with the mRNA concentration. The brightness and chemical inertness of plasmonic particles also enabled the quantification of this process in living cells (bottom) providing a method to quantitate mRNA concentration. Adapted with permission from Ref.[200] © 2014, Nature Publishing Group.

Later Tajon et al. used peptide-linked dimers to study caspase activity in cell lysate.[186] They compared caspase activity in healthy and cancerous cell lines, and found that plasmonic nanorulers provide an improved dynamic range and 2 – 4 fold higher sensitivity compared to fluorescent approaches.

Plasmonic nanorulers were also used to study the dynamics of DNA interaction-mechanisms such as toe-hold exchange,[194] DNA hybridization,[195–198] and protein-DNA interactions,[199] see Figure 2.5. The dynamics of these reactions can be followed over time using e.g. core-satellite constructs where large core particles are linked to small satellite particles through single-stranded DNA. These assemblies were used by Li et al. to study the dynamics of toe-hold mediated strand displacement, where a single-molecule event leads to the detachment of one of the satellite particles, leading to a stepwise blueshift of the plasmon resonance of the assembly (Figure 2.5a).[194] The photostability and chemical inertness of the plasmonic particles allowed the authors to compare the dynamics of strand displacement in vitro, in cell lysate, and inside cells. They found a significant difference in the deduced second-order rate constants, indicating the impact of surrounding medium to the displacement kinetics. In another implementation, Kim *et al* used reversible association and dissociation of particle dimers inserted in a supported lipid bilayer to detect the presence of complementary DNA.[198] They applied kinetic fingerprinting to distinguish between non-specifically formed particle dimers (exhibiting a short survival time) and specifically bound dimers (long survival time), and demonstrated the detection of tens to thousands of DNA copies with single-base-mismatch differentiation capability.

Micro-RNAs (mRNA) are small non-coding RNAs that function in regulation of gene expression, and have recently been identified as a promising biomarker for cancer diagnosis and as potential drug targets. Traditionally, fluorescence-based methods are used to detect small numbers of mRNA molecules inside living cells, but also plasmonic nanorulers have emerged as a promising technology to quantify mRNA intracellularly. Detection and quantification of mRNA was achieved using two approaches: Lee et al. used DNA/RNA duplex formation to *form* particle dimers inside living cells,[200] whereas Li et al.[194] used strand-displacement to *break apart* particle assemblies (Figure 2.5). Both processes yield dynamics that is proportional to the number of complementary mRNA present in the cell, providing a means to quantitative mRNA detection.

These studies have so far focused on the formation or disassembly of plasmonic assemblies in response to molecular events. Although this generates substantial plasmon shifts that are straightforward to detect even inside cells, they do not allow for repeated interactions on the same interlinking molecule. Lee et al. overcame this issue by linking two plasmonic particles using an aptamer (i.e. a ssDNA molecule that undergoes a conformational change upon binding of an analyte).[180] They used this to monitor dynamic interactions with the enzyme matrix metalloprotease 3 (MMP3) that is secreted from mammalian cells and is involved in the breakdown of the extracellular matrix (Figure 2.6). Upon binding of MMP3 to the aptamer, the authors observed a red-shift of the plasmon of ~ 10 nm for a single MMP3, which was the result of a change in interparticle distance of ~ 7 nm. The process was fully reversible allowing for repeated detection of multiple events over time.[180]

Assemblies of metallic particles are challenging to synthesize from colloidal solutions because usually the stoichiometry can only be controlled by post-purification. Plasmonic nanorulers with very similar distance dependent properties can be achieved by particles near a metallic film (see Section 2.3). These structures have also been exploited for molecular sensing by exploiting the ability to modulate the particle-film spacing using a time-varying potential[201,202] or light intensity.[203] Nanoparticles were tethered to a gold film using molecular linkers, and the particle-film spacing was oscillated at a few hertz using an electrical potential or light cue. In the case of actuation using a potential, the electrostatic force and thus oscillation amplitude is proportional to the charge on the surface of the particle. These oscillations therefore induce a periodic shift of the nanoruler plasmon which was detected using a plasmonic imaging approach. Fang et al. used this mechanism to detect phosphorylation kinetics on single particles that were coated by a layer of peptide and exposed to kinase.[201] Shan et al. similarly used nano-oscillators to detect modulations in surface charge of the particles by analyte binding.[202]

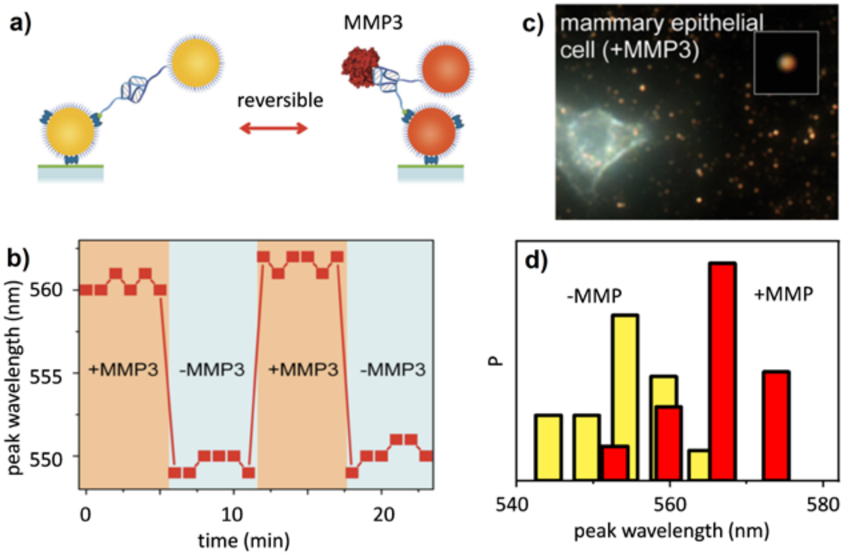

Figure 2.6: a) Schematic of a plasmonic nanoruler used to monitor repeated interactions of a protein secreted from mammalian cells (MMP3) with the interlinking molecule (an aptamer). **b)** The interactions are reversible, enabling the monitoring of repeated event son the same dimer. **c)** dark-field microscopy image of the dimer immobilized on a substrate near a cell. **d)** Plasmon shift induced by binding of MMP3 secreted from the cell. Reprinted with permission from Ref [180]. © 2015, American Chemical Society.

Chen et al. used actuation by light to heat the particles and induce a local temperature change (Figure 2.7a).[203] This results in local softening of a hydrogel sandwiched between the particle and the film, resulting in modulations of particle-film spacing. When single-stranded DNA was doped into the film, the hybridization with mRNA was detected by a change in the distance modulation caused by a modification of the mechanical properties of the material in the gap.[203] This process could be monitored over time and the kinetics

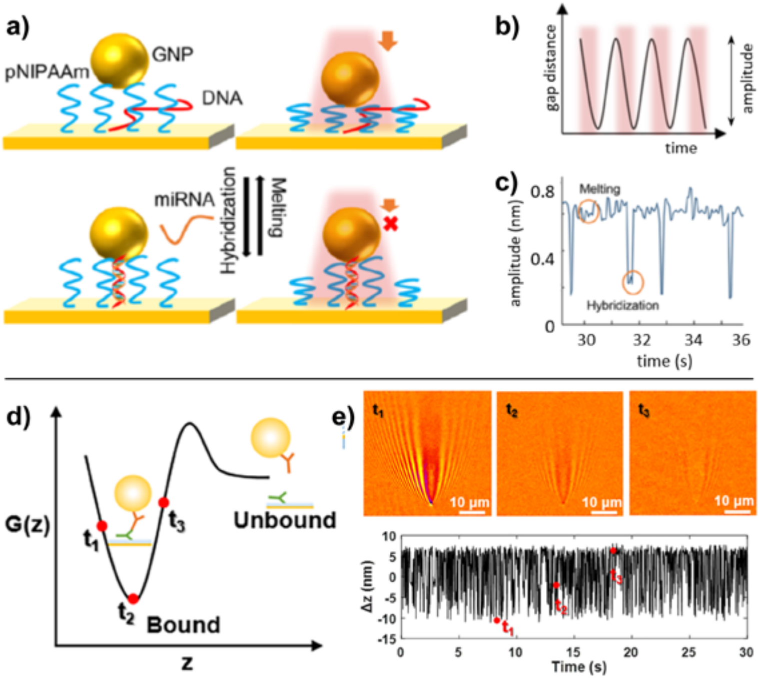
a)
pNIPAAm
GNP
DNA
miRNA
Hybridization
Melting
b)
gap distance
amplitude
time
c)
0.8
0.4
0
amplitude (nm)
Melting
Hybridization
30
32
34
36
time (s)
d)
G(z)
t1
t2
t3
Bound
Unbound
z
e)
t1
t2
t3
10 μm
10 μm
10 μm
10
5
0
-5
-10
-15
Δz (nm)
0
5
10
15
20
25
30
Time (s)

Figure 2.7: a) The use of nanoparticle-on-film systems to detect miRNA using a hydrogel film doped with complementary ssDNA. The particle-on-film system is actuated using resonant laser excitation leading to heating and local softening of the hydrogel. The ensuing reduction in particle-film-spacing leads to a plasmon shift, which is probed using scattering microscopy. **b)** Laser actuation protocol showing the sinusoidal excitation of the system, leading to variations in gap distance. **c)** Upon miRNA hybridization the mechanical properties of the film change locally leading to a change in the amplitude of oscillation. The digital nature of the signals indicate single-molecule sensitivity. Reprinted with permission from Ref [203]. © 2014, American Chemical Society. **d)** Energy barrier diagram of the three-bound states (t_1, t_2, and t_3) for single- and multi-valent antibody binding between an anti-IgG-coated nanoparticle and an IgG-coated gold film. **e)** Plasmonic imaging of the perturbed field caused by nanoparticle binding to the surface. Raw images of the three states are shown (top). Example single nanoparticle vertical position timetrace data where the three states are evident (bottom). Reprinted with permission from Ref [181]. © 2019, American Chemical Society.

of molecular hybridization and unbinding could be resolved.

Recent work by Wang et al builds on dynamic NPoF systems by distinguishing multivalent antibody interactions between IgG-coated nanoparticles and an anti-IgG-coated gold film (Figure 2.7).[181] Imaging of the plasmonic fields directly in the film reveal field perturbations in the locations where a nanoparticle is temporarily bound via IgG-anti-IgG interactions. Plasmonic image analysis determining a changing height of the nanoparticle above the film surface during binding further reveals three states in the single-nanoparticle data – nanoparticles bound to one antibody, multivalent binding to two antibodies, and then bound again to a single, but different, antibody (Figure 2.7e). Impressively, non-specific interactions, and their subtypes, are also distinguishable by kinetic fingerprinting and x,y-displacement analysis.[181]

The above detection mechanisms that relies on dynamic changes of nanoruler spacing have a distinct advantage over regular refractive sensors such as single plasmonic particles, waveguides, metal films, or nanophotonic structures. In the latter sensors, perturbation theory shows that the resonance shift depends on the overlap integral between the local electric field and the analyte. This results in a resonance shift that scales with the analyte volume and thus molecular weight of the analyte. By exploiting such a conformational change in nanoruler structures, the resonance shift is decoupled from the size of the analyte. This allows for single-molecule detection of small molecules that have remained undetectable with “traditional” refractive index sensors.

2.4.2 Conformational dynamics

Repeated conformation switching of biomolecules has particularly been studied using FRET, wherein the proximity of a donor and acceptor dye induces non-radiative energy transfer between them due to dipole-dipole coupling. FRET is a powerful technique and profits from site-specific chemical labelling, background-free imaging, and multi-color capabilities to simultaneously reveal multiple distances within a single biomolecule. One of the drawbacks of FRET that is difficult to overcome is the photophysics of the dyes that results in blinking and eventual bleaching after some tens of seconds. Monitoring conformational dynamics on long timescales is therefore not possible, but recently the distance dependent optical properties of plasmonic nanodimers have been applied for this purpose.

In 2018 Park et al. monitored single-molecule rotational dynamics of plasmonic dimers conjugated to epidermal growth factor receptors (EGFR) in live cell membranes.[204] The dimer was formed by conjugating a single nanoparticle to EGFR, which is known to dimerize in the cell membrane preceding signaling. The authors observed the orientation of the dimers as a function of time and found stochastic jumps in the dimer orientation which was attributed to a conformational change in the receptor. This method allowed not only to visualize molecular diffusion and rotation but also structural transitions of the protein during signaling.[204]

Samai *et al* synthesized dimers of gold spheres linked by a ssDNA that forms a hairpin structure (Figure 2.8a-d).[205] The DNA had several azobenzene groups incorporated in the backbone which, upon illumination, switch from a *cis*- to a *trans*-conformation. In the *cis*-conformation the azobenzene provided steric hindrance, substantially weakening the DNA interaction in the stem-region. This allowed the authors to reversibly open and close the hairpin using blue and UV light, which was characterized using single-particle dark-field scattering spectroscopy. Analyzing the plasmon peak shifts for nearly 100 dimers yielded an average interparticle distance of 15 ± 2 nm in the closed (*trans*-azobenzene) and 18 ± 2 nm in the open (*cis*-azobenzene) state. This resulted in plasmon shifts

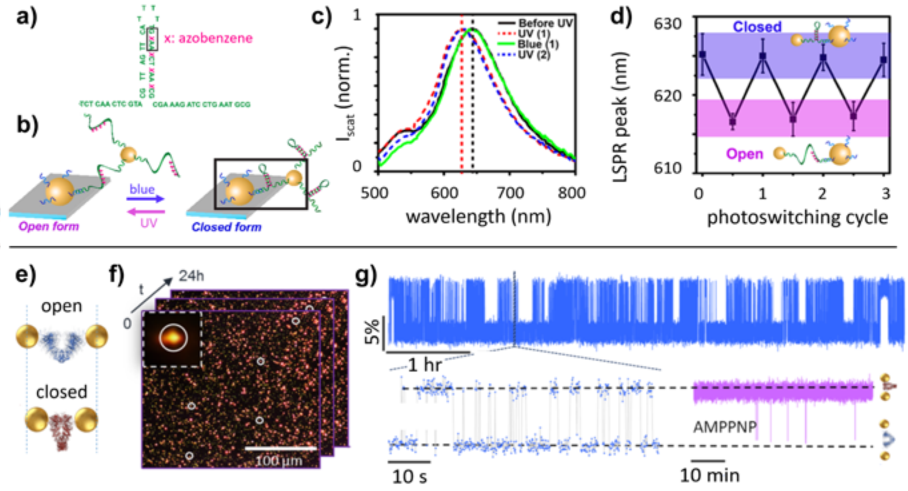

Figure 2.8: The use of metal nanoparticle dimers **a) - d)** to study photo-induced switching of DNA hybridization and **e) - g)** to study single-protein conformational dynamics. a) Two nanoparticles are connected via a hairpin with photoswitchable azobenzene moieties inserted in the stem region. **b)** Upon illumination with blue or ultra-violet light the hairpin formation can be facilitated or hindered by the isomerization of the azobenzene group. **c)** Single-dimer scattering spectra showing that the dimer's plasmon resonance reversibly shifts upon illumination. **d)** Repeated photoswitching cycles showing the stability of the structure. Reprinted with permission from Ref [205]. © 2018, American Chemical Society. **e)** Two nanoparticles connected via a single chaperone protein undergo conformational dynamics between an open and closed state. **f)** Owing to the photostability of the particle's optical response the dynamics can be followed for 24 hours in a dark-field microscope, wherein the scattered intensity is recorded over time. **g)** Repeated transitions between an open and closed conformation are observed as rapid changes in scattered intensity differing by 5%. In the presence of AMPPNP the chaperone is predominantly in the closed conformation, as expected from ensemble-averaged studies. Reprinted with permission from Ref[182]. © 2018, American Chemical Society.

of ~ 10 nm and is in agreement with numerical calculations.[205] Photoswitch-modified DNA therefore enabled the reversible modulation of the interparticle distance, allowing for the remote control of the optical properties of single dimers making use of conformational dynamics.

Conformational dynamics of a single protein were recently monitored using gold particle dimers by Ye et al. (Figure 2.8e-g).[182] They used the molecular chaperone Hsp90 as model system, which is a dimeric protein that undergoes a scissor-like conformational change upon hydrolysis of ATP. The dimers were constructed by first immobilizing well-isolated gold particles with a diameter of 60 nm. Then, a second particle was attached to the anchor particle with an Hsp90 complex bridging the two as schematically represented in Figure 2.8e. These constructs were monitored in a dark-field optical microscope, wherein conformational changes of Hsp90 were observed as distinct changes in scattered intensity.[182] The plasmon ruler traces show long dynamics never seen before by FRET: dynamics on the 1 − 10 min time scale, which were resolved because the photostability of the gold particles allowed the authors to monitor conformational dynamics for 24 hours continuously.[182] Plasmon rulers thus extend the observation bandwidth 3 − 4 orders of magnitude with respect to single-molecule FRET and enable the study of molecular dynamics on very long timescales.

2.5 Challenges and prospects

The recent examples of single-molecule plasmonic nanoruler sensors have begun to demonstrate the potential of these systems to overcome limitations of other single-molecule methods. Plasmonic nanorulers potentially provide a complementary technique to investigate biomolecular folding events for which other single-molecule techniques are ill-equipped. As demonstrated by Ye et al, exceptionally long experimental measurements (hours to days) with stable plasmonic nanoruler scattering signals can be achieved.[182] Plasmonic nanoruler systems, in fact, may fill the timescale gap that exists between molecular dynamics simulations (< 1 μs) and smFRET measurements (> 1 ms). Later in this thesis (Chapter 5) we perform detailed numerical calculations to study the potential of plasmonic nanorulers to reach microsecond integration times.

Successful implementation of dynamic plasmonic nanorulers will not be without obstacles and limitations. Synthesis and purification of specifically labelled nanoparticles is not trivial and often results in a low yield. Better shape control in nanoparticle synthesis, and quantitative control and visualization of the chemical interface of the nanoparticles are needed to improve yield, sensitivity, and response time of plasmonic nanoruler systems. A major challenge herein is the prevention of non-specific interactions between nanoparticles, biomolecules, and surfaces, which will require further developments in antifouling coatings. In next chapters we focus on establishing and quantifying various molecular coatings on gold nanoparticles in order to create functional plasmonic biosensors with controlled molecular functionalization. We design multiple theoretical, experimental, and signal processing methods to analyse the signals at single-particle and single-molecule level, and thus characterize and control interparticle heterogeneities.

3 HETEROGENEOUS KINETICS IN THE FUNCTIONALIZATION OF SINGLE PLASMONIC NANOPARTICLES[†]

In order to assemble a controlled plasmonic assembly linked by a single biomolecule we require a quantified functionalization protocol. The functionalization of gold nanoparticles with DNA has been studied extensively in solution, however these ensemble measurements do not reveal particle-to-particle differences. Here we study the functionalization of gold nanorods with thiolated single stranded DNA (ssDNA) at the single-particle level. We exploit the sensitivity of the plasmon resonance to the local refractive index to study the functionalization in real-time using single-particle spectroscopy. We find particle-to-particle variations of the plasmon shift that are attributed to the particle size distribution and variations in ssDNA coverage. We find that the ssDNA coverage varies by ~ 10 % from particle-to-particle, beyond the expected variation due to Poisson statistics. Surprisingly, we find binding rates that differ from particle-to-particle by an order of magnitude, even though the buffer conditions are identical. We ascribe this heterogeneity to a distribution of activation energies caused by particle-to-particle variations in effective surface charge. These results yield insight into the kinetics of biofunctionalization at the single particle level, and highlight that significant kinetic heterogeneity has to be taken into account in applications of functional particles. The presented methodology is easily extended to any nanoparticle coating and can be used to optimize functionalization protocols.

[†] *This chapter has been published as "Heterogeneous Kinetics in the Functionalization of Single Plasmonic Nanoparticles", Langmuir 2018, 34, 131−138.*

3.1 Introduction

Hybrid nanostructures such as bio-functionalized nanoparticles have recently emerged as versatile and programmable nanomaterials for various applications. Functionalization of nanoparticles is usually achieved using the well-known thiol-gold chemistry[206] where functional probes are provided with a thiol group at one end. Functionalization with antibodies,[142,207,208] peptides[209] and aptamers[210–212] allows metal nanoparticles to be used as biosensors.[143] Also, the functionalization with ssDNA has received considerable attention[190,213–221] driven by anticipated applications in drug delivery,[222] gene regulation,[223] plasmon-induced PCR,[224] and aptamer-based sensing.[143] Moreover, ssDNA functionalized nanoparticles offer a versatile platform to study multivalent interactions and crystal formation and allow for the straightforward tuning of affinity by modulating the number of strands and their complementarity.[225–227]

The functionality of the hybrid nanoparticles depends on the density of functional probes on the surface of the particle. Optimization of functionalization protocols has therefore received considerable attention with the aim to understand and optimize the coating density. In the case of ssDNA functionalization, dense coatings of thiolated ssDNA on gold nanoparticles were conventionally achieved using the so-called salt-aging method,[190,213–218] in which the electrostatic repulsion due to the negative charges on the gold particles and the ssDNA is gradually reduced by stepwise addition of salt over few days. Later it was shown that this process can be accelerated by orders of magnitude by reducing the pH of the employed buffer.[219–221,228,229]

Since then, several studies addressed the functionalization of gold nanoparticles with ssDNA. These studies have yielded insight into the effects of salt concentration,[230–234] buffer pH,[229,233] ssDNA sequence,[220,228,233–235] and nanoparticle size[221,236] on the kinetics of functionalization. These studies monitored the progress of the functionalization by probing the fluorescence of labelled ssDNA[219–221,229,233,234] or the shift of the plasmon resonance[237] on ensembles of nanoparticles. Particle-to-particle differences remain hidden in such ensemble studies because they are averaged out. However, such particle-to-particle heterogeneity can have a profound influence in applications of the particles *e.g.* as biosensors because the sensor response may differ between individual particles.

Here we employ single-particle spectroscopy to study ssDNA-functionalization by probing shifts of the plasmon resonance of individual gold nanorods over time. Probing plasmon shifts on hundreds of individual particles simultaneously in a wide-field optical microscope gives access to heterogeneity that has remained hidden in previous studies. We indeed find strong particle-to-particle variations in the end-point plasmon shift, which we attribute to the distribution of particle sizes present in any preparation of nanoparticles, and to the variation in nanoparticle coverage with ssDNA. Surprisingly, we find unexpectedly large particle-to-particle variations in the rate constant for ssDNA binding, even under identical chemical conditions. We propose that this heterogeneity originates from particle-to-particle differences in surface charge density. The heterogeneity we find should be taken into account when optimizing particle coating protocols, and indicates that statistical analysis of single-particle response is crucial.

3.2 Materials and Methods

3.2.1 Sample preparation

Gold nanorods were purchased from NanoSeedz and their dimensions were subsequently measured using TEM giving an average width of 19 ± 3 nm, and an average length of 69 ± 7 nm (Figure 3.1c). To firmly immobilize gold nanorods they were spin-coated onto coverslips thiolated with 3-mercaptopropyltrimethoxysilane (MPTMS, Sigma Aldrich). The density of particles on the coverslips was controlled by the concentration during spin-coating to yield 300 – 400 particles in the 130 x 130 μm^2 field of view of the microscope. Prior to ssDNA functionalization the sample was rinsed with methanol, 1 M NaCl, PBS, and milliQ water to remove loosely attached particles and residual cetyltrimethylammonium bromide (CTAB) surfactant. The sample was equilibrated in a citric acid buffer, resulting in citrate-coated gold nanorods.

The nanorods are functionalized using a reported low-pH method[219–221,228,229] with ssDNA of 50 nucleotides modified with a thiol at the 5’ end (see Table 3.1) purchased from Eurogentech. Unless stated otherwise, the concentration of ssDNA was 1 µM in citric acid buffer with a strength of 100 mM and a pH in the range of 1.7 to 9. Moreover, the analyte solution contained 1 mM of Tris(2-carboxyethyl)phosphine hydrochloride (TCEP, Sigma Aldrich) to anneal possible di-sulphide bridges. The solution was introduced in the flowcell using a syringe pump at constant flow of 100 µL/min. All experiments were executed at room temperature.

ssDNA sequence (from 5’ to 3’)	**Length**
SH - TAG ACA GTT TCA TCG GTG ACA AGA TCC ATA CGC TTC CAA TAC GCT ATC AG	50 nt

Table 3.1: The sequence of the ssDNA used in our experiments.

3.2.2 Experimental setup

A glass coverslip with gold nanoparticles was inserted in a flow cell (Warner instruments) that was mounted in a wide-field optical (inverted) microscope (Nikon Eclipse Ti).We use prism-type total-internal reflection to excite plasmons in our gold nanoparticles resulting in nearly background-free images. The light scattered by the nanoparticles is collected with a water immersion objective (Nikon Plan Apo 60x VC, NA = 1.15), and projected onto

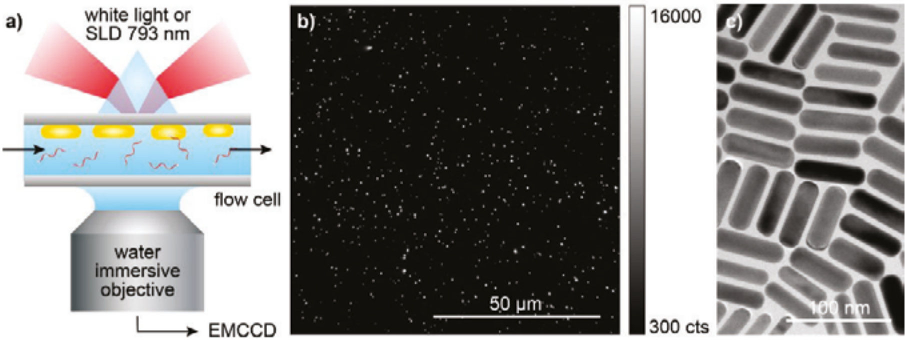

Figure 3.1: a) Scheme of the experimental setup: a coverslip with immobilized gold nanorods is mounted in a flow cell. Using prism-coupled total-internal reflection microscopy, the scattered light from the nanorods is collected by a water immersive objective and recorded onto an EMCCD camera. **b)** A typical field of view, each diffraction-limited spot represents a single nanorod, or sometimes a cluster. **c)** TEM image of a dried drop of the gold nanorods on a carbon coated copper grid.

an EMCCD camera (Andor Ixon+ 885). A simplified scheme of our dark-field imaging setup can be found in Figure 3.1a. For spectroscopic measurements we illuminated the sample with a white-light source, and spectra of individual particles were recorded by wide-field hyperspectral microscopy (Section 3.2.3). For time-dependent measurements we used a narrowband superluminescent diode (SLD) for illumination (Section 3.4.1). Figure 3.1b then shows the field of view of a typical sample, where diffraction-limited spots represent either single nanorods or sometimes clusters of particles. Each spot exhibits a different scattered intensity caused by heterogeneity in particle volume and aspect ratio, and by a different orientation of each particle in the partly polarized evanescent field.

3.2.3 Hyperspectral microscopy

White-light scattering spectra are recorded for all particles in the field-of-view at the same time using wide field hyperspectral microscopy. Individual gold nanorods are characterized by a narrow Lorentzian spectrum, allowing us to discard clusters based on the lineshape and linewidth of the spectrum.

To record white-light spectra we use a fiber-coupled laser-driven xenon white-light source (Energetiq). A series of 10 nm bandpass filters with center wavelengths ranging from 670 nm to 890 nm are sequentially introduced in the emission path of microscope, and a wide field image is captured for each center-wavelength. The scattering spectrum can then be reconstructed by determining the detected scattered intensity for each individual particle for each center wavelength. This method is particularly fast for large numbers of particles, as the data acquisition is reduced to capturing a few images only, i.e. one per wavelength band. We determined the accuracy of this method by repeated measurement of the spectra of the same particles, where we find accuracies in the plasmon wavelength and the linewidth determination of 0.5 nm and 3 meV, respectively.

The intensity scattered by the particle is calculated from the images by fitting each diffraction-limited spot in the image with a 2D Gaussian:

$$f(x,y) = I_{\mathrm{bg}} + A\exp\left[-\left(\frac{(x-x_0)^2}{2\sigma_{\mathrm{x}}^2} + \frac{(y-y_0)^2}{2\sigma_{\mathrm{y}}^2}\right)\right], \tag{3.1}$$

where I_{bg} is the background intensity in the image, x_0 and y_0 are the coordinates of the 2D Gaussian, σ_{x} and σ_{y} are the standard-deviations in the x and the y-direction, and A is the amplitude of the Gaussian. In the fitting procedure we assumed a symmetrical spot, i.e. $\sigma_{\mathrm{x}} = \sigma_{\mathrm{y}}$. The total detected intensity is then given by the volume under the Gaussian as

$$I_{det} = 2\pi A\sigma_x^2 \, . \tag{3.2}$$

To recover the scattering spectrum we correct I_{NP} for the optical response of the setup by normalizing to the experimentally determined (non-zero) white-light response of the setup $I_{\mathrm{NP}}(\lambda) = I_{\mathrm{det}}(\lambda)/I_{\mathrm{bg}}\,(\lambda)$.

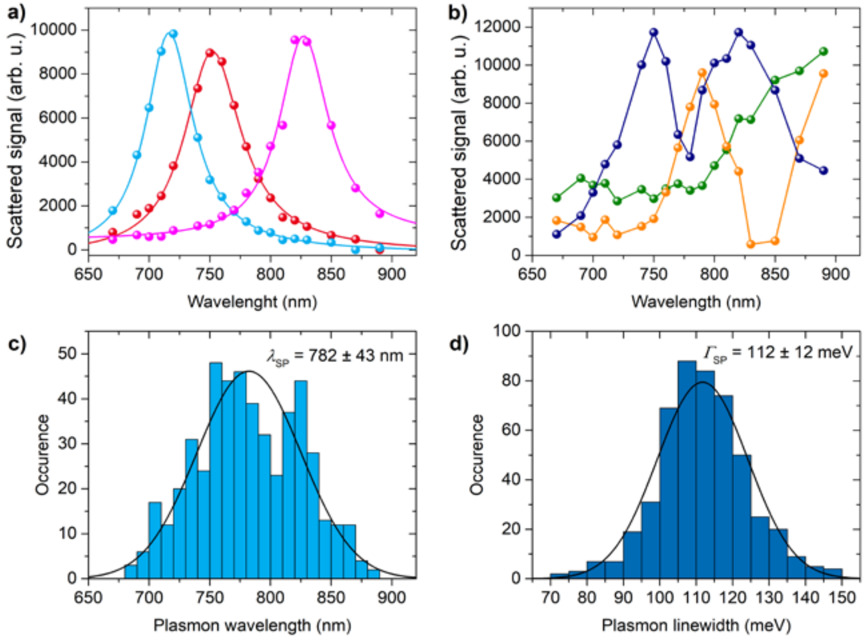

Figure 3.2: A few typical examples of spectra of single nanorods **a)** and clusters **b)** measured by hyperspectral microscopy. Histograms of plasmon wavelengths **c)** and linewidths **d)** of individual single gold nanorods both characterized by normal distributions of 782 ± 43 nm and 110 ± 12 meV, respectively.

A few examples of scattering spectra of individual single gold nanorods are shown in Figure 3.2a. We observe single and narrow Lorentzian spectra whose linewidth (Figure 3.2d) falls within the range of 110 ± 40 meV indicating single particles. Particles with a linewidth that deviates by more than 3 standard deviations from the mean are considered clusters. Taking all single nanoparticles in the microscope field of view we build a histogram of individual plasmon wavelengths (Figure 3.2c). In Figure 3.2b we also show examples of the scattering spectrum of clusters of nanoparticles, which exhibit a double peak (blue and yellow curves) or no clear peak feature at all (green curve). These clusters can easily be distinguished from the spectra of individual particles and are discarded from the further data analysis.

3.3 Results: End-point plasmon shifts

3.3.1 Effect of chemical conditions

We measured plasmon shifts of single particles in response to binding of thiolated ssDNA as a function of buffer pH for pH = 1.7, 3, 5, 7 and 9, and two different concentrations of additional NaCl of 0 M and 1 M added into a buffer. All experiments were performed in citric acid buffer of 100 mM strength. We used incubation times of 1 hour for pH 1.7 and 3 and 3 hours for pH 5, 7 and 9. Spectra of individual particles and their corresponding plasmon shifts were recorded in the same buffer before and after ssDNA functionalization. In Figure 3.3a we show two measured distributions of plasmon shifts for pH 1.7 and 5, and Figure 3.3b summarizes the obtained plasmon shifts as a function of buffer pH for two added NaCl concentrations.

We observe that for pH 5, 7 and 9 for both added NaCl concentrations the plasmon peaks show only small shifts ($\Delta SP < 5$ nm) even after 3 hours of ssDNA incubation. This suggests that the ssDNA binding is inefficient under these conditions resulting in a low coverage and therefore small plasmon shifts. At reduced pH we observe significantly larger plasmon shifts up to $\Delta SP = 15.5 \pm 2.7$ nm for pH 1.7 in combination with 1 M added NaCl.

The observed behavior can be explained by considering the effective charges of ssDNA and gold nanorods and their modulation as a function of buffer pH. The citrate present in the citric acid buffer coats the surface of the gold nanoparticles[238] with an estimated average surface coverage of approximately 45 %[238] and provides the particles with a negative zeta-potential.[239] The acid dissociation constants of citrate are $pK_a = 3.14$, 4.77 and 6.40,[240] implying that the citrate becomes protonated in the lower pH range we employ. The ssDNA on the other hand consists of a sugar-phosphate backbone ($pK_a \approx 1.4$ [241]) and bases: adenine (A) with $pK_a \approx 4.1$, cytosine (C) with $pK_a \approx 4.4$, guanine (G) with $pK_a \approx 3.2$ and thymine (T) with $pK_a \approx 9.9$.[242] The negative charge on ssDNA is mainly determined by its sugar-phosphate backbone which is deprotonated in the whole range of used pH. In the lower pH range the backbone is partially protonated therefore decreasing the net charge of ssDNA.

These considerations imply an improved efficiency of ssDNA coating at low pH due to reduced electrostatic repulsion between the citrate coated nanoparticles and ssDNA. However, even weak repulsion between solution-phase and surface-bound ssDNA will reduce the maximum achievable surface density. This intermolecular electrostatic repulsion can be partly alleviated further by adding 1 M of NaCl into the citric acid buffer, resulting in a reduced Debye length of 0.30 nm (see inset of Figure 3.3b). This is confirmed in the data, where we consistently observe larger plasmon shifts when 1 M salt is added. This modulation of the mean ssDNA coverage due to reduced electrostatic repulsion is in agreement with previously published ensemble-averaged results.[229–234]

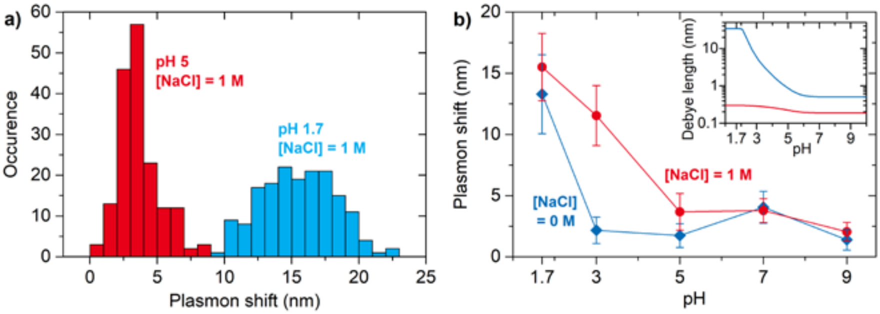

Figure 3.3: a) Two histograms of the single-particle plasmon shifts measured in a citric acid buffer at pH 1.7 and 5 with 1 M of additional NaCl. **b)** Behaviour as a function of pH. The points and error bars correspond to the mean and the standard deviation of the measured distribution, respectively. The modulation of Debye length in the buffer as a function of buffer pH and NaCl concentration is shown in the inset.[243]

3.3.2 Particle-to-particle variations

In addition to the mean plasmon shift, single-particle spectroscopy yields the width of the distribution caused by inter-particle heterogeneities. Histograms in Figure 3.3a show the full distribution of plasmon shifts measured for all particles in the field-of-view for pH 5 and pH 1.7. In both cases we observe a broad distribution of end-point plasmon shifts which can be caused by several mechanisms:

i. inter-particle variations in refractive index sensitivity,
ii. the dispersion of aspect ratios present in any preparation of gold nanorods,[244]
iii. the dispersion of particle volumes present in the sample, or
iv. particle-to-particle variations in the ssDNA coverage.

We first explore mechanism (i), the differences in particle sensitivity to refractive index change. We directly measured the bulk sensitivity of our gold nanorods by changing medium refractive index and subsequently measuring single-particle spectra. The bulk refractive index sensitivity is defined as $S_\lambda = d\lambda_{\mathrm{SP}}/dn$, where $d\lambda_{SP}$ is the change of the plasmon wavelength caused by an increase of refractive index dn of the surrounding media.[245] As shown in Figure 3.4, the difference in bulk sensitivity we find between short and long aspect ratios is in good agreement with calculations using a core-shell Mie-Gans model,[246] see Appendix 1. This increase in sensitivity for increasing aspect ratios has indeed been predicted in the electrostatic approximation[247] and was verified by comparison to numerical simulations.[245] The measured absolute values, however, are lower than the theoretical predictions due to the presence of the substrate in our experiments that shields part of the probe volume of the particles.

Further analysis of the nanoparticle sub-population that exhibits plasmon wavelengths of 750 – 800 nm gives relatively low coefficients of variation of 8 % and 6 % for the theoretical and experimental data, respectively. This implies that the heterogeneity in sensitivity is dominated by the presence of different aspect ratios in the sample, and not by different distances and orientations of the particles with respect to the substrate. The same conclusion translates to the plasmon shifts induced by ssDNA binding therefore giving negligible contributions to the inter-particle heterogeneity.

We further explore mechanism (ii), the dispersion of aspect ratios present in our sample of nanorods. In Figure 3.5a we show the correlation between the measured plasmon wavelength and the corresponding plasmon shift induced by binding of ssDNA at pH 1.7. We find a positive correlation between the aspect ratio and the plasmon shift, again showing a higher sensitivity to local refractive index for longer particles. Although we observe a correlation between aspect ratio and

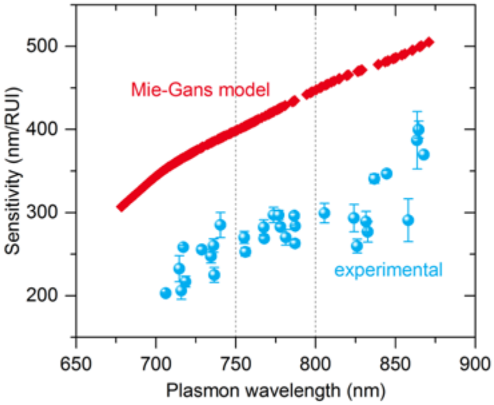

Figure 3.4: The bulk refractive index sensitivity of gold nanorods determined experimentally and using a core-shell Mie-Gans model. By considering the sub-population of nanoparticles characterized by plasmon wavelengths in the range 750 - 800 nm we extracted $\mathrm{CV}_{\mathrm{Mie}}$ = 8 % and $\mathrm{CV}_{\mathrm{exp}}$ = 6 %.

end-point plasmon shift in Figure 3.5a, there is still significant spread in the observed shifts. For particles with a plasmon resonance between 750 nm and 800 nm this residual heterogeneity is characterized by a normal distribution and its variance of $\sigma_{\mathrm{tot}}^2 = 5.2$ nm^2, see Figure 3.5b. This residual heterogeneity could therefore be due to the abovementioned mechanisms (iii) and (iv), *i.e.* the distribution of particle volumes present in the sample (σ_{vol}^2), or due to particle-to-particle variations in the ssDNA coverage (σ_{cov}^2). Assuming all variables are normally distributed the total variance is then given by

$$\sigma_{\mathrm{tot}}^2 = \sigma_{\mathrm{vol}}^2 + \sigma_{\mathrm{cov}}^2 \,. \qquad 3.3$$

We estimate σ_{vol}^2 by calculating the expected distribution of plasmon shifts using a core-shell Mie-Gans model,[246] see Appendix 1. From TEM images we find that our nanorod sample contains particles with distributions in their lengths, and widths, giving a heterogeneous distribution in particle volumes. Differences in particle volume lead to differences in end-point plasmon shift because the near-field decays on longer length-scales for bigger particles.[248] This reduces the overlap between the ssDNA coating and the near-field of the particle, resulting in smaller shifts for larger particle volumes.

We used the core-shell Mie-Gans model to estimate σ_{vol}^2 for a representative sub-population of particles (dimensions extracted from TEM images) with a calculated plasmon wavelength between 750 nm and 800 nm. By considering only a sub-population of nanoparticles and by calculating their expected plasmon shift using core-shell Mie-Gans theory we disentangle the effect of the nanorod‘s shape and size dispersion on the reported plasmon shifts. We find a minor contribution of $\sigma_{\mathrm{vol}}^2 = 0.9$ nm^2 , which implies that the ssDNA coverage varies from particle-to-particle contributing $\sigma_{\mathrm{cov}}^2 = 4.3$ nm^2.

This suggests that the heterogeneity in end-point plasmon shift is dominated by particle-to-particle differences in the absolute number of ssDNA strands. We decompose σ_{cov}^2 into two contributions,

$$\sigma_{\mathrm{cov}}^2 = \sigma_{\mathrm{Poisson}}^2 + \sigma_{\mathrm{DNA}}^2 \,, \qquad 3.4$$

where $\sigma_{\mathrm{Poisson}}^2$ represents the lower limit expected for the variance in the number of ssDNA per particle due to Poisson statistics, and σ_{DNA}^2 represents additional sources of heterogeneity.

To estimate the number of ssDNA strands functionalized to gold nanoparticles and thus its corresponding Poisson distribution over individual particles we estimate the maximum ssDNA loading of the employed particles. We base this estimate on the work by Hill et al.[236] and thus consider thiolated DNA molecules as closely-packed cones occupying the surface area of the particle. A detailed explanation of the estimation is given in Appendix 2. For ideal conditions, which is pH 1.7 with 1 M of additional NaCl, ssDNA adopts a “mushroom-like” conformation, which we approximate by a hydrodynamically equivalent sphere giving a ssDNA footprint of ~20 nm^2 for a length of 50 nt. An assembly of such ssDNA spheres then occupies the surface of the nanorod, which we correct for the presence of a substrate. We determine the maximal molecular loading for all nanorods measured with TEM, and obtained a distribution in the number of ssDNA molecules per particle of $N_{\text{max}} = 225 \pm 42$, where the standard deviation originates from the distribution of surface areas for different particles.

To find $\sigma^2_{\text{Poisson}}$ we assume a Poissonian distribution characterized by a standard deviation of $\sigma = \sqrt{\mu} = 15$, giving the coefficient of variation $CV = \sigma/\mu = 6.5\,\%$. We further assume that this Poissonian CV translates directly to a $CV_{\Delta SP}$ of the plasmon shift, in other words we assume that the average shift per molecule is a constant. This translates to a variance in the plasmon shift that is given by $\sigma^2_{\text{Poisson}} = (\overline{\Delta SP} \times CV)^2 = 0.7\,\text{nm}^2$ for the ideal conditions. The small Poisson-induced contribution demonstrates that the mean source of heterogeneity is due to particle-to-particle variations in the average ssDNA coverage. Note that the above discussion assumes that particle-to-particle variations in DNA-conformation are negligible, which is reasonable because we average over ~ 225 strands per particle. The corresponding variance $\sigma^2_{\text{DNA}} = 3.5\,\text{nm}^2$ represents a coefficient of variation $CV \approx 10\,\%$, implying that number of ssDNA strands per particle varies by ~10 % on top of the Poisson distribution.

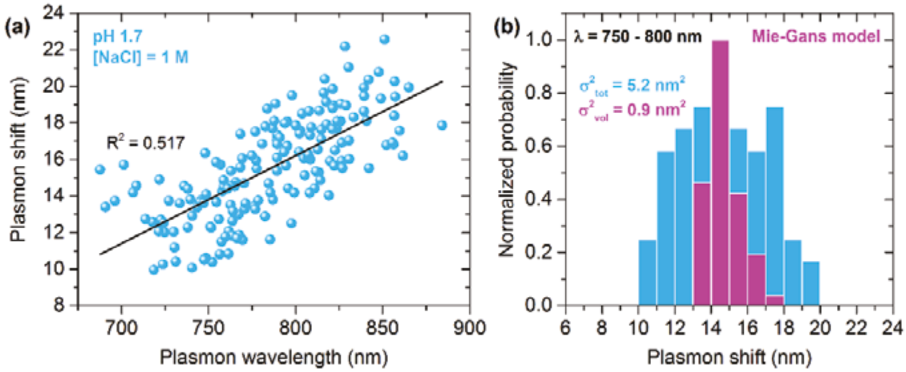

Figure 3.5: a) Functionalization-induced plasmon shifts of individual nanoparticles as a function of plasmon wavelength of individual nanorods. Data shown in this figure were recorded for buffer pH = 1.7 and 1 M of addition NaCl. The black solid line represents a linear fit to the data with $R^2 = 0.517$. **b)** Histograms of the end-point plasmon shift for the sub-population of individual nanoparticles falling in a plasmon wavelength range of 750 – 800 nm (cyan) characterized by a variance of 5.2 nm^2, and calculated plasmon shifts using a core-shell Mie-Gans model[246] for the same sub-population of representative particles whose sizes were extracted from TEM images characterized by a variance of only 0.9 nm^2.

3.4 Results: Kinetics

To further understand the functionalization process, we now focus on the kinetics of the ssDNA binding to individual gold nanoparticles. We performed measurements of dynamic plasmon shifts of single particles in response to binding of ssDNA at pH 1.7, 3, and 5, and for 0 M and 1 M additional NaCl added to the citric acid buffer.

3.4.1 Dynamic plasmon shift of individual nanoparticles

Dynamic plasmon shifts induced by ssDNA binding of individual particles were probed using a narrowband SLD ($\lambda_{\text{probe}} = 793$ nm, $P = 35$ mW, Superlum), generating a time-dependent scattered intensity that depends on the plasmon wavelength relative to the wavelength of the SLD. This dependence is highlighted in Figure 3.6a, where we show several timetraces corresponding to individual gold nanorods on the same sample. For particles with a plasmon wavelength shorter than the probe-wavelength, the red-shift of the plasmon causes an increase in the scattered signal, whereas particles with a plasmon wavelength longer than the probe exhibit the opposite behavior. There is also a third regime where the plasmon wavelength is only slightly blue-shifted compared to the probe. In that case the scattered signal first increases and as the plasmon crosses the SLD wavelength the signal decreases again (magenta line in Figure 3.6a). The overall change in scattered intensity after functionalization with ssDNA is summarized in Figure 3.6b, where we observe the aforementioned wavelength dependence.

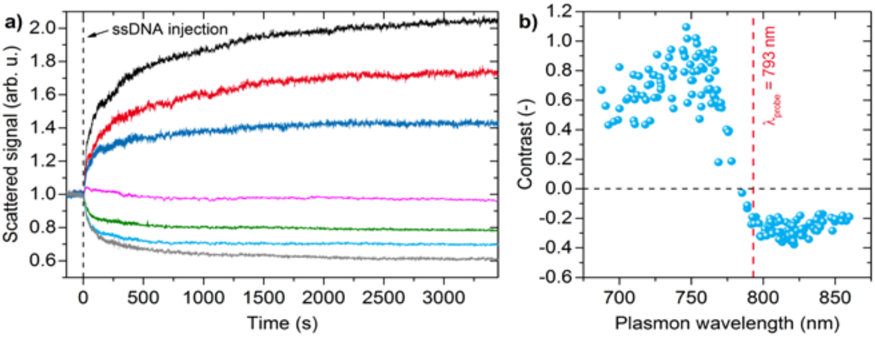

Figure 3.6: a) Timetraces of scattered intensity normalized to the initial value for seven individual nanorods. At $t = 0$ s ssDNA (1 µM in pH 1.7 citric acid buffer with 1 M of additional NaCl) is injected into the flowcell using a syringe pump at a flowrate of 100 µL/min for 3 minutes. The sign of the intensity change depends on the plasmon wavelength relative to the wavelength of the SLD probe (793 nm). **b)** Correlation between the plasmon wavelength measured by hyperspectral microscopy and the observed normalized contrast ($(I_{\text{final}} - I_{\text{initial}})/I_{\text{initial}}$), where I_{final} was measured 1 hour after injection of ssDNA. The vertical dashed line indicates the SLD's centre wavelength.

3.4.2 Extraction of kinetic parameters

To extract kinetic parameters from timetraces, we first fitted the data using a single exponential. However, this resulted in a poor fit suggesting that the binding process cannot be described by simple Langmuir kinetics. Although a multi-exponential fit results in better fitting due to the increased number of fitting parameters, it does not represent the underlying mechanism properly because it discretizes the distribution of rate constants. A better representation is given by a continuous distribution of rate constants k.

Since we expect rate constants bound to the region $0 \leq k \leq \infty$, of the possible rate constant distributions the Gamma distribution possesses a properly defined statistical mean and variance,[249] is a generalization of the conventionally used stretched exponential distribution,[250] and yields an analytical equation that can be used to fit the timetraces. The probability density function (pdf) of the Gamma distribution $p(k)$ is given by:[251]

$$p(k) = \frac{1}{\mathbb{\Gamma}(\alpha)\theta^{\alpha}} k^{\alpha-1} e^{-\frac{k}{\theta}}, \qquad 3.5$$

where α and θ are the shape and the scale parameter of the Gamma distribution ($\alpha, \theta > 0$), and $\mathbb{\Gamma}(z)$ is the Gamma function. The shape and the scale parameters are related to the mean and the standard deviation of the $\mathbb{\Gamma}$ distribution by $\langle k \rangle = \alpha\theta$, and $\sigma = \sqrt{\alpha\theta^2}$, respectively. For the specific case of a Gamma distribution of exponentials the overall signal decay I_{decay} can be expressed in a relatively simple form[251] containing only two parameters α and θ:

$$I_{\text{decay}} = \int_0^{\infty} p(k)\, e^{-kt}\, \mathrm{d}k = \frac{1}{(1+\theta t)^{\alpha}}. \qquad 3.6$$

However, the time-dependent shift of the plasmon wavelength is in our measurements probed using the narrowband SLD. Therefore, to simulate the measured timetrace we approximate the nanorods longitudinal plasmon by a single Lorentzian and its shift over time is given by the gamma distribution of rates. The energy of the plasmon E_{SP} (in eV) as a function of time is then given by:

$$E_{\text{SP}}(t) = E_{0\text{i}} + \Delta E \left(1 - \frac{1}{(1+\theta t)^{\alpha}}\right). \qquad 3.7$$

where $\Delta E = E_{0\text{f}} - E_{0\text{i}}$, with E_{0i} the (measured) initial plasmon energy (in eV) and $E_{0\text{f}}$ the plasmon energy at $t \to \infty$. Eqn 3.7 is then used as the center energy of a Lorentzian curve that represents the scattering spectrum, which is evaluated at the probe wavelength and normalized to the initial value at $t = 0$ s. This yields a model for the normalized intensity scattered by the particle at the wavelength of the SLD probe, given by

$$I_{\mathrm{SP}}^{\mathrm{norm}}(t) = \frac{\left(E_{\mathrm{probe}} - E_{0\mathrm{i}}\right)^2 + \left(\frac{1}{2}\Gamma'_{0\mathrm{i}}\right)^2}{\left(E_{\mathrm{probe}} - E_{\mathrm{SP}}(t)\right)^2 + \left(\frac{1}{2}\Gamma'_{0\mathrm{i}}\right)^2}, \qquad 3.8$$

with $E_{\mathrm{probe}} = 1.58$ eV (= 793 nm) the probe energy and $\Gamma'_{0\mathrm{i}}$ the (measured) initial plasmon linewidth. We find that this model yields a very high fitting accuracy (mean $R^2 = 0.97 \pm 0.08$) with only three fitting parameters. We also fitted the data with a stretched exponential by inserting corresponding probability density function into Eqn. 3.8. In general we find the stretched exponential fits our data worse than the Gamma distribution as represented by higher R^2 values, which is why we choose this model to fit our data in Figure 3.7.

Figure 3.7a shows two typical examples of timetraces at pH 1.7 and pH 5, fitted with Eqn. 3.7 and Eqn. 3.8. At pH 1.7 we find mean rate constants that are orders of magnitude faster than at pH 5, in line with previous ensemble studies.[219,220,229] However, for all particles studied we find a broad gamma distribution of rate

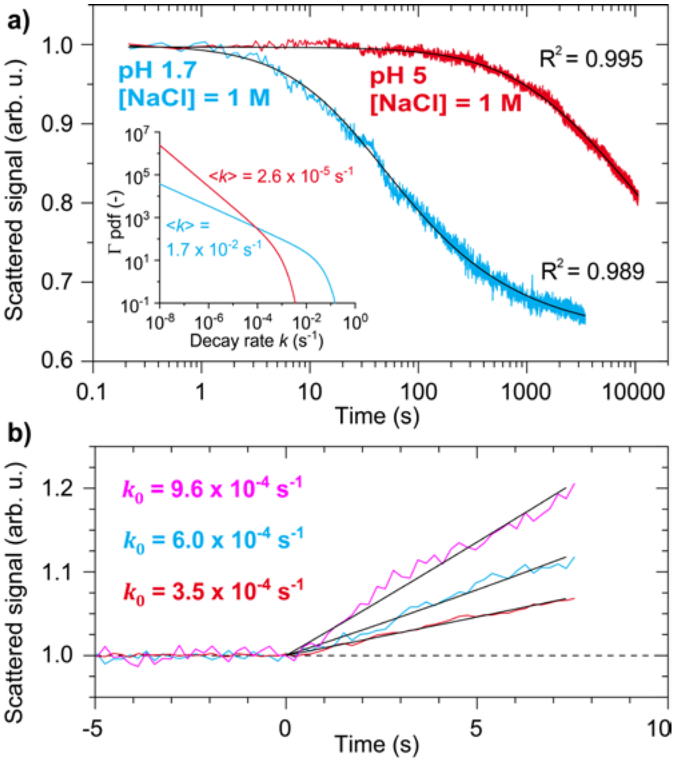

Figure 3.7: a) Gamma distribution fits to recorded timetraces on a logarithmic scale for two individual single nanorods. In the inset the corresponding Gamma probability density functions are shown together with the mean kinetic rates. **b)** Three examples of timetraces of individual single gold nanorods on the same sample with corresponding fits for their initial rates.

constants given by the corresponding Gamma probability density functions plotted in the inset of Figure 3.7a. The broad distribution of rate constants for each particle is observed under all pH and salt conditions and is attributed to ssDNA crowding on the surface of the particle. This causes a gradual decrease in rate constant as the reaction progresses due to the onset of steric hindrance, hydrophobic effects, and electrostatic repulsion.[234]

Although the gamma distribution fits indicate that the binding-rate reduces over time, they do not allow for easy comparison between different conditions because they require accurate fitting at long times to recover the low rate constants. This is especially challenging at pH > 5, where signals are low and the time to saturation is on the order of hours. We therefore turn to the initial rate constant at $t = 0\,s$, where these effects do not play a role. This initial regime is characterized by a plasmon energy that shifts linearly in time, given by

$$E_{\mathrm{SP}}(t) = E_{0\mathrm{i}}(1 - k_0 \cdot t)\,, \tag{3.9}$$

where k_0 is the initial rate constant and the minus sign indicates a shift to lower energies.

We fitted the timetraces of individual particles with Eqn. 3.8, with $E_{\mathrm{SP}}(t)$ given by Eqn. 3.9. A few examples of these fits are shown in Figure 3.7b. We observe that ssDNA binding starts at the exact same time for all probed nanoparticles, however the extracted initial rate constants differ significantly from particle-to-particle, even if the chemical conditions are identical. Figure 3.8a shows the mean and standard deviation of these lognormal distributions as a function of pH for 1 M of additional NaCl. In line with earlier ensemble studies[219–221,228,229] we find that the mean rate constant depends strongly on pH due to the aforementioned modulation of electrostatic forces.

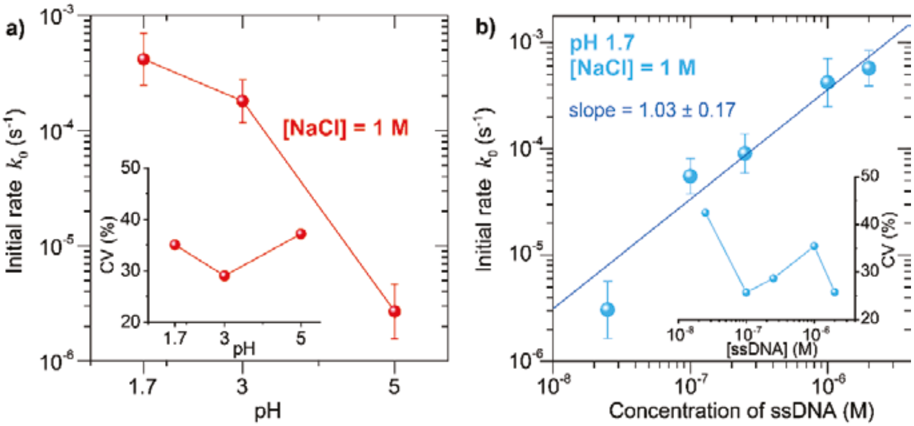

Figure 3.8: Initial binding rates k_0 as a function of **a)** buffer pH and **b)** ssDNA concentration. The datapoints indicate the mean and standard deviations of the distributions extracted from the single-particle timetraces. The insets show the CV of the distribution k_0.

We also determined the dependence of the initial rate on ssDNA concentration. These measurements were performed at a buffer pH of 1.7 with 1 M of additional NaCl, the distributions of k_0 are shown in Figure 3.8b. We fitted the concentration series with a power law obtaining an exponent of 1.03 ± 0.17, confirming that the functionalization is a first-order reaction. We find that k_0 exhibits comparable heterogeneities independent of pH and ssDNA concentration (see insets Figure 3.8).

3.4.3 Particle-to-particle variations in kinetics

In contrast to ensemble-averaged studies we also gain insight into the heterogeneity of the functionalization process. We show a histogram of the distribution of k_0 in Figure 3.9 for buffer pH of 1.7 with 1 M of additional NaCl. Surprisingly, we find values for k_0 that vary by nearly an order of magnitude from particle-to-particle. The origin of the heterogeneity in k_0 could be two-fold:

i. the size-dispersion in our sample leading to different sensitivities to refractive index changes, and
ii. particle-to-particle variations in the energy barriers for ssDNA binding leading to a broadened distribution of k_0.

We again assume all variables are normally distributed. This allows us to establish different contributions to the heterogeneity as a convolution of the individual Gaussian distributions. In terms of variances of distributions we can therefore write

$$\sigma_{\mathrm{tot}}^2 = \sigma_{\mathrm{part}}^2 + \sigma_{\mathrm{bar}}^2 , \qquad 3.10$$

where σ_{tot}^2 represents the total (measured) variance k_0, and σ_{part}^2 represents the heterogeneity caused by the distribution in particle sizes. σ_{bar}^2 then represents the contribution from a distribution of energy barriers that have to be overcome by the ssDNA in order to reach the particle surface and successfully bind.

First we explore mechanism (i), the dispersion of particle sizes present in our sample of nanorods. As shown in Figure 3.5, a nanoparticle's sensitivity to refractive index depends on its aspect ratio[245,247] possibly resulting in a distribution of k_0 even if the ssDNA binds at the same rate. In contrast with the end-point measurements we find no correlation of initial rates with the plasmon wavelength. We further employ a core-shell Mie-Gans model[246] to estimate the distribution of k_0 caused purely by the dispersion of particle sizes, and thus disentangle this effect from the *heterogeneity caused by differences in molecular binding rate*. As before, we used a set of representative particles whose sizes were extracted from TEM images. Although this model does not yield absolute values for k_0, we do obtain its relative values by incrementally increasing the refractive index of the shell for the differently sized core particles. Figure 3.9 shows the histogram of initial rates for pH 1.7, here the distribution of k_0

due to the particle size distribution (mangenta histogram) exhibits a variance of $\sigma_{\text{part}}^2 = 0.8 \times 10^{-9}\, s^{-2}$ compared to the total (measured) variance $\sigma_{\text{tot}}^2 = 25 \times 10^{-9}\, s^{-2}$. These variances corrrespond to $CV_{\text{part}} = 8\,\%$ due to the particle-size distribution, compard to the measured $CV_{\text{tot}} = 35\,\%$. Therefore, the size dispersion is not the dominatant factor determining the broad distribution of k_0.

The residual heterogeneity contributes a variance $\sigma_{bar}^2 = 24.2\ \times 10^{-9}\, s^{-2}$. We observe similar residual heterogeneity for all chemical conditions and ssDNA concentrations. We therefore attribute this additional spread to mechanism (ii), particle-to-particle variations in the surface charge density. The rate at which ssDNA adsorbs on the particle surface depends on the activation energy E_{g} that has to be overcome by a ssDNA molecule approaching the particle. Only when the ssDNA molecule has passed the energy barrier it can adsorb on the gold surface, rearrange, and induce thiol binding. The reaction rate k is then related to E_{g} by the Arrhenius equation, given by:[252]

$$k = Ae^{-\frac{E_{\text{g}}}{k_b T}}, \qquad 3.11$$

where A is the attempt frequency, k_b is Boltzmann's constant, and T is temperature. Based on the strong pH and salt dependence we find for k_0 we infer that E_{g} is dominated by attractive Van der Waals forces and repulsive electrostatic forces, as was concluded before from ensemble-studies.[219,229] The electrostatic interaction depends on the charge distributions on the particle and on the ssDNA, and on the salt-dependent Debye length. Given that our kinetic

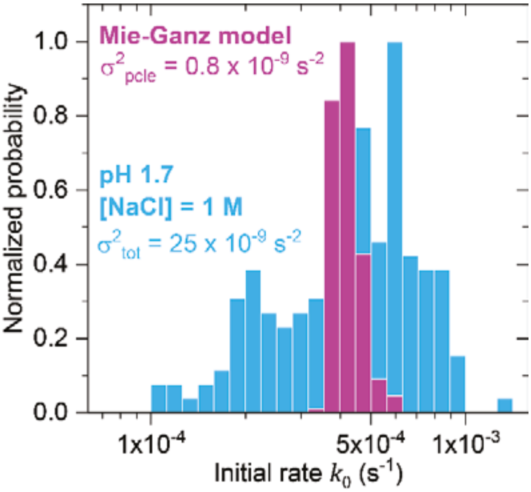

Figure 3.9: Histograms of fitted k_0 for pH 1.7 with 1 M of additional NaCl consisting of 171 individual nanoparticles characterized by a variance of $25\ \times 10^{-9}\, s^{-2}$, and calculated inital rates using core-shell Mie-Gans model whose sizes were extracted from TEM images (215 particles) characterized by a variance of only $0.8\ \times 10^{-9}\, s^{-2}$.

traces average over a large number of ssDNA, the particle-to-particle differences we observe cannot be caused by heterogeneities in the ssDNA.

However, the charge density on the nanoparticle is determined by the density and organization of capping ligands and associated ions on the exposed nanoparticle facets. Interestingly, recent single-particle zeta-potential measurements[253,254] have indeed revealed particle-to-particle differences in zeta-potential for citrate-capped gold particles. Zeta-potential distributions were measured by single-particle electrophoresis through a metallic nanopore, where the transit time depends on the particle's size and surface charge.[253] Particle-to-particle differences in zeta-potential of several tens of percents were found, and were attributed to varying organization and density of citrate on the particle surface.[253]

We therefore propose that this heterogeneity in charge density is the underlying cause of the strong heterogeneity in k_0 that we observe. Indeed, the exponential dependence of k on E_g implies that particle-to-particle variations in surface-charge density of approximately 25 % results in a distribution of k_0 as in Figure 3.9. There are no methods currently available to measure the zeta-potential and k_0 on one-and-the-same particle, which is needed to shed light on the detailed mechanisms causing heterogeneity in the kinetics of functionalization.

3.5 Conclusion

Our results suggest that the final ssDNA density on the particle surface varies by ~ 10 % from particle-to-particle beyond the expected variations due to the Poisson distributed total number of ssDNA strands. The functionalization process itself is unexpectedly heterogeneous and we found rate constants that varied by almost an order of magnitude from particle-to-particle. This strong heterogeneity could not be explained by the particle size dispersion alone. Instead, we attribute the dominant origin of the kinetic heterogeneity to variations in the effective charge on the particle surface due to variations in the capping ligand (citrate) organization and density. These findings will have implications in the use of hybrid nanoparticles for crystallization studies,[226] biosensors,[143] and targeted therapeutics,[255] where the particle functionality is practically determined by a degree of functionalization of the particle surface.

Although these single-particle experiments provide insight into particle-to-particle differences, only relative differences in coverage are revealed. The absolute number of strands per particle can only be obtained at the single-molecule level, where the number of conjugated strands can be counted directly. The following chapter presents such a method based on quantitative super-resolution microscopy.

4 SINGLE-MOLECULE QUANTIFICATION OF NANOPARTICLE FUNCTIONALIZATION[*]

As shown in Chapter 3, functionalization protocols often result in a heterogeneous distribution of particles with a varying density of the functional groups on the particle surface. A lack of methods to directly resolve these molecular properties of the particle's surface hampers optimization of functionalization protocols and applications. Here quantitative single-molecule interaction kinetics is used to count the number of ligands on the surface of hundreds of individual nanoparticles simultaneously. By analyzing the waiting-time between single-molecule binding events we quantify the particle functionalization both accurately and precisely for a large range of ligand densities. We observe significant particle-to-particle differences in functionalization which are dominated by the particle-size distribution for high molecular densities, but are substantially broadened for sparsely functionalized particles. From time-dependent studies we find that ligand reorganization on long timescales drastically reduces this heterogeneity, a process that has remained hidden up to now in ensemble-averaged studies. The quantitative single-molecule counting therefore provides a direct route to quantification and optimization of coupling protocols towards molecularly control colloidal interfaces.

---

[*] *This chapter has been published as "Dynamic single-molecule counting for the quantification and optimzation of nanoparticle functionalization protocols", Nanoscale 2020, 12, 4128−4136.*

4.1 Introduction

Nano- and micro-sized particles proved themselves as versatile probes in bioscience enabling targeting and visualization of specific cellular structures,[256] drug delivery,[257] or even single-molecule sensing.[142] Particularly plasmonic nanoparticles receive attention due to their tunable optical properties,[171] the ability to photothermally heat the particle and release *e.g.* DNA,[258,259] and their biocompatibility upon functionalization.[260] The kinetic response and specificity in these applications is governed by the functionalization of the particle surface with specific biomolecules. In a typical coupling protocol the particles are mixed with the bio-active molecules at specific chemical conditions.[261,262] It is however statistically unlikely that such chemical conjugation protocols result in a homogeneous population of particles each with the same number or density of functional groups (Figure 4.1a). In addition to the variation in the number of functional groups expected from Poisson statistics, in Chapter 3 we found hints of additional heterogeneities due to limitations in the functionalization protocol. These particle-to-particle variations may impair the performance of the functionalized particles, wherein *e.g.* the affinity of a particle for a membrane or the kinetic response of a biosensor depend sensitively on the number of receptors on the particle surface.

Common methods to characterize particle-functionalization, however, have relied on ensemble averaged results, where underlying particle-to-particle differences remain hidden. The kinetics of ligand functionalization and corresponding ligand density are routinely characterized using *i.e.* differential centrifugal sedimentation,[263,264] mass spectrometry,[265] dynamic-light scattering,[263,266,267] and fluorescence assays.[219,221,229,236] The charge of the interfacial layer on the other hand has been determined using zeta-potential measurements[263,266] whereas XPS provides compositional information.[267–270] These ensemble techniques have proven extremely useful to get insight into biomolecular functionalization processes for numerous particle sizes, shapes and materials. However, emerging single-particle applications desire a detailed description and control of the biomolecular layer on the surface of particles. To gain access to particle-to-particle differences the sample needs to be analyzed at the single-particle level[271] while studying many particles simultaneously is crucial to obtain statistics.

Characterization of biomolecular functionalization at the single particle level has been reported using electron microscopy[272,273] due to its high spatial-resolution. Electron microscopy however suffers from a low contrast when imaging biomolecules[274] unless they are labeled using *e.g.* metallic particles.[272] Recently, Eller et al.[275] directly determined the ligand loading on individual gold nanoparticles using a secondary ion mass spectroscopy, and found that the relative DNA loading depends on the particle geometry. Our previous study[276] (Chapter 3) probed plasmon shifts in response to particle functionalization and highlighted the importance of particle-to-particle differences in the kinetics of ssDNA binding to gold nanoparticles. The mentioned methods however either rely on complex instrumentation, do not enable *in situ* characterization, or provide relative loading densities instead of an absolute count of the number of ligands.

Quantitative counting of individual molecules was accomplished by fluorescent labeling and subsequent monitoring of single-molecule photobleaching steps directly after the laser illumination has been applied.[277,278] The method is however limited to particles with a low number of functional groups because single-molecule photobleaching steps should exceed the shotnoise on the total fluorescence signal. Stochastic optical reconstruction microscopy (STORM) localizes fluorescence bursts from single molecules that get activated and then bleach, and has been used to study the spatial distribution,[279,280] and density[281] of ligands. The localization precision of ~10 nm however puts a limit on the maximum density of ligands, and as a result localization microscopy is also

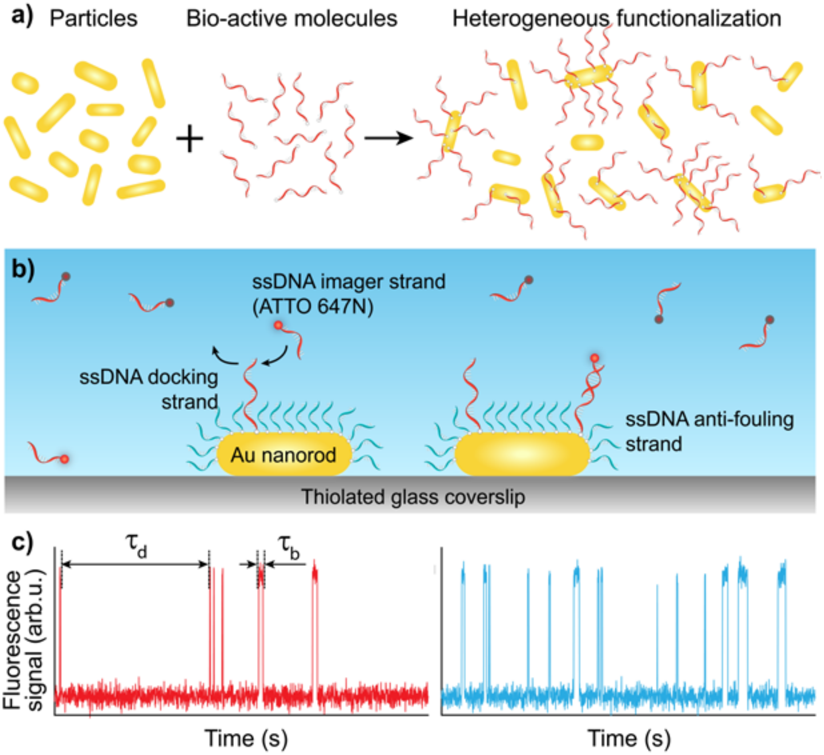
a)
Particles
Bio-active molecules
Heterogeneous functionalization
b)
ssDNA imager strand
(ATTO 647N)
ssDNA docking
strand
Au nanorod
ssDNA anti-fouling
strand
Thiolated glass coverslip
c)
τ_d
τ_b
Fluorescence signal (arb.u.)
Time (s)
Time (s)

Figure 4.1: a) Functionalization of nanoparticles leads to a distribution of bio-active molecules on the surface of the particle, each particle exhibiting a different number of functional groups. **b)** After functionalization the particles are immobilized to allow for quantitative single-molecule counting using DNA-hybridization kinetics. Herein a fluorescently labelled imager strand reversibly binds to the docking strands on the particle. **c)** Using a wide-field fluorescence microscope, each single-molecule hybridization event causes a fluorescent burst. Temporal analysis of the bursts reveals the number of functional groups on each individual particle.

limited to low molecular densities. The dynamic range can be extended upto several hundreds of ligands by counting the frequency of blinking events,[282,283] but this is difficult to quantitate and easily results in overcounting (due to multiple blinks from the same molecule) or undercounting (due to rapid photobleaching). Quantitative single-molecule counting on the other hand has been pioneered by Jungmann who used it to count the number of binding sites on DNA origami structures,[284] and was later applied to count the number of sites on large polystyrene beads.[285]

Here we use such quantitative single-molecule counting to guide functionalization protocols of nanometer size plasmonic particles at the single-particle and single-molecule level (Figure 4.1b,c). This method is accurate for a large range of functionalization densities and does not suffer from blinking and bleaching.[286] We use a stochastic model to predict the precision and accuracy of counting, and demonstrate the method by counting the number of DNA strands on single gold nanoparticles across several orders of magnitude. Although we use gold colloidal nanoparticles, the method proposed here can be in principle applied on particles of any size, shape or material. Since the recorded signal relies on the transient re-binding of a fluorescently labelled ligand, the only requirement is that the particles can be functionalized with a receptor that exhibits a reversible interaction with its ligand. We compare particle-to-particle variations in the number of functional groups for different protocols, and we find that protocols reported in literature yield fast functionalization but with larger than expected particle-to-particle differences. Ligand reorganization over timescales of several hours is needed to reach a state in which particle-to-particle variations are limited by Poisson statistics. The method we present provides a quantitative measure of the number and heterogeneity of functional groups and is a promising avenue to optimize particle-functionalization protocols at the single-particle and single-molecule level.

4.2 Methods

4.2.1 Accuracy and precision of the method

Detection of the transient and repeated binding of a fluorescently labelled ligand to docking strands on a nanoparticle results in a series of fluorescence bursts that are characterized by their respective start- and end-times. The number of bursts (i.e. hybridizations) per unit time scales with the number of docking strands per particle, and this can be quantified in two ways, namely

i. by statistically analyzing the average frequency of fluorescence bursts,

ii. or by analyzing the distribution of waiting times (i.e. the dark times) between the bursts.

Which approach is most accurate is not *a-priori* clear, so we performed stochastic simulations to choose the optimum experimental parameters and quantification method. To investigate the degree of quantification we focus on the counting precision and the counting accuracy (Figure 4.2a).

For this purpose we simulated the binding and unbinding of the imager strand as a random sequential process in which the waiting time until binding (the dark time, or τ_d) and unbinding (the bright time, or τ_b) are both governed by Poisson statistics and thus exponentially distributed. This allows us to generate a timetrace for each docking strand present on a particle, and the response of the particle as a whole then follows from the sum of all N (independent) docking strands (Figure 4.2b). If the number of binding sites on a single particle is estimated n times by independent experiments, the counting precision describes the spread of these estimates around its mean value $\bar{N}$, commonly expressed in terms of a standard deviation σ_N. The counting precision is then essentially determined by the number of events detected on a particle, so for method (i) the number of detected fluorescence bursts, and for method (ii) the number of detected dark times.

The counting accuracy describes to what degree the mean estimated number of sites ($\bar{N}$) deviates from the true number of sites N. These deviations mainly arise when binding events overlap in time, resulting in undercounting. These counting inaccuracies are given by $\Delta N = \bar{N} - N$. We analyze the counting precision and accuracy as a function of the ratio between mean dark- and bright times $\tau_\mathrm{d}/\tau_\mathrm{b}$, which can be expressed in the experimental parameters as

$$\frac{\tau_\mathrm{d}}{\tau_\mathrm{b}} = \frac{k_\mathrm{off}}{N c_\mathrm{img} k_\mathrm{on}}, \qquad 4.1$$

where k_off, k_on, and c_img are the imager strand's dissociation rate, association rate, and concentration, respectively.

The ratio between dark- and bright times can be experimentally tuned by simply changing the imager strand concentration. In Figure 4.2d we plot the normalized counting precision (coefficient of variation), where we observe a low precision for low and high $\tau_\mathrm{d}/\tau_\mathrm{b}$ ratios with an optimum at $\tau_\mathrm{d}/\tau_\mathrm{b} \sim 1$. For large ratios the number of events per timetrace is limited (*e.g.* due to a low c_img), resulting in unprecise counting. For small ratios on the other hand, the large binding frequency results in a fraction of events overlapping in time. This cannot be identified reliably in an experiment, resulting in missed events and thus a reduced total number of events per timetrace for decreasing ratios. The normalized counting precision scales nearly identically for both quantification methods, confirming that the precision is indeed dominated by the (Poissonian) counting statistics. These results indicate that a measurement time of 40 minutes results in a maximum counting precision of $\sigma_\mathrm{N}/\bar{N} = 0.04$, which can evidently be further improved by increasing the measurement time.

For the counting accuracy however we find a large difference between the two methods (Figure 4.2e). Quantification by the frequency of events produces consistent undercounting because each double event affects this frequency.

The probability of double events is low (but not zero) at high $\tau_\mathrm{d}/\tau_\mathrm{b}$ ratios, producing less than 10 % deviation in the number of counted sites, but the accuracy substantially decreases for $\tau_\mathrm{d}/\tau_\mathrm{b} < 10$ due to the increased probability

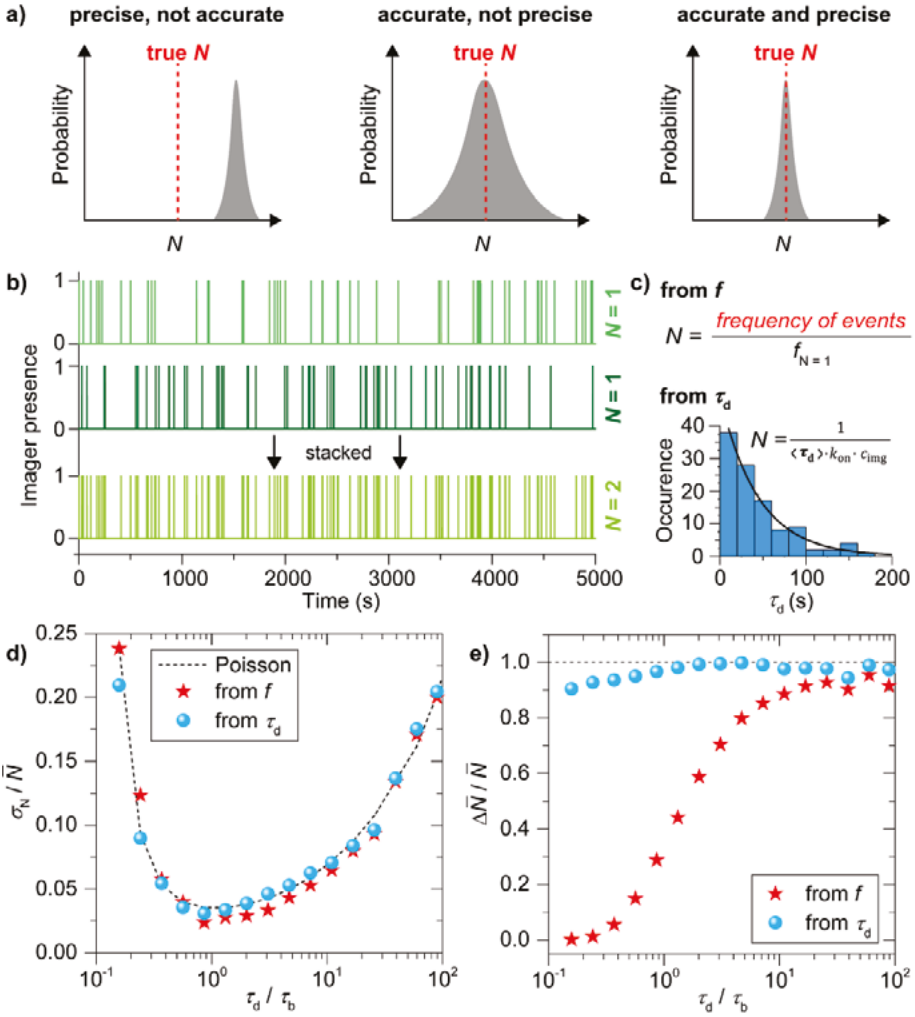

Figure 4.2: a) Concept of measurement precision and accuracy. **b)** Imager transient binding timetraces are generated for every individual docking strand on a particle, and subsequently merged to give the response of the particle as a whole. **c)** Number of docking strands on the particle is determined either from the frequency, or from the distribution of the dark times between the events. Simulated normalized precision **d)** and accuracy **e)** extracted from stochastic simulations of timetraces with a duration of 45 minutes, a camera framerate of 20 Hz, association rate $k_\mathrm{on} = 2.3 \times 10^6\ \mathrm{M}^{-1}s^{-1}$ and dissociation rate $k_\mathrm{off} = 1.6\ s^{-1}$. The precision and accuracy are extracted from 100 simulations performed using these input parameters.

of double events. When the mean dark time is considered the counting accuracy is substantially higher over a larger range of $\tau_\mathrm{d}/\tau_\mathrm{b}$ because double events reduce the number of detected dark times (as captured by σ_N) but do not affect their mean. So although the counting precision reduces when a substantial number of events overlap, the counting accuracy is robust against double events. The deviation of this behavior for $\tau_\mathrm{d}/\tau_\mathrm{b} < 1$ observed in Figure 4.2e is caused by the finite camera framerate (20 fps), which results in overestimation of the dark time and thus undercounting for short dark times.

These stochastic simulations provide guidelines on for the experimental design, and will allow us to quantify the effects of the (intrinsically limited) number of events on the counting precision and accuracy. Based on these simulations we performed the experiments at an imager concentration c_img that leads to $\tau_\mathrm{d}/\tau_\mathrm{b} \sim 20$ (for our imager $k_\mathrm{on} \sim 2.3 \times 10^6\ \mathrm{M}^{-1}\mathrm{s}^{-1}$ and $k_\mathrm{off} \sim 1.6\ \mathrm{s}^{-1}$).[286] This corresponds to imager strand concentrations ranging from 50 pM to 3 nM depending on the expected mean number of docking strands. Although the counting precision could be further improved by working at lower ratios (Figure 4.2d), we will see below that the particle-to-particle variations are dominated by other factors.

4.2.2 Data post-processing

The experimental implementation is based on quantitative PAINT (qPAINT), which was originally developed to count the number of docking strands on DNA origami structures.[284] We apply this method to DNA-functionalized single crystalline gold nanoparticles because they are extensively used for biosensing,[142,207,287] and drug delivery.[222] We first spin-coat the particles onto a thiolated glass coverslip at low surface coverage, see b, and insert the sample in a flow cell. Subsequently we functionalize the particles with thiolated ssDNA docking strands of 30 nucleotides using the protocol described in Chapter 3.[219,221] The docking strands are mixed with short 10 nt antifouling

ssDNA strand	**Length**	**Sequence (from 5' to 3')**
Docking strand	30 nt	SH - CAT CAT CAT ACG CTT CCA AT A ATA CAT CTA
Antifouling strand	10 nt	SH - ACG CTA TCA G
Non-complementary docking strand	30 nt	SH - AAG ATG CTT ACG CTA CGA TTA CGC TAT CAG
Imager strand	10 (9) nt	ATTO 647N – C TAG ATG TAT

Table 4.1: DNA sequences used in the experiments. Complimentary sequences are shown in red. Note that the imager strand is 10 nt long, however only 9 nucleotides are complementary with the docking strand.

ssDNA strands at varying fractions to provide control over the average number of docking strands per particle. See all used ssDNA molecules and their corresponding sequences in Table 4.1. The flow cell is then inserted into an inverted wide-field optical microscope (Nikon Ti) equipped with an oil-immersive objective (Nikon Apo TIRF 100x Oil DIC N2). We excite the sample using objective-type total internal reflection, collect the emitted light with the same objective, and send the wide-field image to an EMCCD camera (Andor DU-888 X-9414). A typical field of view (FOV) is shown in Figure 4.3a where individual diffraction limited spots correspond to either single particles or clusters.

To distinguish single nanoparticles from clusters we record scattering spectra of the nanoparticles using hyperspectral microscopy.[244,276] We illuminate the particles through the objective with a white-light beam (Energetiq) and record wide-field images of the scattered intensity for a set of band-pass filters. Figure 4.3b shows an example of such a scattering spectrum for a single nanoparticle. As before, clusters are identified based on their non-Lorentzian lineshape and broad linewidth, and they are subsequently discarded from further analysis.

After identification of the single particles in the field of view we introduce the imager strand (9 nt complementarity, in PBS with additional 500 mM NaCl) in the flow cell using a syringe pump and excite the ATTO647N label using a 637 nm fiber-coupled laser (intensity in the focal plane ~ 2 kW/cm^2). The emission spectrum of ATTO647N is detuned by nearly 100 nm to the blue of the longitudinal plasmon of the used gold nanorods to reduce plasmon-fluorophore coupling and minimize the ensuing mislocalization.[288–291] We record movies at 20 fps for at least 30 minutes. Transient hybridization of the imager strand to the docking strand on the particle results in bursts of fluorescence, a typical timetrace is shown in Figure 4.3c.

To identify binding events we threshold the timetrace (see Figure 4.3d). In a small fraction of events the detected intensity fluctuates during an event, possibly due to blinking or reorientation of the fluorophore in the polarized excitation beam. These phenomena are corrected for to ensure such cases are treated as a single event. We then localize each event to identify whether it occurred near the particle, or on the substrate away from the particle (see Figure 4.3e). To achieve this we first subtract the 1PL background originating from the particle and fit the resulting point-spread-function with a 2D Gaussian using the maximum likelihood estimation method.[292] The obtained localizations are drift corrected using fiducial markers (particles with a strong 1PL signal), allowing for reconstruction of the particle geometry and identification of events that occurred away from the particle that were discarded from further analysis. Note that this filtering of events based on localization is only possible because we employ a fluorophore with an emission that is blue-shifted from the plasmon resonance, resulting in minimal mislocalization.[289,293–296]

From the experimental data in Figure 4.3 we then finally construct a histogram of all dark times between individual binding events for each single nanoparticle, and fit the histogram with an exponential distribution (Figure 4.3f). The mean dark-time can then be related to the number of docking strands on the particle using Eqn. 4.1.

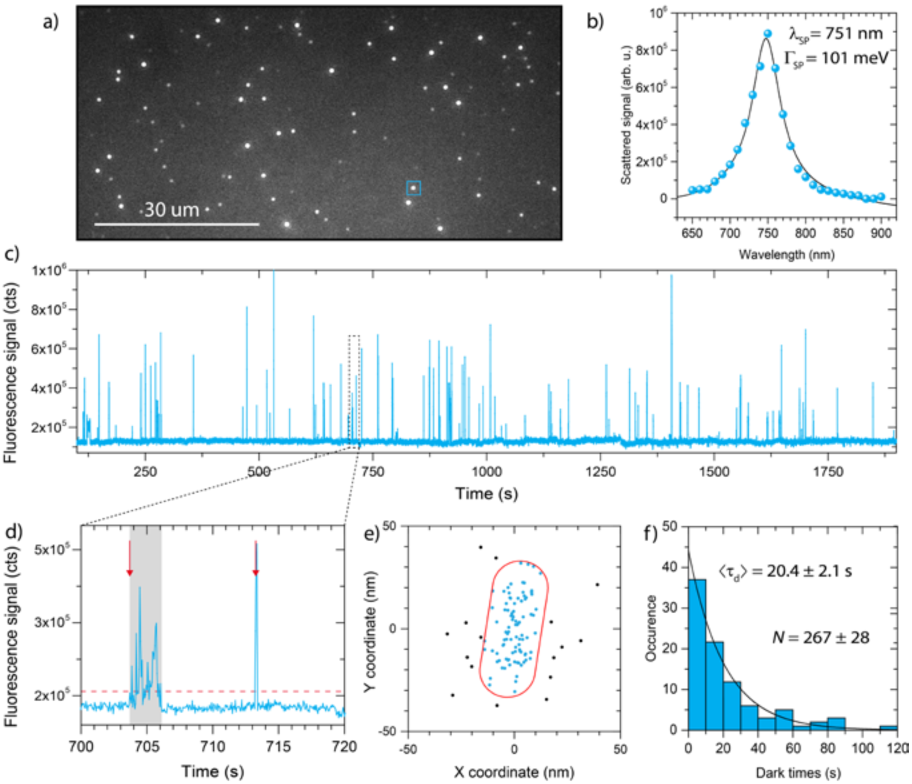

Figure 4.3: **a)** Typical field of view where each diffraction limited spot corresponds to one-photon luminescence from individual nanoparticles or clusters. **b)** Scattering spectrum of a typical nanoparticle measured using hyperspectral microscopy. The solid line shows a fit with a single Lorentzian. **c)** Fluorescence intensity timetrace of the blue square ROI indicated in a). **d)** Bursts above a threshold level (dashed line) are detected, taking into account intermittent dark frames due to blinking. The red arrows indicate examples of two events that are identified. **e)** Individual events are localized, allowing us to identify events that occurred on the particle and events that occurred on the coverslip away from the particle. **f)** The dark-time between events is extracted from the timetrace (events away from the particle are discarded). The distribution of dark-times is fitted with a single-exponential yielding the mean dark-time for each particle in the field of view.

4.3 Results

4.3.1 Specificity of DNA hybridization

Efficient suppression of non-specific interactions with both the particle and the nearby substrate are crucial to achieve accurate counting. The cyan timetrace in Figure 4.4a illustrates that imager strands bind dominantly to the functionalized nanorods with minimal non-specific binding to the glass coverslip. To ensure that the fluorescent bursts we observe are due to specific hybridization between the docking and the imager strands (rather than non-specific binding of the imager strand with the particle) we performed control experiments on nanoparticles functionalized with a mismatched docking strand. We used a 30 nt non-complementary docking strand and a 10 nt antifouling strand, and show corresponding typical timetraces in Figure 4.4a. Only very few molecular events are detected that are mostly localized away from the particle and are thus caused by non-specific binding to the coverslip.

We extracted darktimes between the residual events inside the particle cloud and reconstructed histograms of the number of binding sites (Figure 4.4b,c).

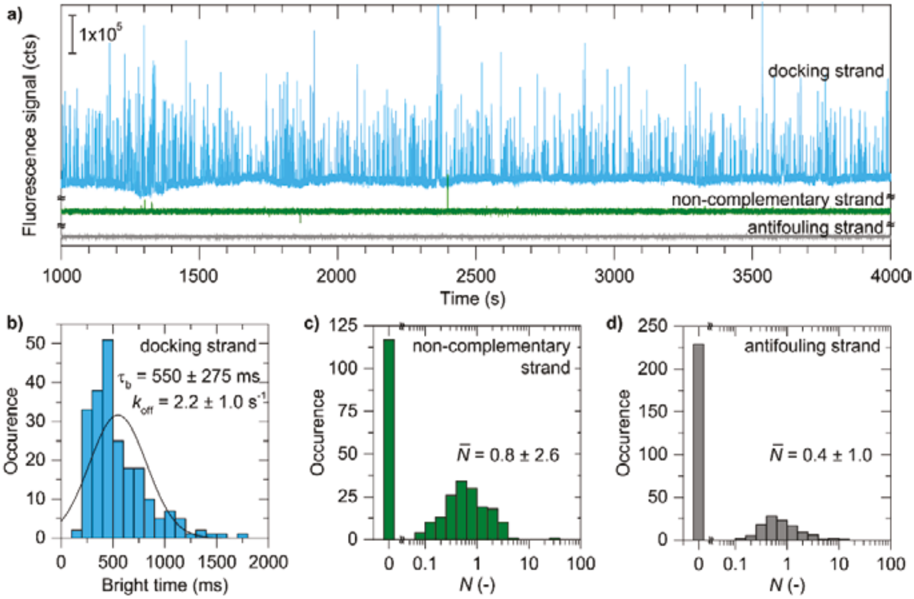

Figure 4.4: a) Examples of typical timetraces for particles functionalized with specific docking strand (cyan), and non-complementary 30 nt and antifouling strands. **b)** Histogram of mean bright times on individual particles, from which we determine the corresponding k_{off} for DNA hybridization. Histograms of number of binding sites are determined from 90 minutes measurements at 1 nM of imager for particles functionalized with 30 nt non-complementary strands **c)** and 10 nt antifouling strands **d)**.

We observe a relatively narrow distributions characterized by a low mean of 0.4 and 0.8 apparent docking strands respectively, with majority of particles showing no detected fluorescence events and thus zero binding sites. However, the determined number of non-specific binding sites suffers from a high statistical error since only a few events were recorded over the 90 minutes of measurement.

To further conclude that the signals in Figure 4.4a are due to specific interactions we determined the dissociation rate of the DNA hybridization. We take single-molecular events inside the localization cloud (Figure 4.3e) and extract their bright times, and find a mean bright time of $\tau_\mathrm{b} = 550 \pm 275$ ms corresponding to the mean dissociation rate of $k_\mathrm{off} = 2.2 \pm 1.0$ s^{-1} matching well with the literature for this sequence.[286] These observations indicate that interference from non-specific interactions after localization filtering is minimal.

4.3.2 Heterogeneous particle functionalization

We then measured the number of docking strands per particle after functionalization with a low pH coupling protocol,[219,221] which we thoroughly investigated in Chapter 3. We varied the time of incubation of a 5 µM solution of 30 nt thiolated docking strand in citric acid buffer, and afterward we back-filled the DNA coating using a 5 µM solution of 10 nt thiolated strands (Figure 4.1b). Histograms of the distribution of the number of docking strands per particle are shown as histograms on a log-log scale in Figure 4.5. For short incubation times of a few seconds we find very heterogeneous functionalization, where the number of docking strands ranges from zero to two hundred per particle. However, as the ssDNA functionalization progresses by an extension of the incubation time we find only a slight increase in the maximum number of binding sites but a significant reduction in the heterogeneity.

This suggests that individual particles undergo a vastly different rate of functionalization, but that the number of ssDNA converges at timescales of a few hundred seconds. This is in agreement with the results in Chapter 3 where we probed plasmon shifts to study the kinetics of ssDNA coating, where we indeed found a large range of initial functionalization rates.[276] For longer incubation times the protocol reaches a plateau at 180 ± 77 binding sites per particle with strongly reduced particle-to-particle differences.

4.3.3 Contributions to inter-particle heterogeneity

The single particle approach gives crucial information on the particle-to-particle differences in the number of docking strands. The underlying sources of heterogeneity can be quantified by the total variance of a measured distribution σ_tot^2, which can be rewritten as a sum of individual contributions as

$$\sigma_\mathrm{tot}^2 = \sigma_\mathrm{parts}^2 + \sigma_\mathrm{Poisson}^2 + \sigma_\mathrm{counting}^2, \qquad 4.2$$

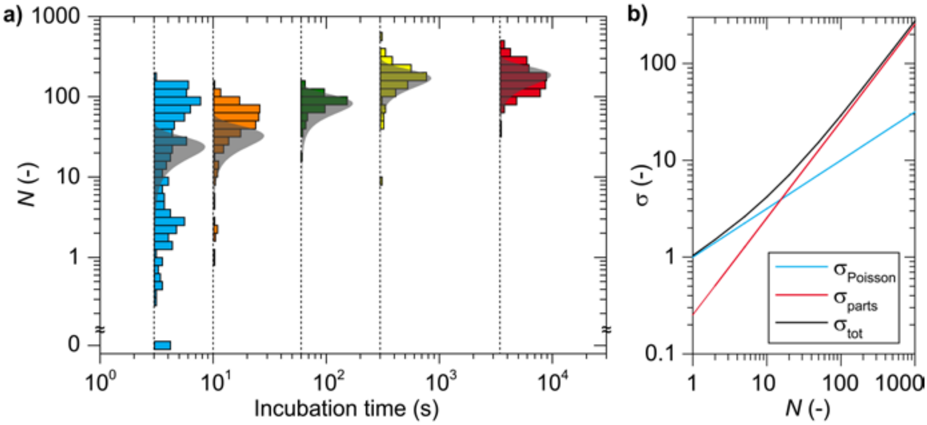

Figure 4.5: a) Suppression of heterogeneity in particle functionalization by prolonging the incubation time. The grey shaded areas are the expected distributions based on the contributions due to the particle size-distribution, and the random nature of the ssDNA functionalization. In **b)** these two contributions are disentangled, showing that at low numbers of sites the contribution due to the Poisson distributed number of strands for equally sized particles dominates, whereas for larger mean numbers of strands the heterogeneity is dominated by the particle-size distribution.

where σ^2_{parts} represents a variance due to the underlying size distribution of the particles, $\sigma^2_{\text{Poisson}}$ stands for the intrinsic variation due to the randomized number of strands per particle following Poisson statistics. The factor $\sigma^2_{\text{counting}}$ represents the counting error due to a finite number of detected events, which we neglect in this analysis because under our optimized conditions it is substantially smaller than the other contributions. Assuming normally distributed variables is a convenient approximation although we note that *e.g.* the Poissonian contribution only approximates a normal one for large values of N. The particle size distribution is well approximated by a normal distribution, whereas the residual heterogeneity can in principle have any distribution function. Nevertheless, this approximation allows us to conveniently disentangle the different contributions to the heterogeneity, and any heterogeneity beyond the expected σ_{tot} is due to sub-optimal functionalization protocols.

The contributions from σ^2_{parts} and $\sigma^2_{\text{Poisson}}$ can be estimated *a-priori*. The latter can be expressed as $\sigma^2_{\text{Poisson}} = N$, and is dominant over σ^2_{parts} for low values of N. For high values of N the term σ^2_{parts} dominates, which we estimate by assuming a ssDNA docking strand footprint of ~16 nm^2 using a conical representation of the ligand. We previously applied this model in Section 3.3.2, and a detailed discussion about the model can be found in Appendix 2. Further we measured the exact dimensions of the nanorods using TEM, to obtain the maximum number of docking strands per particle and its standard deviation of $N_{\text{max}} = 338 \pm 85\ (N \pm \sigma)$. For one hour of incubation we find in our experiments that $N_{\mathrm{max}} = 180 \pm 77$ and find that our particles load approximately to half of the theoretical prediction. This moderate mismatch is possibly caused by steric effects and electrostatic repulsion between randomly absorbed ssDNA strands hindering close-packed functionalization. Comparing the estimated spread to the experimental results (Figure 4.5) we find a drastically broadened distribution compared to our expectations for short incubation times. For the 3 second incubation time the spread in the number of binding sites is ~ 5 fold higher than expected. We attribute this, in concert with our previous ensemble-averaged study, to a heterogeneous binding rate[276] caused by particle-to-particle differences in the zeta-potential,[253] or possible remaining CTAB residuals.

4.3.4 Tuning the number of functional groups

Many applications will benefit from precise *control* over the number of receptors on the particles because the kinetics of a particle-based sensor depends on the number of functional groups,[143,297] and in nanomedicine applications the specificity and efficiency of delivery relies on matching the receptor density on the particle with the one on the cell membrane. Controlling the number of receptors is often done by mixing in a second ligand that functions as a spacer, where it is assumed that the number of receptors on each particle is proportional to the mixing fraction. To verify this simple extrapolation for DNA-functionalized particles we varied the density of docking strands by employing a mixture with a short antifouling strand at varying fractions. We then count the number or docking strands on each individual particle after 1 hour of functionalization. The results are shown in Figure 4.6a, where we observe that for a high fraction of docking strands the number of receptors per particle indeed follows the expected linear trend. However, for low fractions of docking strand we find a significant broadening of the distribution, and a deviation from the linear scaling. Moreover, the particle-to-particle differences are amplified at low fractions of docking strand.

To identify the origin of this non-linearity we incubated the samples with a 1 % fraction of docking strand and vary the incubation time (Figure 4.6b). The data for a very short incubation time of 10 seconds shows a very broad distribution, mainly due to the contribution of non-specific interactions indicated by the shaded area. A general trend can be observed in Figure 4.6b where the maximum number of docking strands is reached in approximately one hour ($\bar{N} = 20$), when the functionalization is also most heterogeneous. A further increase in the incubation time surprisingly reveals a slow decrease in the mean number of binding sites while also the heterogeneity decreases. For the longest measured incubation time of five days we find an almost 4x reduction in the mean number of binding sites to $\bar{N} = 5$, and find a nearly 10-fold reduction in the heterogeneity compared to 1 hour of incubation. Interestingly, for these long incubation times the counted number of binding sites approaches a plateau that is very close to the theoretically predicted number of sites based on the average particle dimensions and DNA footprint (marked by the black arrow in Figure 4.6b).

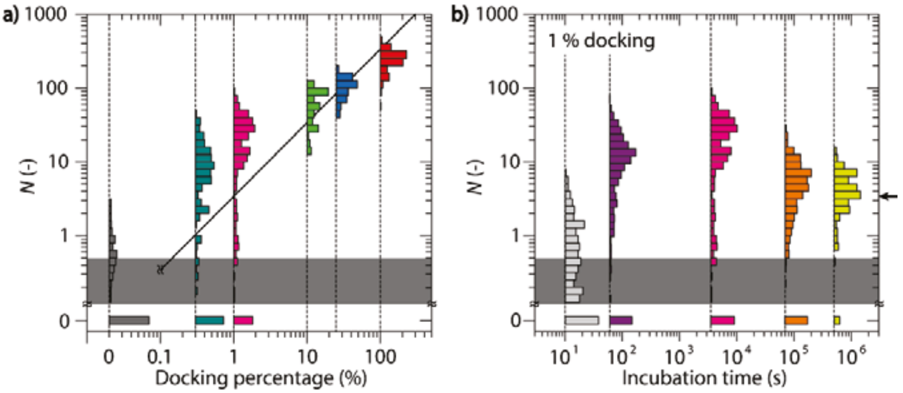

Figure 4.6: a) Controlling the number of functionalized docking strands. The black solid line corresponds to a slope of 1. **b)** Incubation series using 1 % docking solution. The black arrow corresponds to the theoretical prediction based on our model. The contribution of non-specific events is marked by the shaded area.

4.3.5 Ligand reorganization at long timescales

We hypothesize that three mechanisms might be at play that cause the observed trends in Figure 4.6: i) DNA release from the particle, ii) ligand exchange of 30 nt docking strand with 10 nt strands, or iii) ligand reorganization. The first contributor can be ruled out based on the timescale of our incubation because earlier studies concerning release of thiolated ssDNA from the surface of gold nanospheres reported unbinding of only ~ 1.5 % of ssDNA at room temperature per day.[298] We observe a substantially greater reduction, ruling out the thiol release as the main mechanism to the gradual reduction in the number of counted docking strands.

To check mechanism ii) we incubated the samples with 1 % docking strand for one hour, subsequently washed them to remove the residual unbound DNA and left particles in pure citric acid buffer for two days. In Figure 4.7a we show the obtained results (green distribution) and compare them directly to samples incubated for 1 hour (pink) and two continuous days (cyan). In agreement with Figure 4.6 we again observe a decrease in the mean number of binding sites compared to a 1 hour incubation. The results for a 2 day incubation in the DNA, and a 1 hour incubation in DNA followed by a 2 day incubation in buffer show similarly heterogeneous distributions. This allows us to conclude that ligand exchange is not the dominant effect because the sample aged in the pure citric acid buffer for two days has negligible residual ligands present in the pure buffer solution. We further confirm this by results for 100 % docking strand functionalization which we show in Figure 4.7b. We again observe the same trends in the measured data as previously for 1 % docking functionalization.

Ligand reorganization is therefore the dominant factor, where we hypothesize that desorption of non-specifically bound docking strand combined with rearrangement of thiol-bound docking strand are at play, illustrated in Figure 4.8. The timescales on which this behavior is observed is in good agreement with the timescales involved in formation of self-assembled monolayers on metals, where slow diffusion and rearrangement of thiol-bound ligands leads to reorganization of molecular layers.[268] The rearrangement may therefore include such diffusion of interface Au atoms with a ssDNA attached to it, but may also involve changes in accessibility of the docking strand for hybridization with imager strands. We note that ligand reorganization was observed before on gold nanorods,[280] but these experiments were performed in air resulting in initial collapse and thermally induced regeneration of the particle coating. The current experiments provide a direct quantification in aqueous media that is often used in biomedical devices, and thus provides a method to optimize the number of ligands per particle for applications such as sensing and delivery.

The future combination with super-resolution localization microscopy is attractive because it will provide insight into the distribution of receptors on the surface of the particle, and may facilitate the development of functionalization protocols that provide control over receptor location. Such localization microscopy has already been applied to large (micron-sized) polystyrene spheres[285] and has revealed that e.g. microswimmers are propelled due to an anisotropic distribution of enzymes on their surface,[283] and heterogeneous protein absorption over-time leads to largely different protein corona compositions between individual particles related to the surface chemistry and degradability of the studied particles.[282] For nano-sized particles, and particularly plasmonic ones, the use of localization microscopy will require further development of the technology to correct for mislocalizations induced by plasmon-fluorophore coupling. Although for fluorophores that are blue-shifted by > 100 nm from the plasmon resonance the mislocalization is limited to ~ 5 nm,[289,293–296] a general

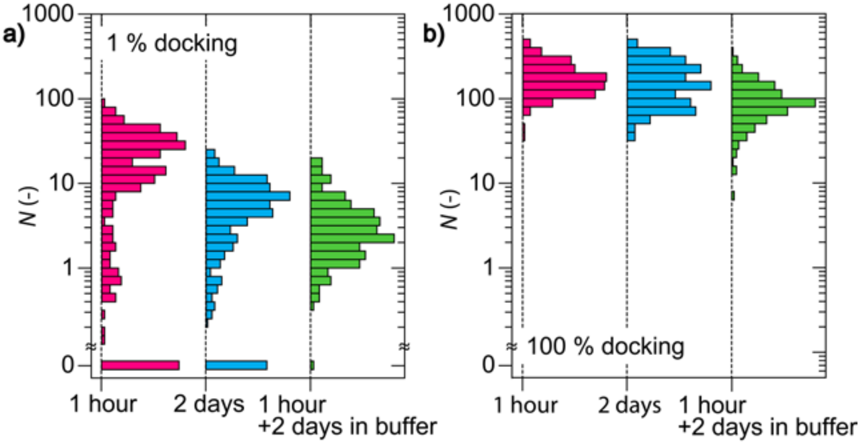

Figure 4.7: Ligand reorganization evidenced by the incubation of samples in DNA solutions with **a)** 1 % and **b)** 100 % docking strand for 2 days, and in DNA solution for 1 hour followed by incubation in buffer for 2 days.

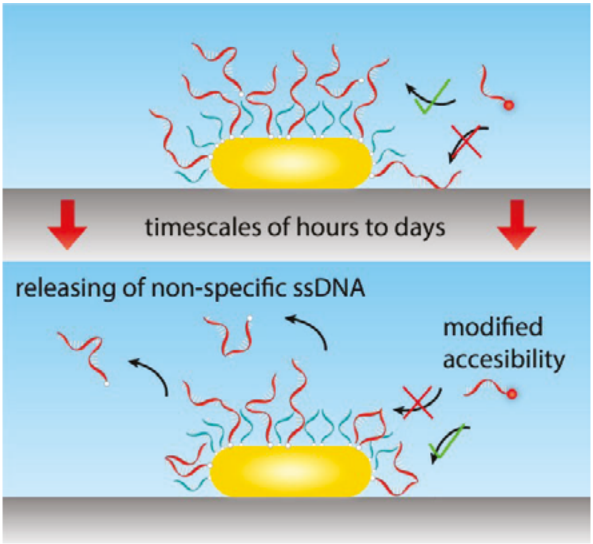

Figure 4.8: Cartoon showing the emerging picture of ligand reorganization that follows from quantitative single-molecule counting.

approach to resolve functional groups on metallic particles will require a refined method to correct for mislocalization that accounts for the spectral properties of dye and particle, and their relative position. Although complex, this will provide the attractive opportunity to obtain the true location of the functional group and characterize the molecular composition of particle coatings at the single-molecule level, and may even enable the tracking of single functional groups during the slow ligand reorganization that we observed.

4.4 Conclusion

We directly counted the number of binding sites on individual single nanoparticles in aqueous solution using stochastic single-molecule interactions. For a typical measurement time of 45 minutes the method exhibits a counting precision better than 5 % with a near-unity counting accuracy for a large range of functionalization densities. Statistical analysis of the interaction kinetics indicated that the particle-to-particle differences we observe are dominated by the particle-size distribution for large particle sizes, but are substantially broadened for short incubation times and for low fractions of functional groups in a mixed monolayer coating. The residual contribution to the heterogeneity was minimized by extending the incubation time. The underlying mechanism points toward ligand reorganization over timescales of several hours to days before the coating reaches a state in which the particle-to-particle variations are limited by Poisson statistics. The methodology presented here enables quantification and optimization of coupling protocols in solution, and opens the window to obtaining molecular control over functionalization protocols for particle-based biosensors and drug-delivery vehicles.

Optimized coupling protocols, as well as the methodology and knowledge obtained in Chapters 3 and 4, are necessary to further investigate real-time molecular folding. Controlled monovalent particle functionalization with a biomolecule is of essence to successfully assemble the plasmonic nanoruler, of which dynamics can be subsequently monitored using its plasmon shift in an optical microscope. Before attempting real-time conformational dynamics experimentally, we first investigate the limits in the spatial and temporal domain for plasmonic dimers of different configurations.

5 PLASMON RULERS AS A PROBE FOR REAL-TIME MICROSECOND CONFORMATIONAL DYNAMICS⁑

Biopolymers such as DNA, RNA and proteins exploit conformational changes to modulate their function. Although state-of-the-art single-molecule approaches enable identification of conformational states, the transition path and metastable intermediates often remain elusive because they occur on microsecond timescales. Here we introduce a method to probe conformational dynamics with microsecond integration times based on a heterodimer of plasmonic particles. By combining Brownian dynamics and electromagnetic simulations we find that integration times of 1 μs can be routinely achieved, providing the capability to identify short-lived intermediates and transition paths at the single-molecule level in real-time. Importantly, plasmon rulers require no specialized equipment but can be probed on existing fluorescence microscopes equipped with a fast camera. The approach combines the advantages of fluorescent probes (zero-force, parallelization) and mechanical probes such as optical tweezers (continuous microsecond integration times). They offer a unique opportunity to study conformational dynamics and compare measurements to full-atom simulations, where computational demands limit the simulation time.

⁑ *This chapter has been published as " Plasmon Rulers as a Probe for Real-Time Microsecond Conformational Dynamics of Single Molecules", Nano Letters 2018, 18, 7927−793.*

5.1 Introduction

Biomolecules like DNA, RNA and proteins form the basic machinery of life.[1] These biopolymers after their synthesis fold into a three-dimensional structure on sub-millisecond timescales,[34] and some undergo conformational changes in their folded form in response to external stimuli.[2–4] Theory predicts that the life-time of a conformational state is typically seconds or longer, but the transition between two conformations involves barrier crossing that occurs on short microsecond timescales. Real-time measurements of these transition path times are formidable challenge due to the broad range of timescales employed in molecular folding. To directly observe molecular folding itself and its event-to-event heterogeneity, one has to repetitively probe the same biomolecule over extensive period of time with a microsecond time resolution. In Chapter 1 of this thesis we provided a detailed discussion of the current state-of-art of the single-molecule methods to probe molecular conformational dynamics. We identified a need for a single-molecule method with a microsecond temporal resolution operating under zero-force conditions.

We proposed the use of dynamic plasmonic nanorulers, whose optical properties and current applications are reviewed in Chapter 2. Published reports indicate that plasmon rulers reveal interparticle distances with sub-nanometer resolution,[167] while providing a photostable optical signal. Recent work by Ye et al. demonstrates the ability of plasmon rulers to measure the conformational dynamics of a protein with 30 ms time resolution.[182] However, their applicability to study micro-second processes in real-time remains unknown because thermal fluctuations of the interparticle distance introduce signal fluctuations at these short timescales.

In this chapter we numerically study the limits in time resolution of dimers of metal nanoparticles as depicted in Figure 5.1a. A conformational change of the tether molecule will modulate the interparticle distance and shifts the plasmon resonance of the dimer [148,170] which thus acts as molecular ruler. If the scattered intensity is recorded at a single wavelength, a change in the distance between the particles leads to a change in the scattered light intensity. This makes the proposed experimental method directly compatible with any existing fluorescence microscope, with the main difference that we detect elastic scattering instead of the Stokes-shifted emission. This new implementation of plasmon rulers combines the advantages of fluorescent probes (zero-force conditions, wide-field imaging) and force-based methods (continuous microsecond integration times), paving the way to unravel the folding process and its heterogeneity in real-time.

We numerically explore the limits of different plasmon rulers by a combination of Brownian dynamics simulations and electromagnetic modelling to show that a time-resolution of 1 μs can be routinely achieved with commercially available particles. Experimental observation of the angular orientation of gold nanoparticles at microsecond integration times have been demonstrated, allowing the simulations to be performed in that regime.[299] We compare two geometries,

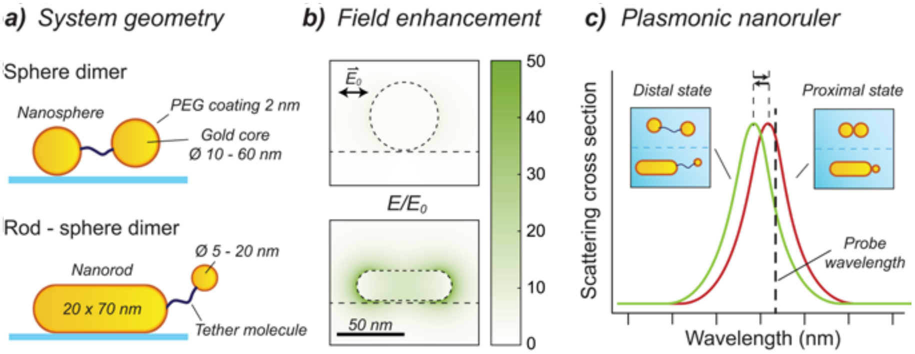
a) System geometry
b) Field enhancement
c) Plasmonic nanoruler
Sphere dimer
Nanosphere
PEG coating 2 nm
Gold core
Ø 10 - 60 nm
Rod - sphere dimer
Nanorod
20 x 70 nm
Ø 5 - 20 nm
Tether molecule
$\vec{E}_0$
E/E_0
50 nm
50
40
30
20
10
0
Scattering cross section
Distal state
Proximal state
Probe wavelength
Wavelength (nm)

Figure 5.1: Plasmon rulers for the measurement of biopolymer conformational dynamics and folding. **a)** Schematic representation of the canonical nanoruler geometry and the heterodimer geometry. Both systems are formed by a surface immobilized primary particle that is linked to a tether particle via a biomolecule. **b)** Numerical simulation of the evanescent field around a gold nanosphere and nanorod resonantly excited at the (longitudinal) plasmon resonance. The evanescent field rapidly decays from the surface of the particle, inducing distance-dependent coupling between the particles. **c)** Comparison of the scattering spectrum of the nanoruler in the proximal and distal state. A change in the interparticle separation leads to a change in the plasmon coupling and concomitant plasmon shift.

namely the canonical plasmon ruler formed by a dimer of spherical gold nanoparticles, and a heterodimer with a gold nanorod as primary particle,[300] see Figure 5.1a. The primary particle in the canonical dimer is a 50 nm diameter gold nanosphere, whereas the heterodimer is constructed around a 20 x 70 nm^2 gold nanorod corresponding to the ideal size for biosensing applications.[245] These particle sizes were chosen because they exhibit a similar but large scattering cross section that enables the use of very small tether particles.

The enhanced electric fields around the particles are shown in Figure 5.1b for excitation resonant with the plasmon wavelength. The fields around the nanorod are significantly stronger than the sphere, mainly because its longitudinal plasmon resonance occurs in the near-infrared, away from the interband absorption of gold. The evanescent field rapidly decays from the surface of the particle, inducing distance-dependent coupling between the particles. In that sense a plasmon ruler shares similarities with FRET, where distance dependent dipolar coupling between two fluorophores is exploited.[301] However, the plasmon ruler is sensitive to distance changes over a significantly longer range than a typical FRET pair, as we already discussed in Section 2.3. This sensitivity range can be further tuned by modifying the size of the primary particle, which modifies the decay length of the near-field.[302]

5.2 Methods and implementation

We first investigate the conformational changes of a two-state (open and closed) ssDNA tether that can form a hairpin structure as shown in Figure 5.2a. In solution-phase experiments the small tethered sphere will diffuse through the enhanced field and cause time-dependent shifts of the plasmon resonance due to a fluctuating interparticle distance. The change in the conformation of the tether leads to a change in the confinement of the tethered sphere. Typically, for a shorter tether the time-averaged interparticle distance is reduced leading to a red-shift of the plasmon resonance of the dimer. As shown in Figure 5.1c if these plasmon shifts are probed using a light source with a wavelength on the red wing of the plasmon, the shifts of the plasmon resonance are then translated to changes in the scattered intensity.[207] We use a numerical approach to simulate the optical signal generated by the dimer. The approach consists of four steps:

i. The probability distribution for the position of the tether particle with respect to the main particle is evaluated by means of Monte Carlo simulations. These simulations take into account the persistence- and contour lengths of the molecular tether.
ii. The Brownian motion trajectory of the tethered particle in this confined space is calculated.
iii. The scattering spectrum corresponding to each position of the tether particle is calculated numerically using the Boundary Element Method.
iv. The resulting time-dependent optical signal is calculated using specific experimental parameters such as probe wavelength, integration time and collection efficiency of the setup.

5.2.1 Probability distribution of tethered particle position

In the first step we determine the configuration space (i.e. the position distribution) of the tether particle using a Monte Carlo simulation method.[122] The particles were simulated as spheres and the rods as spherically capped cylinders. The tether was attached to the side of the primary particle corresponding to the location with largest field enhancement (Figure 5.1b). The tether molecules were simulated as a Kratky-Porod chain[303,304], in which individual straight segments of length l_s with a persistence length of P were connected in series by joints with the bend angle θ and an associated bending energy:

$$E_\mathrm{bend} = \frac{k_\mathrm{b} T P}{2 l_\mathrm{s}} \theta^2, \qquad 5.1$$

where k_b is the Boltzmann constant, and T the temperature. The chain was constructed segment by segment until the required chain length was reached, and the orientation of every next segment in the chain was drawn from a Boltzmann distribution:

$$p \propto e^{-E_{\mathrm{bend}}/k_{\mathrm{b}}T}. \qquad 5.2$$

The open state of the tether was modelled as 50 nucleotides ssDNA linked to the particles via a polyethylene glycol linker, i.e. PEG – ssDNA – PEG with the appropriate segment and persistence length for each component. The PEG components are neutral in charge and have a total contour length of 10 nm. For the simulation of PEG tethers in the system $l_s = 0.1$ nm, $P = 0.1$ nm, for ssDNA $l_s = 0.63$ nm and $P = 3$ nm were used.

In the closed state we assumed that the stem (in red in Figure 5.2a) is far more rigid than the single-stranded portions of the strand, so that the particle-dynamics is determined by the 7 nucleotide single-stranded part (in blue in Figure 5.2a).[305,306] This means that the effective contour length of the DNA changes from 31.5 nm to 4.4 nm upon state switching. The design of the hairpin is based on systems studied using FRET with a few extra nucleotides to act as a spacer between the hairpin and the plasmon ruler.[92]

After the construction of a potential chain configuration, the chain was checked against the boundary conditions thus excluding configurations with the overlap between chain elements, rod, particles, and the surface. If the chain configuration

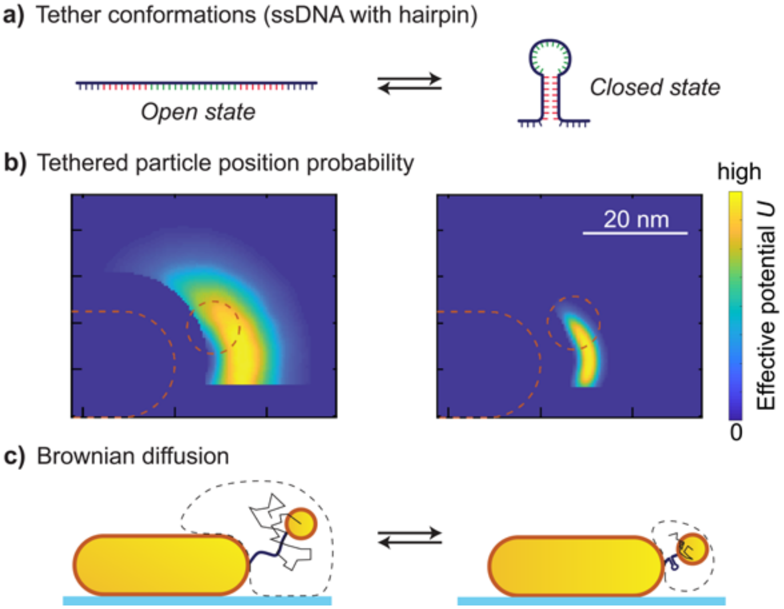
a) Tether conformations (ssDNA with hairpin)
Open state
Closed state
b) Tethered particle position probability
20 nm
high
Effective potential U
0
c) Brownian diffusion

Figure 5.2: a) ssDNA molecule with a sequence that can form a DNA hairpin structure. **b)** The position distribution described by the calculated potential $\boldsymbol{U(\vec{r})}$ of the tether particle, here plotted for the heterodimer in the open and closed conformations. The dashed lines indicate the size of the particles used in the simulation. **c)** The probability p gets more confined as the hairpin closes, leading a decrease in the average interparticle distance. This results in stronger plasmonic coupling between the particles and a red-shift of the plasmon (Figure 5.1c).

was found to be correct the parameter of interest, i.e. the position of the tethered particle, was extracted. This process continued until typically $\geq 2\cdot 10^5$ valid chain configurations were found.

Using the Monte Carlo simulation method, we approximated the position distribution of a nanoparticle that is tethered to a surface immobilized particle. From the position distribution for the open and closed states we determined an effective potential $U(\vec{r})$ that describes the confinement experienced by the particle due to the tether and the nearby interfaces. In principle the effective potential can be immediately calculated from the position distribution by inverting the Boltzmann distribution (Eqn. 5.2):

$$U(\vec{r}) = -k_\mathrm{b} T \ln p(\vec{r}) + C, \tag{5.3}$$

in which C is a constant of integration and was chosen to set the lowest potential at zero. The probability density $p(\vec{r})$ was smoothed [307] without introducing artefacts that arise from the sudden drop to zero at the edge of the excluded volumes. This resulted in a good approximation of the real potential and was further used as the effective potential in the Brownian Dynamics simulations. The potential is plotted for both the open and the closed conformation in Figure 5.2b, where we find a probability distribution with sharp boundaries dictated by the particle surface and underlying substrate.

At physiological ionic strength the Debye length is < 1 nm, indicating that electrostatic interactions between the PEGylated particles and between a PEGylated particle and the ssDNA are effectively shielded. The maximum excursion of the tether particle is therefore determined by the contour length of the tether.

5.2.2 Brownian dynamics simulations

Next, Brownian Dynamics simulations were used to simulate the motion of the particle as it experiences the restrictive effect of the tether described fully by the effective potential $U(\vec{r})$. Our implementation of the Brownian Dynamics uses an algorithm based upon a forward Euler implementation[308] of the Brownian motion of the particle that experiences the effective potential determined from the Monte Carlo simulations. The simulation incremented the position of the particle by a time-step Δt based independently on (1) the Brownian displacement, (2) the displacement due to the effective force giving

$$\Delta\vec{r} = \Delta\vec{r}_\mathrm{Force} + \Delta\vec{r}_\mathrm{Brownian}. \tag{5.4}$$

Using the mean squared displacement equation

$$\langle \vec{r}^2 \rangle = 6D\Delta t, \tag{5.5}$$

the Brownian displacement $\Delta\vec{r}_\mathrm{Brownian}$ was determined by randomly choosing the displacement from a three-dimensional normal distribution with a $6D\Delta t$ standard deviation, where D is the diffusion constant of the tether particle. The effective force due to the tether exerts a drag $\zeta = 6\pi\eta r$ on the particle with radius r in environment of viscosity η , which effectively slowing down the particle diffusion

$$D = k_\mathrm{b}T/\zeta, \tag{5.6}$$

The displacement due to the external effective force was determined

$$\Delta\vec{r}_\mathrm{Force} = -\nabla U/\zeta. \tag{5.7}$$

The calculated displacements were corrected for boundaries of the system caused by particles and substrate. If tether particle is displaced outside the boundaries during any move, the move is not executed and time is not incremented.

The timestep was optimized to minimize computational time and optimize the accuracy of the result. The aforementioned forward Euler method assumes that the acting force is constant, which is not the case. Therefore the timestep needs to be sufficiently short to minimize the error caused by a force changing in time. To ensure an adequate time-resolution for the interpretation of the data a maximum time step of 0.1 ns was used. We estimate the error using the expected Brownian motion; at a maximum timestep of 0.1 ns we expect a average Brownian displacement of 0.12 nm for a particle with a diameter of 5 nm, which provides an upper limit on the error in the diffusive move near the wall. We regard this as sufficiently small as it is below the van der Waals radius of an individual gold atom (166 pm). The result of the Brownian Dynamics simulation is the simulated position of the particle as a function of time.

5.2.3 Electromagnetic calculations

In the third step we perform electromagnetic simulations to account for the fact that the scattering cross-section of the dimer depends on the position of the tether particle relative to the primary particle. The electromagnetic response of the plasmonic system was numerically determined using the BEM,[150,151,157] namely the MNPBEM toolbox developed at the University of Graz.[150] In BEM the materials are characterized by their dielectric functions, and the desired geometry is reduced to its surface which is discretized into a series of polygons. This enables the toolbox to solve the full Maxwell's equations only at the particle boundaries.

The primary particle was placed on a glass substrate in water, and the tethered particle was placed at the position of interest derived from the Brownian Dynamics. The effect of the ssDNA tether on the optical response of the particle is negligible and was therefore not explicitly modelled. For gold we used the dielectric function measured by Johnson and Christy,[138] the glass substrate is characterized by the dielectric function of BK7 glass,[309] the surrounding water is considered to be non-dispersive and is characterized by a dielectric constant $\varepsilon_\mathrm{m} = 1.77$. Since the presence of a PEG coating on the particles only shifts the dimer's plasmon wavelength and leaves the relative results unaffected,

a) *Scattering spectra*

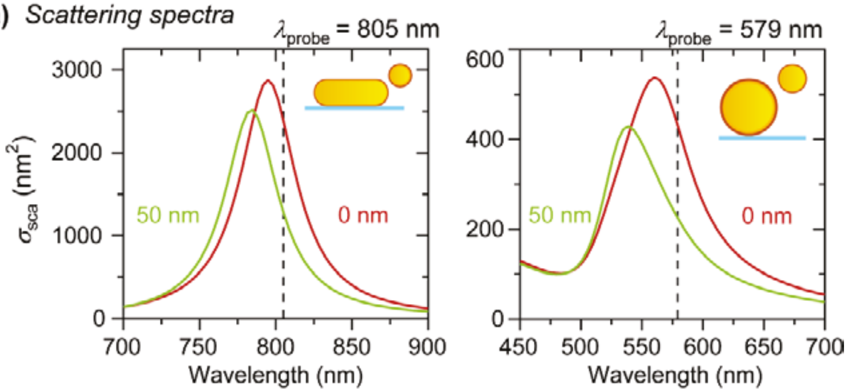

b) *Plasmon shift induced by ⌀ 20 nm sphere*

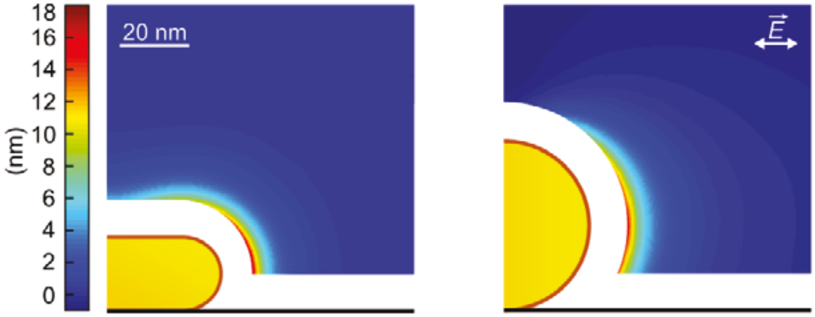

c) *Normalized signal at λ_{probe} for ⌀ 20 nm sphere*

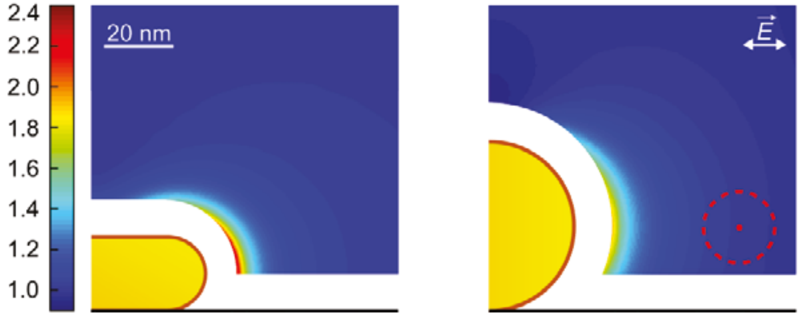

Figure 5.3: Numerical BEM calculations for both plasmonic sensors for a ⌀ 20 nm tethered sphere. **a)** Scattering cross section in the proximal and the distal state of the tethered particle. Dashed lines represent optimum probe wavelengths. Spatial distributions of **b)** plasmon shifts and **c)** normalized scattered signal at probe wavelength λ_{probe} induced by the tethered sphere (locations in maps correspond to the geometrical centre of the tethered sphere as marked by a red dashed circle). The areas that the sphere cannot reach due to volume exclusion are visible as dark areas around the particles. Note that 2D projections are shown, whereas the calculations employ 3D distributions.

the PEG anti-fouling layer was not taken into account. As illumination we used a plane wave with a polarization parallel to the long-axis of the dimer, thereby exciting the longitudinal plasmon of the particle.

We evaluated the full spectra of individual dimers (Figure 5.3a) to find the optimal probe wavelength positioned on the red wing of the dimer's plasmon. Next the scattering and absorption cross sections were calculated at the probe wavelength for all positions of the tethered particle in the three-dimensional grid and were subsequently normalized to their respective references. These calculations were performed for all considered dimer geometries yielding a look-up table of the optical response as function of the position of the tether particle. The Brownian motion trajectories obtained in step (ii) were then used to obtain the scattering cross-section of the nanoruler as a function of time $\sigma_{\text{scat}}(t, \lambda_{\text{probe}})$.

5.2.4 Detected optical signal

Subsequently we calculated the detected number of photons $N_{\text{det}}(t)$ by taking into account the incoming photon flux, the collection efficiency of the setup ($\eta_{\text{det}} = 0.05$), the integration time, and shot noise:

$$N_{\text{det}}(t) = t_{\text{int}} \cdot \overline{\sigma_{\text{scat}}}(t, \lambda_{\text{probe}}) \cdot n_{\text{illum}} \cdot \eta_{\text{det}}. \qquad 5.8$$

The scattering cross-section at the probe wavelength $\sigma_{\text{scat}}(t, \lambda_{\text{probe}})$ was averaged over the integration time t_{int}. The photon flux of the illumination light n_{illum} was chosen to limit the temperature rise on the surface of the nanoruler to 2 K, which minimizes thermal effects on the biomolecule and leads to negligible changes in the diffusion coefficient of the particles. At this maximum available incident intensity, the scattered intensity of the dimer is:

$$I_{\text{scat}} = \frac{4\pi\kappa R \Delta T}{\sigma_{\text{abs}}(t, \lambda_{\text{probe}})} \sigma_{\text{scat}}(t, \lambda_{\text{probe}}), \qquad 5.9$$

with $\kappa = 0.56\,\text{W} \cdot \text{m}^{-1} \cdot \text{K}^{-1}$ the thermal conductivity of water, R the radius of the sphere with volume equal to the particle dimer, and σ_{abs} the absorption cross-section of the dimer at λ_{probe} calculated using BEM simulations. The maximum photon flux can be expressed as:

$$n_{\text{illum}} = \frac{I_{\text{illum}}}{hc/\lambda}. \qquad 5.10$$

giving $n_{\text{illum}} = 3.0 \cdot 10^{26} - 7.7 \cdot 10^{27}\ \ \text{m}^{-2}\,\text{s}^{-1}$ for the dimer geometries considered here.

Shot-noise was added to the detected signal by randomly drawing from a normal distribution with zero-mean and a variance of $\sqrt{N_{\text{det}}}$, congruent with experimental shot noise on a high optical signal. The result is the experimentally recorded signal including all relevant noise sources. Experimental observation of the angular orientation of gold nanoparticles at microsecond integration times have been demonstrated, allowing the simulations to be performed in that regime.[299]

We fully described the detected optical signal of a tethered particle for given tether length thus giving the signal corresponding to a conformational state of ssDNA hairpin. We focus on the signal change caused by conformational changes of a two-state (open and closed) ssDNA hairpin molecule, later we extend this to an arbitrary number of states. The detectability of a conformational change is quantified by the Signal-to-Noise Ratio (SNR). The number of detected photons $N_{\mathrm{det}}(t)$ exhibits a mean and standard deviation: $\mu_N \pm \sigma_N$. If the state of the two-state system changes between open and closed, or vice versa, this is observed as a change in the signal intensity:

$$\Delta\mu_N = \left|\mu_{N,\mathrm{open}} - \mu_{N,\mathrm{closed}}\right|, \qquad 5.11$$

with a compound deviation:

$$\sigma_{\mathrm{tot}} = \sqrt{\sigma_{\mathrm{open}}^2 + \sigma_{\mathrm{closed}}^2}. \qquad 5.12$$

We define the SNR as the ratio between the change in the mean intensity μ and the compound noise σ_{tot}:

$$\mathrm{SNR} = \Delta\mu_N/\sigma_{\mathrm{tot}}. \qquad 5.13$$

5.3 Results

In following section we simulate the thermal fluctuations of the plasmon rulers for different tether particle sizes. We evaluate $\mu_{N,\mathrm{open}}$ and $\mu_{N,\mathrm{closed}}$ as well as their standard deviations σ_{open} and σ_{closed} for both proposed dimer geometries. First we determine the SNR with which we can probe conformational dynamics as a function of the integration time of the detector.

5.3.1 Dependence on detector integration time

Representative calculated timetraces for three different integration times are shown in Figure 5.4a-c for a dimer consisting of a rod and a tether sphere of 20 nm in diameter. The timetraces show the signals in the open and closed state, with an instantaneous transition at $t = 1$ ms. The simulations reveal three regimes:

i. For short integration times (Figure 5.4a), shot noise is the predominant contribution to the SNR.

ii. For intermediate integration times (Figure 5.4b) the shot noise is similar in magnitude to the fluctuations induced by the Brownian motion of the tether particle (Brownian noise).

iii. For longer integration times (Figure 5.4c), the Brownian noise is dominant over shotnoise and gets averaged out leading to an increase in SNR with integration time.

These three regimes are also recognized in Figure 5.4d, where we show the SNR as a function of t_{int} for the heterodimer and its different tether particle sizes. For the 5 nm tether particle the shotnoise is dominant across all t_{int} because the plasmon shift is small upon interparticle distance changes, leading to the expected scaling of the SNR as $\sqrt{t_{\text{int}}}$. The plasmon shift increases with tether particle size,

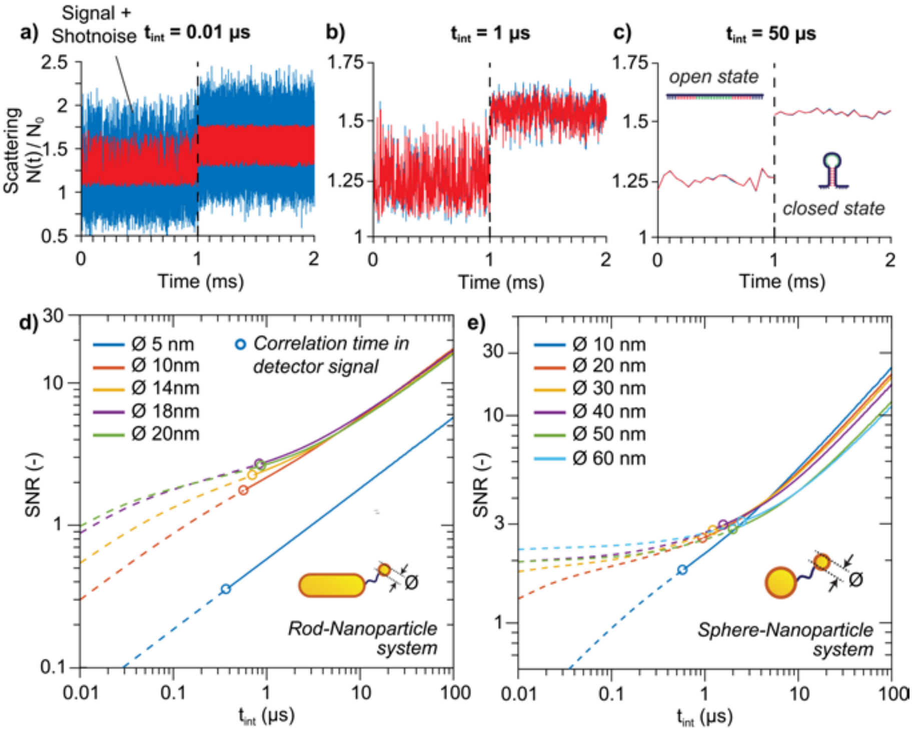

Figure 5.4: a - c) Normalized detector signal $N(t)/N_0$ for a heterodimer (20 x 70 nm^2 rod, sphere Ø 20 nm) as a function of time for three different integration times t_{int} **a)** 0.01 µs – in the shot noise limited regime, **b)** 1 µs – in the intermediate regime, **c)** 50 µs – in the Brownian noise limited regime. The signal due to the Brownian motion and plasmonic coupling is shown in red, the signal with shot noise added is shown in blue. The first millisecond shows the signal of the system in the open state, the second millisecond in the closed state. **d)** The SNR of the detection of a state change between the open and closed state as a function of the integration time for heterodimer with satellite particle diameters of 5, 10, 14, 18 and 20 nm. The time needed by the tether particle to explore the available space in the open state, τ_{p}, is shown as open circles. **e)** The SNR of the detection of a state change between the open and closed state as a function of the integration time for homodimer with satellite sphere diameters of 10, 20, 30, 40, 50, and 60 nm.

and for tether particles larger than 10 nm a transition between the shot noise limited regime and regime limited by Brownian noise is observed for integration times between 0.2 and 2 µs. With larger tethered-particle sizes (14, 18, 20 nm in diameter), shot noise becomes less significant and the transition to the shotnoise dominated regime occurs at shorter t_{int}.

The SNR does not increase continuously with the tether particle diameter but has an optimum at 18 nm. This reflects the fact that larger particles become substantially larger than the near-field, contributing increasingly less to the plasmon shift. Additionally, a larger particle will have a lower diffusion coefficient, which reduces the SNR for shorter integration times because the Brownian motion is averaged less by integration of the signal, leading to the effective detection of more Brownian noise.

In Figure 5.4e we further show the SNR as a function of t_{int} for the homodimer in which the primary particle is a sphere of diameter 50 nm, and we again change the size of the tether sphere. The temporal response of this sphere-sphere dimer is remarkably similar to the heterodimer, and we again observe a crossover from a shot-noise limited regime to a Brownian-noise limited regime on timescales of ~ 1 µs. Surprisingly, the SNR of the sphere-sphere dimer is similar in absolute values to the heterodimer, despite the larger primary particle and broader plasmon resonance.[139] The similarity in SNR is caused by a smaller absorption cross section of the sphere-sphere dimer allowing for a higher excitation power before the surface temperature increase exceeds 2 K.

5.3.2 Characteristic time of the dimer

The ultimate resolution of the plasmonic ruler is defined by the characteristic time at which the tether particle explores all tether configurations. We will refer to this time as the characteristic lag time of the plasmon ruler τ_{ACF}. We quantify τ_{ACF} by considering the autocorrelation function of the detector signal, which was fitted with a single exponential decay function

$$R(t) = e^{-\tau_{\text{ACF}}/t}. \qquad 5.14$$

to yield the characteristic correlation time τ_{ACF}. An example of a typical correlogram and fit is shown in Figure 5.5a for heterodimer with the tether sphere of 10 nm. The autocorrelation function is not strictly mono-exponential due to the complex tether potential and near-field profile of the dimers. The half-time provides an alternative, model-independent, parameter to characterize the decay time but leads to nearly identical results and does not affect our conclusions.

Two major contributions determine τ_{ACF}: the diffusion constant of the particle and the length of the molecular tether. The open circles in Figure 5.4d-e show the SNR at an integration time equal to τ_{ACF} of the open state. Note that τ_{ACF} in the closed state is shorter, but the longer correlation time determines the shortest accessible timescales. We find a clear trade-off between the SNR and τ_{ACF} because the smaller tether-particles diffuse faster but generate a smaller plasmon shift upon conformational changes. Crucially, the heterodimer enables the observation of conformational changes of ssDNA hairpins with SNR ~3 with continuous sub-microsecond integration times.

A direct comparison of the characteristic lag time τ_{ACF} for the two geometries is shown in Figure 5.5b, where we find that τ_{ACF} is mainly determined by the diameter of the tether particle in the investigated size-regime. This implies that robust sensors with a well-defined temporal resolution can be constructed as long as the diameter of the tether particle is well controlled. Current synthesis protocols for gold spheres result in a size distribution with a coefficient of variation of no more than 10%, yielding the required control over τ_{ACF}.

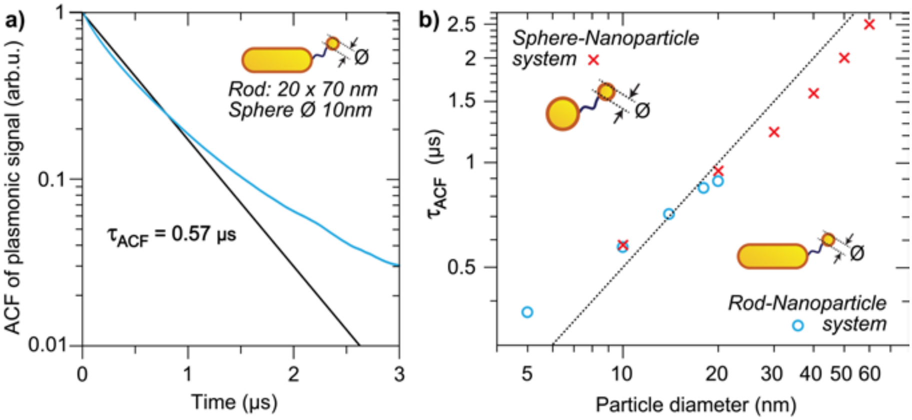

Figure 5.5: a) Correlogram of the autocorrelation of the plasmonic signal for a rod-sphere nanoruler. The characteristic lag time is determined from the single-exponential fit at $\tau_{\mathrm{ACF}} = 0.57\ \mu\mathrm{s}$. **b)** The characteristic lag time τ_{ACF} for the heterodimer and sphere-sphere dimer as a function of the diameter of the tether particle. The corresponding SNRs for $t_{\mathrm{int}} = \tau_{\mathrm{ACF}}$ are around 2 for all tether particle diameters. The dashed line indicates a linear guide to the eye (slope of 50 ns/nm).

5.3.3 General contour length change

Up to now we considered a two-state switching tether with a fixed initial and final contour length. However, many biomolecules exhibit short-lived intermediates in their folding trajectory with microsecond lifetimes, prime examples are metastable intermediates of small folding proteins,[20] partially open intermediates associated with membrane transporters,[310] and pseudoknots in oligonucleotides.[311] Such metastable states have typical lifetimes of some tens of microseconds, but can currently not be detected directly. In Figure 5.6a we show a simulated timetrace of an oligonucleotide that exchanges between three conformations on microsecond timescales. Extraction of the underlying states using change-point analysis [312] illustrates the capability of the plasmon ruler to reliably detect short-lived intermediate conformations. This also allows us to generalize our results to an arbitrary conformational change by considering a change in contour length from l_{init} to l_{fin}. We focus on the heterodimer and numerically evaluate its capability to resolve these transitions for an 18 nm diameter tether particle at $t_{\text{int}} = 1$ µs. We plot the results in Figure 5.6b, where contour lines indicate the SNR achievable for a certain $\Delta l = l_{\text{fin}} - l_{\text{init}}$.

As expected, larger values for Δl lead to a higher SNR for detection of the state-change, reaching SNR > 3.5 for $\Delta l = 40$ nm. We find that a certain Δl can be resolved with higher SNR for shorter l_{init}. This is explained by three effects:

i. at shorter l_{init} the relative change in contour length is larger,

ii. due to the increased effect of molecular coiling at larger tether lengths the time-averaged particle-separation scales sub-linear with contour length,

iii. the plasmon shift for a certain value of Δl is larger if it occurs closer to the nanorod surface because the gradient in the near-field is higher (Figure 5.1a).

The required SNR to extract a state-change depends on the lifetimes of the intermediate states and the used analytical method. For example, detection of a state-change by simple thresholding requires a SNR ~ 2, while hidden Markov modelling can analyze state changes at lower SNR.[313–315] At SNR = 1 discrete contour length changes of 3 nm → 5.5 nm → 9 nm → 15 nm → 35 nm are detectable and directly relevant to the folding of e.g. aptamers, DNA hairpins and polypeptides. This implies that under optimized conditions up to 5 individual states can be distinguished, providing the opportunity to *e.g.* investigate multi-state folding.

Our simulations assume that the tether particle is attached on the tip of the primary particle. Attachment to the side of the nanorod would lead to a factor 5 lower signal and thus factor $\sqrt{5}$ lower SNR ratio in the shotnoise limited regime. For the heterodimer a tip-specific functionalization is thus preferred and can be achieved using site-specific functionalization protocols reported in literature.[316–319] In addition, pioneering work by Mirkin and Alivisatos allows for the synthesis and purification of monovalent constructs.[191,192] For the heterodimer the optimum signal-to-noise ratio is then achieved by employing a linearly polarized excitation field along the nanorod-axis (Figure 5.1a). For the sphere-sphere dimer the orientation of the dimer is modulated by the position of the tether particle, so in this case circularly polarized light results in maximum SNR.

5.4 Conclusion

Our numerical simulations show that plasmonic nanorulers are a promising platform to study the conformational dynamics of molecules in real-time at microsecond timescales. Due to the brightness and photostability of the plasmon resonance the temporal resolution is not limited by shot-noise but rather by the diffusion of the tether particle that introduces fluctuations of the optical signal. The use of a large primary particle allows for the use

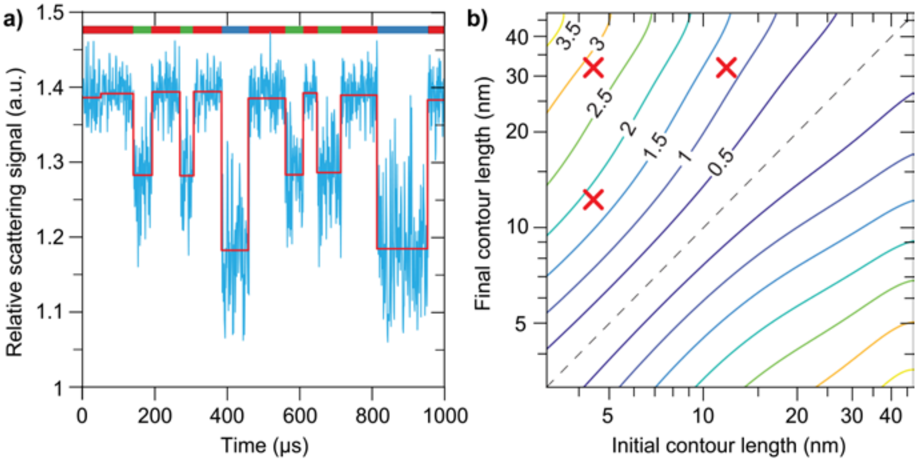

Figure 5.6: a) Timetrace of a three-state DNA hairpin representing a system with an intermediate metastable state, simulated for $t_{\text{int}} = 1$ µs and $\eta_{\text{det}} = 5$ %. The red line presents the analysis of the timetrace using a change point step finding algorithm.[312] The dimer consists of a nanorod of 20 x 70 nm^2 and a tether particle with a diameter of 18 nm. The colored bar at the top of the graph represents the state of the system. The contour lengths of the three states are respectively 50 nt for the open state (31.5 nm, blue), 20 nt for the intermediate state (12.5 nm, green) and 7 nt for the closed state (4.4 nm, red). The states have a random lifetime between 30 and 150 µs. **b)** The calculated SNR for an arbitrary change in the contour length of a ssDNA tether for $t_{\text{int}} = 1$ µs. The SNR is shown as a contour plot with the initial and final contour length of the ssDNA tether on the x-axis and y-axis. Note that under all conditions the Brownian motion of the tether particle is the limiting factor; the shot noise is negligible. The red crosses correspond to the DNA contour length change occurring between the open, intermediate and closed state of the hairpin. The dashed line indicates zero change in contour length.

of a very small tether particle thus minimizing interference of the molecular dynamics. The ultimate temporal resolution is approximately three orders of magnitude higher than state-of-the-art smFRET due to a higher photon budget, and approximately ~10 times higher than recent force-based methods owing to the nanometer-sized tether particles.[66,75] Surprisingly, we observe a very similar response between both types of dimers due to the compensating effect of the ratio between the absorption and scattering cross-section.

One of the strengths of smFRET is the ability to probe many constructs simultaneously in the field of view of the microscope to acquire statistics. Plasmon rulers are equally well probed in parallel by imaging the scattered signal on a camera,[207] where access to microsecond timescales is warranted by an intensified CCD camera or by commercially available high-speed CMOS cameras. This makes the experimental implementation of plasmon rulers straightforward because the microscope required is already available in nearly any research laboratory. Plasmonic nanorulers therefore overcome important hurdles in existing techniques and combine the advantages of smFRET (zero-force conditions, parallelization) and force-based methods (continuous microsecond integration times), paving the way to start unraveling the folding process and its heterogeneity in real-time.

In our simulation results the most optimal system for the observation of molecular dynamics with an integration time of 1 µs is a nanorod with dimensions 20 x 70 nm^2 with a tether particle of ⌀ 18 nm. In the following chapter we use nanoparticles of such dimensions and focus on the experimental assembly of the proposed plasmonic dimer, and explore its use to study conformational changes of single-molecules.

6 A HETERODIMERIC PLASMON RULER FOR SINGLE-MOLECULE CONFORMATIONAL DYNAMICS

We present a method to assemble a plasmonic ruler consisting of a nanorod-nanosphere heterodimer interconnected by a ssDNA hairpin. After optimization of the particle antifouling coating, the ssDNA hairpin is conjugated between the particles using two orthogonal crosslinking chemistries: EDC/NHS coupling in combination with copper-free click chemistry. We continuously monitor hundreds of individual plasmonic rulers using a wide-field microscopy with millisecond temporal resolution. We classify the observed dynamic behavior based on the characteristic times using autocorrelation analysis, and the constructs showing characteristic times of 1 – 2 seconds are ascribed to the single-molecule hairpin switching. Further we extracted dwell times in the open and closed molecular states for individual plasmonic rulers, and found them to be exponentially distributed in line with the single-molecule switching behavior. Their corresponding mean dwell times show that the molecular switching occurs on timescales of ~ 1 second, which is in excellent agreement with theoretical predictions for a hairpin with a stem-region of 10 nt used here.

6.1 Introduction

Visualizing molecular folding transitions is a complex task since these transitions appear at short timescales and at nanometer length scales, which are difficult to access using standard experimental approaches.[9,10] Full-atom molecular dynamics simulations have provided structural and dynamic information required to understand the molecular folding mechanism and to establish an underlying theoretical background.[11–13] These simulations have hinted that the pathway that a biomolecule follows from an unfolded to a folded state is likely heterogeneous (i.e. the exact pathway followed differs from *molecule-to-molecule*, and from *transition-to-transition*) and involves in most cases short-lived intermediate states.

Resolving these pathways therefore requires a single-molecule approach. In Chapter 1 of this thesis we have outlined current single-molecule biophysical methods being used to study these transitions. However, none of these approaches provides access to microsecond timescales without the application of an external force (Figure 1.5). In Chapter 5 we have shown that heterodimeric plasmon rulers may provide the possibility to achieve this, with integration times in the low-microsecond regime.

In this chapter we report the experimental assembly of the heterodimer, with dimensions based on the design rules we obtained in the previous chapter. As a model system we use a ssDNA sequence forming a structure with two conformational states: either the unfolded stretched conformation, or the secondary hairpin-like structure (Figure 6.1a,d). We probe the molecular switching by scattering-based microscopy using total-internal-reflection excitation on millisecond timescales. A shift of the plasmon resonance induced by changes in nanorod-nanosphere proximity then induces a change in the detected scattered intensity (Figure 6.1b). We continuously monitor the scattered

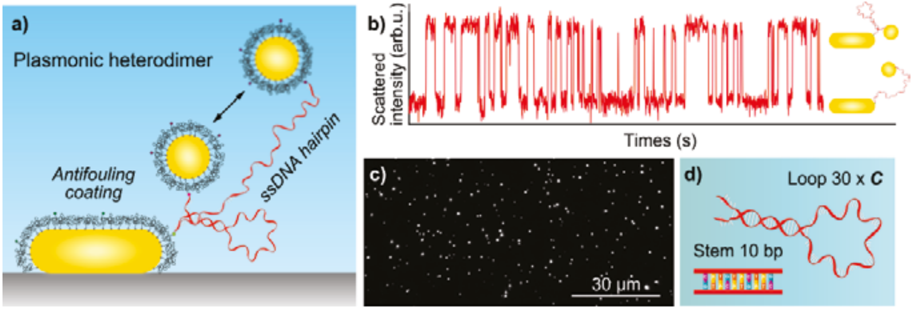

Figure 6.1: a) Schematic of the heterodimeric plasmon ruler interconnected by a dynamic ssDNA hairpin. **b)** Switching between the closed and open states is probed using narrowband excitation, in which changes in nanorod-nanosphere proximity are revealed as modulations in the scattered intensity. **c)** The dynamics is probed in a wide-field optical microscope using total-internal-reflection excitation, allowing for the probing of hundreds of rulers in parallel. **d)** Design of the ssDNA hairpin, including a 10 nt stem region and a 30 nt loop.

intensity from hundreds of individual rulers in parallel using a wide-field microscope (Figure 6.1c) revealing interparticle distance changes over time caused by the dynamics of the interconnecting biomolecule. The hairpin is designed using a stem-region of 10 nt (Figure 6.1d) resulting in switching that occurs on timescales of ~1 second.[32] After optimization of the particle coating we experimentally measure the dwell times in the closed and open states of the ssDNA hairpin, which are in excellent agreement with theoretical expectations.

6.2 Assembly of a heterodimeric plasmon ruler

Here we describe our strategy to experimentally prepare the plasmonic dimer consisting of an immobilized gold nanorod and a tethered gold nanosphere in order to experimentally investigate conformational changes of the interconnecting ssDNA hairpin (Figure 6.1). The numerical models presented in Chapter 5 supply us with design rules for the particle dimensions and DNA tether. We therefore used colloidal gold nanorods of 20 nm diameter and a length of 75 nm and gold nanospheres of 20 nm in diameter. The ssDNA hairpin consists of a 66 nt strand with a 10 nt complementary stem loop, similar to the design simulated in Chapter 5 (for the sequence see Table 6.3).

The design of the dimer and optimization of the protocols used for its assembly ideally achieve the linking of a single gold nanorod to a single gold nanosphere via a single ssDNA tether. The left side of Figure 6.2a shows this ideal case where a gold nanorod is immobilized on the glass surface, while the nanosphere undergoes Brownian motion restricted only by the single ssDNA tether, *i.e.* no other physical connection is established between the particles.

The right side of Figure 6.2a sketches the undesired geometries arising from non-specific interactions between the particles, and between the particles and the ssDNA. In the following paragraphs we describe a step-by-step optimization of the assembly to avoid such undesired configurations, and to practically assemble a functional plasmonic nanoruler.

We have two main strategies at our disposal to prepare a functional sample. The first one (mostly used in the chemistry community) is a *solution-based approach*, where the coupling of molecular ligands is performed on solution-phase nanoparticles in a flask. A clear advantage of this strategy is its high throughput because high concentrations and larger volumes of particles can be processed in a relatively short time. However, such an ensemble approach suffers from a lack of control and typically yields a large range of multi-particle assemblies that requires purification steps to isolate them. The second strategy is a *bottom-up approach* where the particles are assembled step-by-step on a solid substrate. This provides the unique opportunity to monitor every step in the functionalization process in real-time using optical microscopy and spectroscopy.

We employ a combination of both strategies (Figure 6.2b): We prepare gold nanospheres decorated with ssDNA hairpins in solution, while the nanorods are spincoated onto glass coverslips and subsequently functionalized with antifouling molecules in a flow cell. Once functionalized, the pre-decorated gold spheres are introduced in the flow cell allowing us to monitor the nanorod-nanosphere conjugation in real-time using single-particle microscopy and spectroscopy.

To prevent the non-specific interactions as sketched in Figure 6.2a with an exposed gold surface we first optimize the antifouling coating on the nanoparticles (Figure 6.2c). This coating should (1) suppress non-specific interactions between the tether nanoparticle and the main particle, (2) suppress non-specific interactions between the particles and the DNA tether itself, and (3) allow for the specific and oriented conjugation of the hairpin. In the next three sections we discuss these aspects separately.

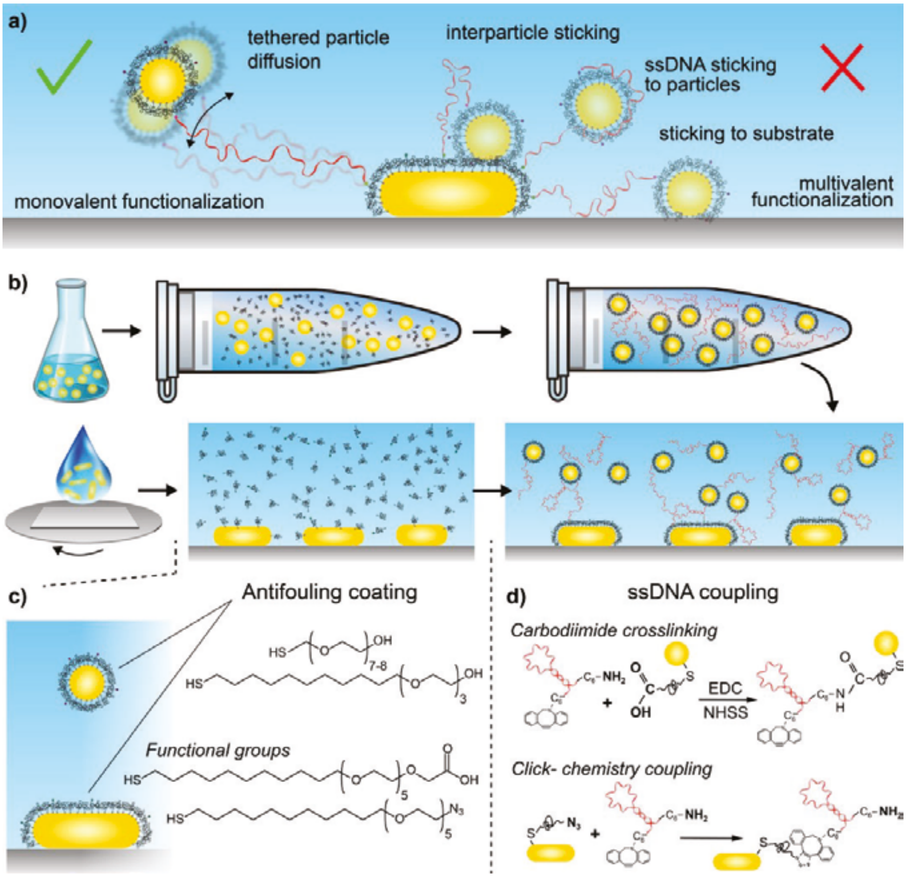
a)
tethered particle diffusion
interparticle sticking
ssDNA sticking to particles
sticking to substrate
monovalent functionalization
multivalent functionalization
b)
c)
Antifouling coating
Functional groups
HS
OH
7-8
3
5
N_3
d)
ssDNA coupling
Carbodiimide crosslinking
EDC
NHSS
Click- chemistry coupling
C_6-NH_2

Figure 6.2: a) Scheme of the proposed plasmonic dimer with the left side showing the ideal monovalent tethering with no non-specific interactions, and the right side illustrating possible non-specific interactions that should be prevented. **b)** Our proposed experimental assembly of the plasmonic nanoruler system. **c)** Antifouling coating of nanoparticles based on PEG. We incorporated functional groups for further coupling of ssDNA **d)** to the coated nanoparticles.

6.2.1 Anti-fouling against nanoparticle-nanoparticle interactions

First, we optimize the anti-fouling coatings on the nanorods and the nanospheres, and test their non-specific interactions against each other. We spincoated the gold nanorods on a thiolated glass coverslip, and subsequently rinsed the coverslips with 1 M NaCl, PBS, MQ water, ethanol, methanol, and finally blow dry with N_2. Subsequently, the surface immobilized nanorods were functionalized with varying anti-fouling coatings by flowing the respective solutions into the flow chamber. In Figure 6.2c we show the employed antifouling molecules SH - PEG_n – OH (n ~ 7 – 8) (400 Da) and SH - C_{11} - PEG_3 - OH (330 Da), which we incubated with particles at a concentration of 10 mM in PBS for 1 hour or overnight. Although similar in molecular weight, the C_{11}-PEG chain will create a self-assembled monolayer (SAM) on the gold particle, whereas the other PEG will form a mushroom-like conformation.[320–322] We observed, for incubation times longer than 1 hour, that particles functionalized with SH - C_{11} - PEG_3 - OH tend to desorb from the glass coverslip likely because the dense self-assembled monolayer on the particle competes with the thiol-linkages between the glass coverslip and the particle. After the PEG functionalization the slides were rinsed with 1 M NaCl, PBS, MQ water, ethanol, methanol, sonicated in methanol bath for 15 minutes, and then stored in MQ. The coverslips were inserted into the flow cell, and the samples were further investigate by single-particle microscopy and spectroscopy as described in the previous chapters.

As tether particle we used colloidal gold nanospheres (*Sigma Aldrich*) with an average diameter of 20 nm that were functionalized in a flask. Gold spheres are initially stabilized with citric acid giving them poor colloidal stability at ionic strengths exceeding 10 mM. Therefore we first perform a ligand exchange on these particles to replace citric acid with bis(p-sulfonatophenyl)phenylphosphine (BSPP) by incubation with BSPP at 10-100 mM for at least 48 hours. Repeated centrifugation and redispersion in 1 mM BSPP solution ensured the efficient removal of citric acid. The particles were then incubated overnight with a 10^7 times molar excess of SH – PEG_n – OH or SH – C_{11} – PEG_3 – OH. Repeated centrifugation and redispersion in PBS diluted to 45 mM ionic strength was used to remove excess ligands from solution.

A 5 nM solution of the coated gold nanospheres was then pumped into the flow cell containing the immobilized nanorods. The dynamic plasmon shifts of individual nanorods were monitored by dark-field scattering microscopy using a superluminescent diode with a center wavelength of 793 nm for ~30 minutes. Non-specific interactions between spheres and rods then result in (transient) plasmon shifts that are observed as step-wise changes in the scattered intensity, see for more details Section 3.2. These measurements showed a mix of behaviors (Figure 6.3) that we classified into three distinct regimes:

i. *The transient interaction* of spheres to a gold nanorod is characterized by short spikes in the signal mean, which after several consecutive frames drop back to the baseline value (Figure 6.3a). We find a broad range of spike-durations with a large population of spikes lasting < 200 ms

(4 frames, Figure 6.3b). Considering that the characteristic time required for a 20 nm diameter sphere to diffuse through the near-field of the nanorod is < 10 µs, all events we observe here are attributed to transient sticking with a low affinity.

ii. Often the temporary sticking of a sphere result in *tethered particle motion* (TPM) of the sphere. This regime is analysed in Figure 6.3c where a sphere sticks and appears to be firmly bound via the PEG coating, however dettaches and starts to diffuse in a confined space in the nanorod's proximity. Such non-specific TPM is characterized by a rapidly fluctuating signal, sometimes between two clear levels of signal intensity determined by the proximal and distal states of the tethered sphere (Figure 6.3d). Such non-specific TPM is found to last from a few seconds to even hours.

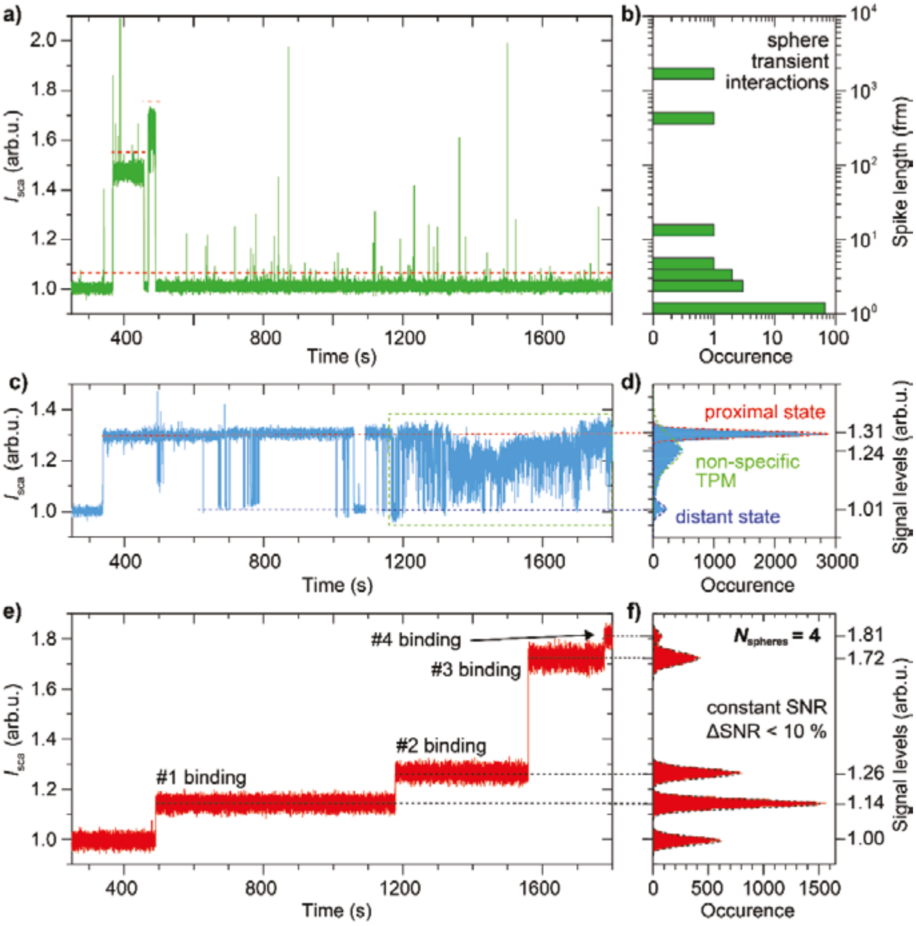

Figure 6.3: Three examples of typical timetraces and their quantitative analysis for non-specific rod-sphere interactions classified by the three regimes described in the text.

iii. In the last regime strong interactions between the sphere and the nanorod result in *the permanent binding and immobilization* of a sphere on the rod surface (Figure 6.3e). This is characterized by a permanent change of the signal mean level for the remainder of the measurement. These well-defined signal changes allow for the direct counting of the permanently bound spheres from the signal histogram (Figure 6.3f).

Although the example timetraces in Figure 6.3 show three distinct regimes, often a mixture of all regimes is detected instead. To quantify the antifouling performance we first examine the appearance of the individual regimes in our measurements for different antifouling coatings. Pie charts in Figure 6.4a summarize the relative appearance of the three classes of behavior that we observe. Comparing bare (that is: BSPP coated) particles with the PEGylated ones we find a substantial reduction in the fraction of particles that permanently binds gold spheres, particularly for the self-assembled monolayer of PEG. On the other hand, the self-assembled monolayer of PEG increases the fraction of assemblies that exhibit non-specific TPM.

We further analyzed the particles showing non-specific TPM by correcting individual timetraces for thermal drift and manually counting the number of non-specifically tethered spheres for each single gold nanorod. We plot the measured distributions for different particle coatings in Figure 6.4b. Interestingly, we find similar distributions of the number of non-specifically tethered spheres for the different coatings. Using the same procedure we also counted the number of permanently bound spheres, Figure 6.4c summarizes these distributions. We find a significant reduction in the number of permanently bound spheres when both particles are functionalized with PEG where particularly the self-assembled monolayer of $SH - C_{11} - PEG_3 - OH$ performs well.

The coating with the best antifouling properties against other nanoparticles is found to be the SAM of $SH - C_{11} - PEG_3 - OH$, although we observe a higher fraction of non-specific TPM for this coating. In addition, the presence of the dense SAM sometimes results in poor attachment of the nanorods to the substrate, causing “wiggling” particles. Such wiggling particles can be identified before introducing the spheres, and thus can be discarded from the analysis. For the later measurements shown in this chapter the permanent and strong binding of gold spheres is not an issue because of the lack of dynamics in the signal, and we will see that these non-specific TPM can be separated from hairpin dynamics based on its short timescales.

6.2.2 Anti-fouling against nanoparticle-DNA interactions

We now focus on the antifouling properties of the nanoparticles against the non-specific sticking of ssDNA. We characterize interactions of coated nanoparticles with a non-modified ssDNA (Table 6.1). All experiments were performed in the flow cell in citric acid buffer of pH 3 with additional 1 M of NaCl. We pump the ssDNA analyte into the flow cell using a syringe pump at a flowrate of 100 µL/min. After completely filling the flow channel we turn off the pump and monitor the plasmon shift as a function of time.

We measured dynamic plasmon shifts of individual nanorods using a SLD (793 nm) during their interaction with 1 µM of non-modified ssDNA. As in Chapter 3 these measurements convert plasmon shifts to a change in the scattered intensity, which is quantified by plotting the contrast equal to

$$\text{contrast} = \frac{I_{\text{final}} - I_{\text{initial}}}{I_{\text{initial}}}, \tag{6.1}$$

as a function of measured plasmon wavelength of each individual particle, see Figure 6.5**:** Plasmon shift contrasts (see Eqn 6.1) induced by non-specific binding of non-modified ssDNA. We find a relatively strong non-specific sticking of the non-modified ssDNA to bare gold nanorods characterized by a maximum contrast of $\sim 10\,\%$ (equivalent to a plasmon shift of $\Delta SP \approx 4\text{ nm}$). By functionalizing the nanorods with SH – PEG$_n$ – OH we find a mild suppression of

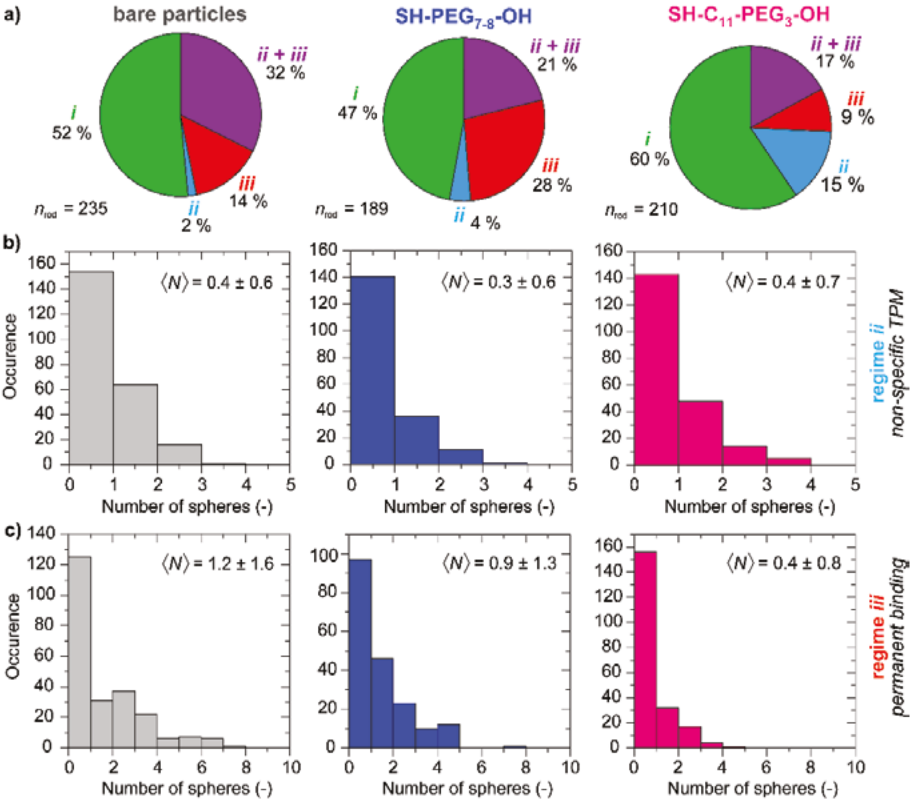

Figure 6.4: a) Relative occurrence of individual signal regimes of different antifouling coatings of gold nanoparticles. Histograms of the number of non-specifically tethered **b)** and permanently bound **c)** spheres detected on single gold nanorods.

non-specific interactions, whereas the SAM composed of $SH - C_{11} - PEG_3 - OH$ does not reveal a detectable contrast (equivalent to a plasmon shift of $\Delta SP < 1.0$ nm).

We conclude that the best antifouling is achieved for $SH - C_{11} - PEG_3 - OH$. Although the molecular weight of the compared PEG molecules is approximately the same, their anti-fouling performance differs significantly. Regular PEG on a gold surface adopts a *mushroom-like* conformation even at high functionalization densities which results in a poor organization of the molecular layer.[320–322] PEG molecules with a carbon chain easily adopt a *brush-like* conformation by self-assembly, resulting in a more organized molecular layer that is more resistant toward non-specific interactions. In addition, the commercial availability of SAM PEG enables us to introduce a functional group into the molecular layer by introducing i.e. $SH - C_{11} - PEG_5 - N_3$ or $SH - C_{11} - PEG_5 - COOH$ providing control over the number of functional groups by employing mixed SAMs. The next section describes how click chemistry targeting these specific functional groups was used to assemble the dimer.

ssDNA sequence (from 5' to 3')	**Length**
CTG TAC GCC ACA TAA GTA AGT CGG AGT GCT GCA	33 nt

Table 6.1: Used ssDNA sequence to test antifouling coating of gold nanorods against unmodified ssDNA.

6.2.3 Specificity of hairpin conjugation

Click-chemistry uses the 1,3-dipolar cycloaddition between azides and cyclooctynes creating a covalent bond (Figure 6.2d),[323–327] where a high efficiency of the reaction is reported for the use of dibenzocyclooctyne (DBCO).[328,329] We quantified the specificity of the conjugation of DBCO-ssDNA to immobilized gold nanorods using (1) the approaches developed in Chapter 3 based on plasmon sensing, and (2) the approaches developed in Chapter 4 based on quantitative single-molecule counting.

For the verification using plasmon sensing we functionalized immobilized gold nanorods with a SAM of $SH - C_{11} - PEG_5 - N_3$ for 1 hour at 10 mM in PBS. The PEG-azide coated nanorods were exposed to 1 μM of a DBCO-ssDNA solution (15 nt, citric acid buffer of pH 3 and 1 M of additional NaCl) for 1 hour, and as a control we used an un-modified ssDNA of the same sequence (Table 6.2).

In Figure 6.6a-d we plot the contrast in scattered intensity after 300 seconds of ssDNA functionalization. We observe a large difference in plasmonic contrast (> 10 x) between the experiments employing DBCO-DNA and the control with non-modified ssDNA. These results are in line with previous experimental data obtained for the $SH - C_{11} - PEG_3 - OH$ coating, and confirm that non-modified ssDNA does not non-specifically interact with the azide groups on the particle.

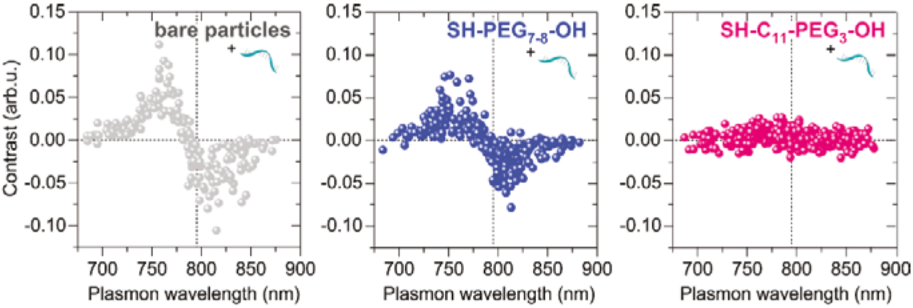

Figure 6.5: Plasmon shift contrasts (see Eqn 6.1) induced by non-specific binding of non-modified ssDNA.

However, we do observe significant binding of DBCO-ssDNA to the SAM of SH – C_{11} – PEG_3 – OH (Figure 6.6c) giving at most 50 % of the signal compared to azide-functionalized nanorods. To confirm that the non-specific interactions are indeed caused by the DBCO group we performed control experiments for non-modified DNA, and in line with Figure 6.5**:** Plasmon shift contrasts (see Eqn 6.1) induced by non-specific binding of non-modified ssDNA we find no measurable binding (Figure 6.6d). We hypothesize that the non-specificity is the direct result of the hydrophobicity of the DBCO group causing it to stick to surfaces.

We further quantified the specificity of the DBCO-ssDNA conjugation using the single-molecule counting approaches developed in Chapter 4. Immobilized gold nanorods were functionalized with a mixture of SH – C_{11} – PEG_3 – OH and SH – C_{11} – PEG_5 – N_3 at varying mixing ratios with a total ligand concentration of 10 mM, and subsequently functionalized with DBCO-ssDNA using the protocol described above.

We then introduced the imager strand (Table 6.2), and performed qPAINT experiments as in Chapter 4 to count the apparent number of ssDNA on each individual particle. The results are shown in Figure 6.6e for varying mixing ratios. Particularly for low azide-content we find a number of ssDNA docking strands well above the expected number that was estimated based on the footprint of the PEG (diagonal line in Figure 6.6e) and the fraction of azides.

ssDNA strand	**Length**	**Sequence** (from 5’ to 3’)
Modified strand (= docking strand)	15 nt	DBCO - CCA ATA ATA CAT CTA
Non-modified strand	15 nt	CCA ATA ATA CAT CTA
Imager strand	10 (9) nt	ATTO 647N – C TAG ATG TAT

Table 6.2: SsDNA sequences employed to study specificity of click-chemistry conjugation. Complimentary sequences are shown in red.

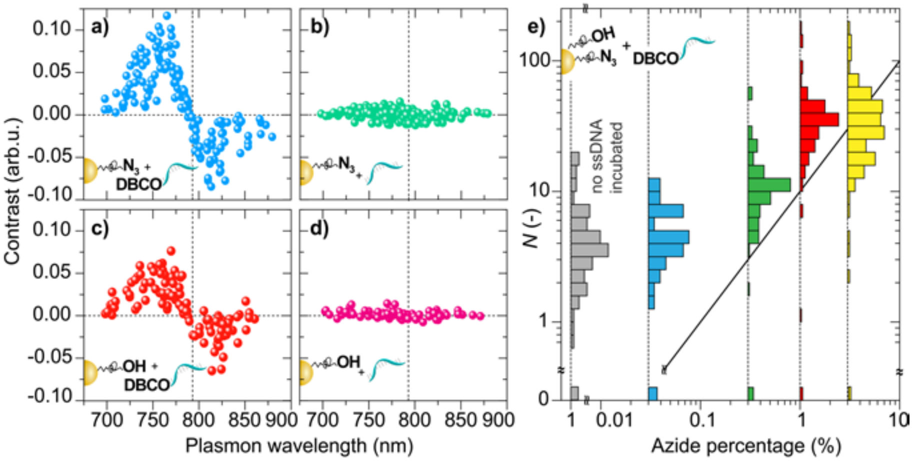

Figure 6.6: a - d) Observed relative change in scattered intensity at 793 nm (contrast, see eqn. 6.1) induced by ssDNA (15 nt) binding to gold nanorods after 300 seconds of incubation measured. **e)** qPAINT measurements of click-chemistry functionalization. The diagonal black line indicates the estimated number of functional groups based on their footprint and mixing ratio.

This again suggests a contribution of non-specifically attached DBCO-DNA, in combination with non-specific interactions of the imager strand with the azide-functionalized nanorods.

To quantify the latter we used azide coated nanorods (fraction of azides 1 %) without any further functionalization with DBCO-ssDNA and count an average of 5 ssDNA per particle, even though no ssDNA functionalization was performed (grey histogram in Figure 6.6e). Since our earlier measurement showed that there is a negligible sticking of unmodified ssDNA to the PEG-SAMs, we hypothetise that the non-specific sticking of the imager strand is induced by the fluorescent dye. These experiments indicate that at low fractions of incorpoorated azide the contribution due to non-specifically attached DBCO-ssDNA is not negligable, but that this effect reduces at higher azide fractions.

6.2.4 Complete dimer assembly

As we established reliable antifouling coating of the nanoparticles based on PEG, and achieved reasonably specific coupling of ssDNA to the rods using click chemistry, we now proceed to assemble the dimer as a whole. As a tether we use an ssDNA hairpin with a stem of 10 complementary nucleotides, and a loop of 30 nt consisting of only cytosine (Table 6.3). To reduce steric hindrance close to the nanoparticle surface we further incorporate thymine spacers of 8 nt on both sides of the hairpin sequence. Note that the spacers are the only difference with the tether modelled theoretically in Chapter 5. To enable orthogonal conjugation to the rod and the sphere, the ssDNA is modified with DBCO for rod-conjugation and with an amine for sphere-conjugation.

ssDNA sequence (from 5' to 3')	**Length**
DBCO – TTTTTTTT CAT GTA CTA G CCC CCC CCC CCC CCC CCC CCC CCC CCC CCC CTA GTA CAT G TTTTTTTT – NH_2	66 nt

Table 6.3: SsDNA hairpin sequence used in our experiments, complementary stem bases are shown in red color.

Gold nanospheres were functionalized in solution using protocols described in previous paragraphs with 10 % of $SH - C_{11} - PEG_5 - COOH$ mixed into the antifouling coating. The antifouling coating itself consisted of an equal fraction of $SH - PEG_n - OH$ (n = 7-8) and $SH - C_{11} - PEG_3 - OH$ which we found to be beneficial for colloidal stability. The nanospheres are incubated in millimolar concentrations of EDC and NHSS at pH 6 for 15 minutes, after which the pH was elevated to 7.5 to facilitate overnight coupling to a 10-fold molar excess of amine-functionalized hairpin. Assuming a typical EDC/NHSS coupling efficiency of 30% this will result in an average of 3 ssDNA hairpins per nanosphere.

Repeated centrifugation was used to remove excess chemicals, and the particles were redispersed in PBS with 500 mM additional NaCl. Gold nanospheres with coupled ssDNA are then introduced into the flow cell at a particle concentration of 5 nM, where they can bind to coverslip immobilized gold nanorods functionalized with a 10% fraction of azides using copper-free click-chemistry. The nanorods incubation in the nanosphere solution was recorded using SLD illumination at 793 nm, and collecting the scattering signal with 50 ms integration time.

In Figure 6.7 we again classify the behavior observed in the three kinetic regimes defined earlier: *i* the temporary sphere binding, *ii* dynamic signals due to TPM, and *iii* the permanent sticking of spheres. Two exemplary timetraces are shown in Figure 6.8. In the experiments where the ssDNA hairpin is present we observe a drastic increase in nanosphere interactions, evidenced by the near-disappearance of the "non-reactive" regime *i*. In addition, we observe an increase in the number of nanospheres performing dynamic behavior from $\overline{N}_{\mathrm{control}} = 0.4 \pm 0.6$ in the absence, versus $\overline{N}_{\mathrm{ssDNA}} = 1.8 \pm 0.9$ in the presence of the ssDNA hairpin (Figure 6.7b). The efficiency of the click-chemistry conjugation is further proved by the large increase in permanent binding of nanospheres decorated with ssDNA hairpin (Figure 6.7c). Here we find $\overline{N}_{\mathrm{ssDNA}} = 2.2 \pm 1.5$ spheres per single nanorod in contrast to $\overline{N}_{\mathrm{control}} = 0.5 \pm 0.8$ when no ssDNA hairpin was present.

6.3 Hairpin dynamics

The permanent binding of sphere is unwanted due to induced steric hindrance and corresponding plasmon detuning reduces SNR of the sensor. Nevertheless, as the biggest challenge we identify regime *ii)* where the spheres

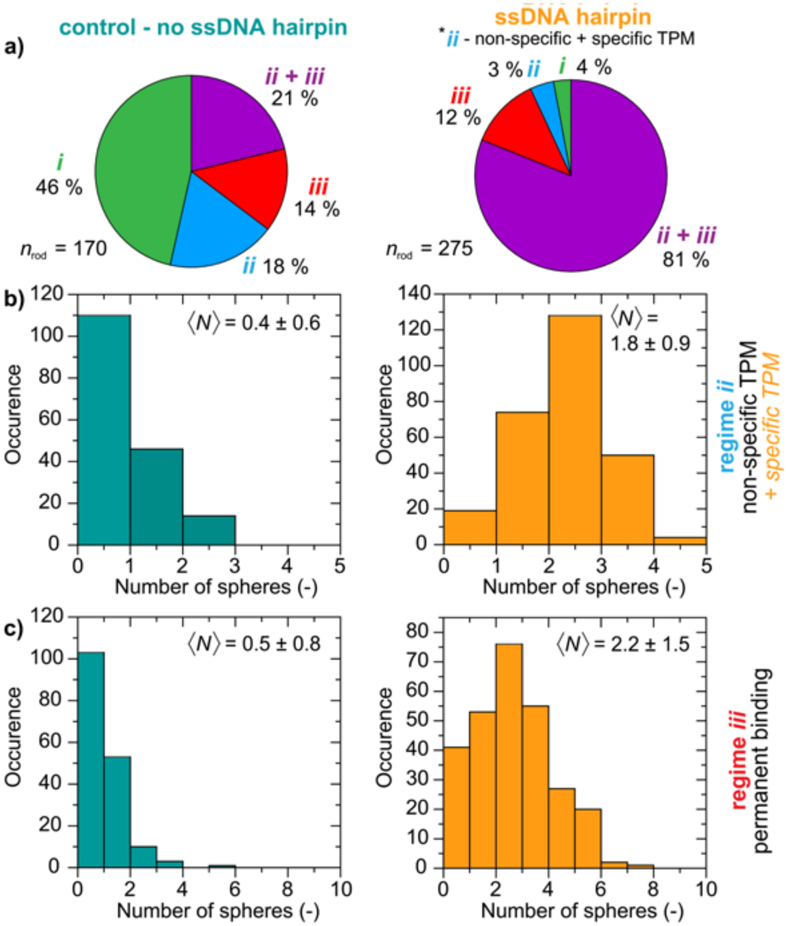

Figure 6.7: Analysis of kinetic regimes in the single nanorod timetraces for interaction with spheres either with or without ssDNA hairpin. **a)** Relative occurrence of kinetic regimes, and detailed quantification of the regimes of **b)** TPM and **c)** permanently bound nanospheres.

perform dynamic behaviour that can be either due to hairpin dynamics, or due to weak and recurring interactions between the nanosphere and the nanorod. Two rather typical timetraces are plotted in Figure 6.8a. A time-varying signal with periods of dynamic signal fluctuations are observed, spaced by periods of time in which the signal appears stable. We identified and subsequently cropped time-frames where dynamics is observed, and extracted the timescales on which the fluctuations occur using autocorrelation analysis. The autocorrelation function was fitted with a single exponential to yield a characteristic lag time τ_{ACF}

$$ACF = a_0 + a \exp\frac{-t}{\tau_{\mathrm{ACF}}}, \qquad 6.2$$

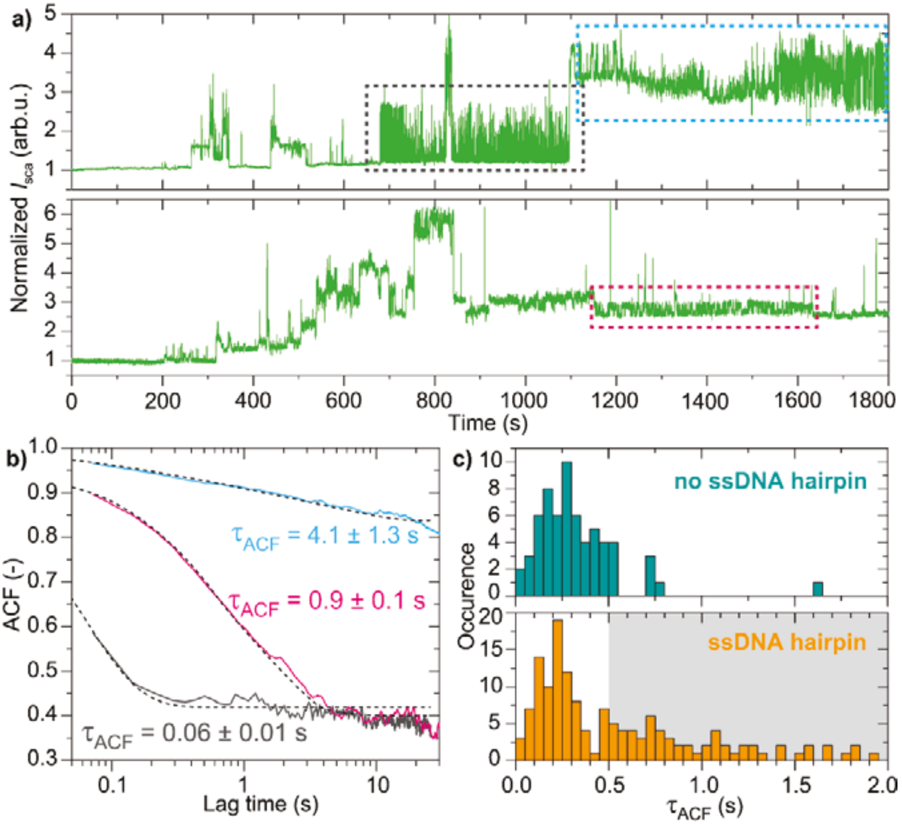

Figure 6.8: a) Two examples of typical timetraces showing functionalization of gold nanorods with ssDNA hairpin coupled nanospheres. Dashed regions indicate nanospheres performing a TPM. **b)** Analysis of these TPM time-frames using autocorrelation of the plasmonic signal with corresponding single exponential fits. **c)** Histograms of characteristic ACF times. Note that here we inthe region from 0 to 2 seconds, uncorrelated signals typically yield characteristic ACF times of 10 – 100 seconds which we do not consider in this analysis.

where a_0 and a are constants, and the characteristic correlation time is related to the association (k_{on}) and dissociation rate (k_{off}) of the 10 nt stem region via:[330]

$$\tau_{\mathrm{ACF}} = \frac{1}{k_{\mathrm{off}} + k_{\mathrm{on}}}. \qquad 6.3$$

In Figure 6.8b three autocorrelation functions are shown with their corresponding fits. The figure illustrates a large variety of timescales present in our measurement ranging from tens of milliseconds to tens of seconds. We perform autocorrelation analysis on all identified time-windows where fluctuating signals were observed, and plot the distribution of characteristic lag times in Figure 6.8c. We exclude the population of

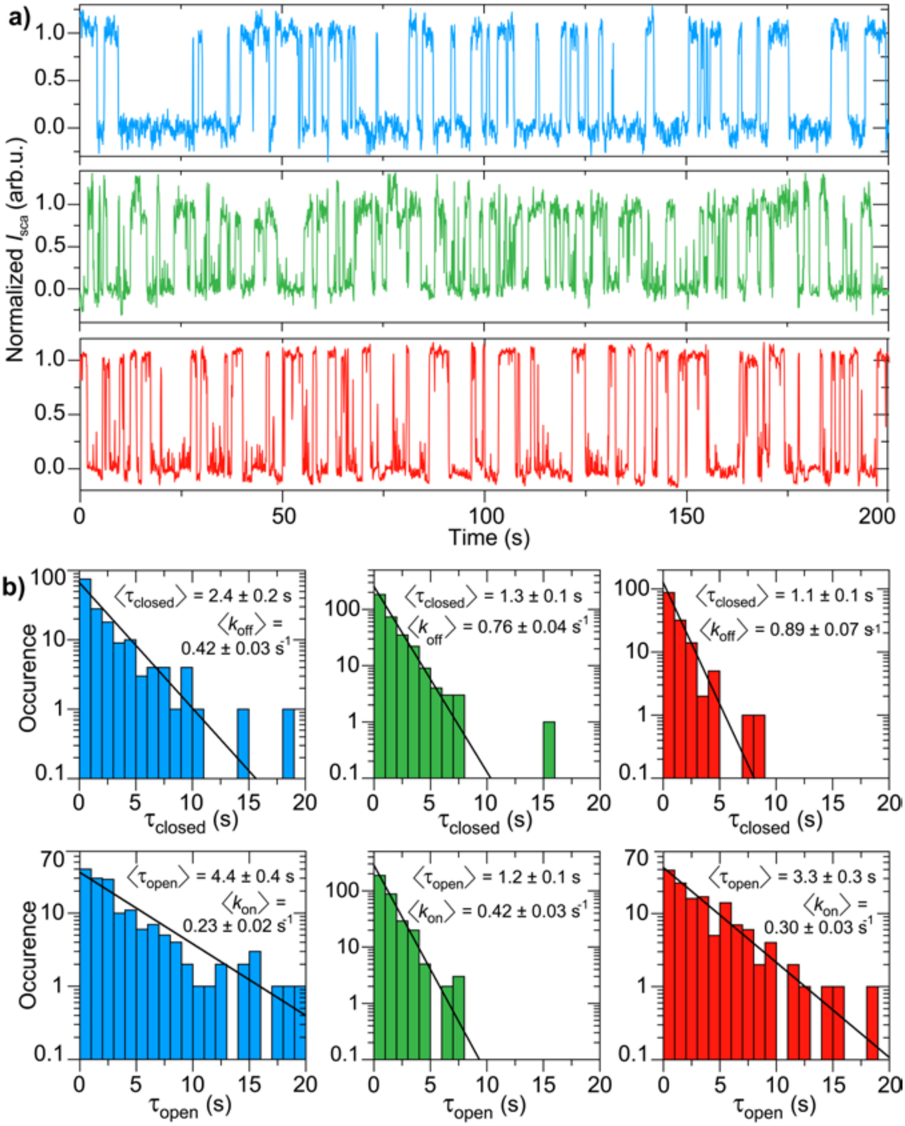

Figure 6.9: Three examples of two-state switching behavior, and the extracted distributions of dwell times in the open and closed state.

timetraces that $\tau_{\mathrm{ACF}} > 10$ s because these are likely caused by a combination of small drifts and/or randomly fluctuating signals. A subpopulation of characteristic lag times with a mean of ~ 1 s is exclusively present when nanospheres were incubated in the presence of the hairpin. This strongly suggest that the fluctuations are caused by hairpin switching dynamics, which we further investigate.

From this subpopulation, three typical timetraces are plotted in Figure 6.9a, where we observe in all cases a dynamic switching between two distinct (normalized) signal levels. This behavior typically lasts for minutes to hours after which the tethered sphere either permanently sticks to the rod or the substrate, or detaches.

To confirm that this behavior is indeed caused by hairpin switching we threshold the timetraces and extract the dwell times in the open and closed states. The detuning between the 793 nm probe wavelength and the (measured) plasmon resonance of each particle was used to identify whether the high or low signal level corresponds to the open state. The distributions of dwell times including a single-exponential fit are shown in Figure 6.9b.

The histogram of dwell times exhibits a single-exponential character, as expected for a molecular interaction with a well-defined rate constant. The average dwell time in the closed state is closely related to the affinity of the 10 nt complementary stem region. The average dwell time and dissociation rate k_{off} can then be estimated from the Gibbs free energy ΔG of the stem sequence responsible for the hybridization:

$$\tau_{\mathrm{closed}}^{\mathrm{theory}} = \frac{1}{k_{\mathrm{off}}^{\mathrm{theory}}} = \frac{1}{k_0} \exp\left(\frac{-\Delta G}{k_b T}\right), \tag{6.4}$$

where $k_0 \cong 3 \cdot 10^6$,[92] and for the complementary sequence and experimental conditions (ionic strength of 1 M) we find $\Delta G = -8.87$ kcal·mole^{-1}.[331,332] This gives a predicted average dwell time in the closed state of $\tau_{\mathrm{closed}}^{\mathrm{theory}} \cong 1$ s corresponding to a dissociation rate of $k_{\mathrm{off}}^{\mathrm{theory}} = 1$ s^{-1}. These predicted values are in excellent agreement with the measured values. Note that the association rate k_{on} of the hairpin cannot be easily predicted from the sequence only but also depends on the accessibility of the stem parts of the sequence, and their relative distance and thus the loop length.

6.4 Conclusion

We have presented a method to monitor the assembly of nanorod-nanosphere heterodimers in-situ using scattering microscopy, and probe the ensuing conformational dynamics of the interconnecting hairpin. Optimization of the anti-fouling coating is crucial in these systems, where we found that self-assembled-monolayers of PEG outperform regular PEG coatings. The hairpin is then conjugated using two orthogonal crosslinking chemistries: EDC/NHS coupling in combination with copper-free click chemistry. The latter particularly resulted in a fraction of non-specific interactions between the (hydrophobic) DBCO groups and the coating.

We nevertheless observed dynamic behavior that we classified based on the characteristic timescales in the autocorrelation function. Constructs with characteristic times of 1-2 seconds were only present in the experiment where the interconnecting ssDNA contained a hairpin, and were therefore ascribed to hairpin switching. The dwell times in the open and closed states were found to be nearly exponentially distributed with the expected mean, which provides a second observation that is in line with single-molecule switching behavior.

Although we clearly detect ssDNA hairpin switching behavior in our signal it appeared particularly challenging to suppress non-specific interactions between the different components in the system. In addition, the current molecular coupling protocols are not yet developed well enough to yield controlled monovalent functionalization of nanoparticles with molecular ligands. The requirement of monovalent functionalization is however crucial for successful probing of transition paths at short timescales. These aspects will be discussed in more detail in the next chapter, where we look beyond and define follow-up research.

7 CONCLUSION AND OUTLOOK

Biomolecules, and their ability to adopt a specific conformation and thus self-regulate, are the basis of many biological processes. Molecular folding has been investigated using single-molecule techniques providing the opportunity to study biophysical properties that ensemble-averaged techniques cannot. Current measurement methods have been however either limited in applying an external force on the folding molecule or in the accessible timescales (Figure 1.5).

In this thesis we proposed the use of plasmonic nanodimers to study real-time folding of single molecules without the application of an external force. We employed plasmonic gold nanoparticles interconnected by the molecule of interest, which exhibits conformational changes modulating the interparticle distance resulting in an optically detectable shift of the dimer's plasmon resonance. Similar to smFRET, plasmonic dimers act as molecular rulers but with a stable and high photon budget. We explored the ability of plasmonic particle based sensing and investigated the performance of the plasmonic nanodimer theoretically and experimentally. Here we first summarize the main results in this thesis, and subsequently discuss experimental obstacles and challenges to finalize with a perspective on the application of dynamic plasmonic nanorulers in bionanoscience.

7.1 Summary of this thesis

In Chapter 2 we laid down the theory behind plasmons and their hybridization in order to understand the optical response of plasmonics-based nanorulers. We further gave an extensive literature overview of applications of nanorulers, and discussed key advances in the field which potentially lead to real-time observation of molecular (un)folding. To be able to practically design a functional nanoruler system and apply it to probe molecular folding, we develop several experimental, signal processing, and theoretical characterization methods of plasmonic based sensors.

In Chapter 3 we studied the functionalization of gold nanorods with thiolated ssDNA at the single-particle level. We exploited the sensitivity of the plasmon resonance to the local refractive index induced by ssDNA binding using single-particle spectroscopy, and found that the ssDNA coverage varies considerably from particle-to-particle. Interestingly, the functionalization process was unexpectedly heterogeneous, beyond the expected variation due to Poisson statistics. We found kinetic rate constants varying by almost an order of magnitude from particle-to-particle, the origin of which we attributed to variations in the effective charge on the particle surface.

Nevertheless, the absolute number of ligands per particle was not resolved. Therefore in Chapter 4 we developed a method based on quantitative single-molecule interaction kinetics to count the absolute number of ligands on the surface of individual particles. By analysing the waiting-time between single-molecule binding events we quantified the particle functionalization both accurately and precisely for a large range of ligand densities. In line with Chapter 3 we observed significant particle-to-particle differences in functionalization which were dominated by the particle-size distribution for high molecular densities, but are substantially broadened for sparsely functionalized particles. Time-dependent studies showed that ligand reorganization on long timescales drastically reduces the heterogeneity, a process that had remained hidden up to then in ensemble-averaged studies.

The work performed in Chapters 3 and 4 provided us an understanding of interactions of single gold nanoparticles with DNA molecules. The given results yielded an insight into the molecular functionalization process at the single particle level. Data further highlighted that significant particle-to-particle heterogeneity has to be taken into account in applications of functional particles. Importantly, our work provided a direct route for quantification and optimization of coupling protocols. The obtained knowledge on ssDNA functionalization of single nanoparticles was necessary to be able to assemble DNA tethered nanoparticles.

In Chapter 5 we investigated the theoretical performance of the proposed plasmonic nanorulers by numerically evaluating the diffusion of a tethered nanosphere and converting this to the corresponding optical scattering signal. We showed that the proposed plasmonic dimer exhibits sensitivity to conformational changes ranging from one to a few tens of nanometers, comparable to the size of short oligonucleotides and small proteins. In principle the distance sensitivity can be further tuned by employing nanoparticles with different sizes, and thus modulate applicable length-scales. Importantly, the long range over which plasmon shifts are found allows, to incorporate short molecular spacers between the folding molecule and the plasmonic components to reduce steric effects that might affect the conformational dynamics.

The numerical study in Chapter 5 demonstrated that experimental timescales in the low microsecond regime are accessible. Unlike smFRET, signal intensity and shotnoise are not the limiting factor, but rather the fluctuations induced by the diffusing of the tether particle through the near-field of the rod.

Our theoretical work established design rules like particle size and tether molecule length to successfully observe conformational transitions. In Chapter 6 we investigated the experimental assembly of the plasmonic heterodimer using a large gold nanorod (20 x 75 nm^2) immobilized to a coverslip and a small tethered sphere (diameter 20 nm). As a model system we used a ssDNA hairpin. After optimization of the particle antifouling coating we experimentally resolved hairpin switching. The measured dwell times in the closed and open states were in good agreement with theoretical expectations.

Microsecond time resolution however hasn't been reached yet experimentally mainly due to complexity of the employed chemical environment, and limitations in the detector bandwidth. In following paragraphs we comment on the current limiting factors and discuss further advances required for successful application of plasmonic nanodimers to observe molecular transitions in real-time.

7.2 Challenges and further research

Several obstacles remain to be overcome for the successful implementation of plasmonic nanorulers to probe conformational dynamics in real-time. Here we describe the main challenges that could be addressed in future research.

7.2.1 Quantified and specific particle functionalization

A challenge that we addressed in Chapters 3 and 4 that requires more research is the quantitative and homogeneous functionalization of particles. This challenge includes the control over the number of functional groups per particle and its antifouling coating. The latter is a molecular layer that should prevent non-specific interactions between the chemically diverse interfaces associated with the nanoparticles, biomolecules, and substrate. It appears that the optimum antifouling coating depends on the type of nanoparticle and its stabilizer, and strongly depends on the particle shape size, and material. A promising alternative to PEG-based antifouling coatings are zwitterionic ligands as pioneered by the group of Whitesides.[333,334] Zwitterionic materials as a new class of emerging materials have recently been developed and applied to a broad range of biomedical and engineering applications.[335–337] Zwitterionic materials possess a unique molecular structure combining both cationic and anionic groups with overall charge neutrality and high hydrophilicity.

Mixed into this antifouling coating we require functional groups that provide handles for the tether biomolecule. Ideally monovalent molecular functionalization in the plasmonic nanoruler is necessary for their proper functioning. Modern nanotechnology methods enable a precise placement of molecules using e.g. an AFM tip,[338,339] or nanoscale UV lithography.[340] Although spatially controlled functionalization on the nanoscale can be achieved, these methods are limited in throughput and not available in most of biophysics labs.

Wet-chemical functionalization protocols have relied on quantification at the ensemble average level which restricts a precise control. Solution-phase synthesis and subsequent purification of specifically labeled nanoparticles is not trivial and often results in a low yield. In Chapter 4 we designed single-molecule method to quantify the functionalization of single nanoparticles with molecular ligands in absolute terms. This lays down a path for a further research towards optimized molecular coupling protocols and molecularly controlled colloidal interfaces with minimized inter-particle differences. Particularly combining the single-molecule counting methods outlined in Chapter 4 with super-resolution localization microscopy is a promising avenue.[282,285] Such direct visualization of the molecular functionalization at the single-particle and single-molecule level provides valuable feedback to optimize functionalization protocols.

7.2.2 Heterogeneous plasmonic response

The scattered signal of plasmonic nanoparticles depends on the particle size, the plasmon wavelength, and the particle orientation in the (often polarized) excitation field. Every colloidal sample of gold nanoparticles consists of particles with a distribution of sizes introducing heterogeneity into the optical response. To be able to interpret the optical signals we have calibrated our sensor single-particle spectroscopy. For practical applications however better shape control in nanoparticle synthesis, and quantitative control of the optical response are crucial. Recently, laser-induced shape transformations have been used to obtain an optically homogeneous ensemble of gold nanorods with an ensemble-averaged linewidth that approximates the single-particle linewidth.[341,342] However, these laser-mediated protocols require further optimization to be reliably and generally applicable to a range of particle shapes and sizes.

To reduce the heterogeneity in detected signals the control over the alignment of nanoparticles and the evanescence field polarization is also desired. This could be implemented using lithography techniques,[343] which offer the possibility to deposit individual particles in lithographically defined “pits” using high-throughput solution-based protocols. Another avenue is to employ lithographically defined nanoparticles, wherein electron-beam lithography can be used to create aligned nanostructures over large areas, albeit at the expense of sensitivity due to the reduce Q-factor of the plasmon resonance due to electron scattering off grain boundaries.[344,345]

7.2.3 Improved data analysis

We showed theoretical possibility of plasmonic nanoruler to access real-time molecular folding. An associated challenge is then related to the real-time processing and analysis of the experimental data. Optimized data processing algorithms and enhanced computational hardware are of a great need due to the large computation demands coming from the large span of recorded timescales and the large datasets (100s of Gb per minute) provided by state-of-the-art high-speed cameras.

Current data analysis techniques are effective at extracting two-state system information (*i.e.* - on or off, bound or unbound, etc.). Of course, even simple biological systems can contain several states and this information is difficult to obtain with data processing methods to-date. Step finding algorithms based on hidden Markov models enable to extract kinetic information of multiple states although their number has to be know a priori.[315,346,347]. We foresee that AI or deep learning algorithms may provide the answer by their ability to rapidly process and analyze large amounts of data without a-priori knowledge of the number of states.[348]

7.2.4 Effect of volume exclusion forces

As a system based on Brownian diffusion of a tethered nanoparticle the force-free conditions are met when the molecular conformational transitions occure at timescales longer then the characteristic diffusion time at which the particle diffuses its full, tether-permitted space. If the timescales are similar or shorter the molecule starts to experience a hydrodynamic drag that might influence the folding dynamics. This was investigated in detail in Chapter 5 and quantified by the autocorrelation time of the tethered sphere.

The presence of the particles however restricts the accessible conformations of the tether molecule somewhat compared to the free molecule. This results in a small but perhaps not negligible exerted net-force, the volume exclusion force.[349] As the particle is excluded from the proximate solid surface it results in an entropic force that the molecule experiences. Contrary to the short-lived and randomized “Brownian forces” the volume exclusion force is a net non-zero force that scales with the distance to the excluded volume. For the tethered nanoparticles of 20 nm and counter length of 66 nt, which we investigated in Chapter 5 and 6, we obtain a net external force of ~ 400 fN. Models are only available for a spherical tether particle near a flat surface, but in the case of a plasmonic dimer the second particle surface is not flat but curved. This volume exclusion force is then expected to be even lower, but quantitation of this force will require further numerical simulations using e.g. molecular dynamics.[350,351] Nevertheless, this force is substantially lower compared to the force used in mechanical single-molecule methods where the lowest limit is set by optical tweezers to ~ 10 pN. As already pointed out the absolute exterted force on the molecule varies significantly with its length. This together with the Brownian diffusion force at different timescales deserves further research.

8 REFERENCES

[1] D. Clark, N. Pazdernik, *Molecular Biology*, Academic Cell, Burlington, **2012**.

[2] N. Plattner, F. Noé, *Nat. Commun.* **2015**, *6*, DOI 10.1038/ncomms8653.

[3] S.-J. Chen, *Annu. Rev. Biophys.* **2008**, *37*, 197.

[4] G. Bao, S. Suresh, *Nat. Mater.* **2003**, *2*, 715.

[5] E. Nudler, A. S. Mironov, *Trends Biochem. Sci.* **2004**, *29*, 11.

[6] W. C. Winkler, *Curr. Opin. Chem. Biol.* **2005**, *9*, 594.

[7] D. D. Boehr, R. Nussinov, P. E. Wright, *Nat. Chem. Biol.* **2009**, *5*, 789.

[8] H. Frauenfelder, S. G. Sligar, P. G. Wolynes, *Science (80-.).* **1991**, *254*, 1598.

[9] J. Ferina, V. Daggett, *J. Mol. Biol.* **2019**, *431*, 1540.

[10] S. Piana, J. L. Klepeis, D. E. Shaw, *Curr. Opin. Struct. Biol.* **2014**, *24*, 98.

[11] C. D. Snow, H. Nguyen, V. S. Pande, M. Gruebele, *Nature* **2002**, *420*, 102.

[12] D. E. Shaw, P. Maragakis, K. Lindorff-larsen, S. Piana, Y. Shan, W. Wriggers, **2010**, *330*, 341.

[13] T. Cellmer, M. Buscaglia, E. R. Henry, J. Hofrichter, W. A. Eaton, *Proc. Natl. Acad. Sci. U. S. A.* **2011**, *108*, 6103.

[14] M. B. Prigozhin, M. Gruebele, *Phys. Chem. Chem. Phys.* **2013**, *15*, 3372.

[15] J. Kubelka, J. Hofrichter, W. A. Eaton, *Curr. Opin. Struct. Biol.* **2004**, *14*, 76.

[16] R. B. Best, *Curr. Opin. Struct. Biol.* **2012**, *22*, 52.

[17] P. L. Freddolino, F. Liu, M. Gruebele, K. Schulten, *Biophys. J.* **2008**, *94*, 75.

[18] K. Lindorff-Larsen, S. Piana, K. Palmo, P. Maragakis, J. L. Klepeis, R. O. Dror, D. E. Shaw, *Proteins Struct. Funct. Bioinforma.* **2010**, *78*, 1950.

[19] D. E. Shaw, R. O. Dror, J. K. Salmon, J. P. Grossman, K. M. MacKenzie, J. A. Bank, C. Young, M. M. Deneroff, B. Batson, K. J. Bowers, E. Chow, M. P. Eastwood, D. J. Ierardi, J. L. Klepeis, J. S. Kuskin, R. H. Larson, K. Lindorff-Larsen, P. Maragakis, M. A. Moraes, S. Piana, Y. Shan, B. Towles, *Proc. Conf. High Perform. Comput. Networking, Storage Anal. SC '09* **2009**, 1.

[20] K. Lindorff-Larsen, S. Piana, R. O. Dror, D. E. Shaw, *Science (80-.).* **2011**, *334*, 517.

[21] M. Sadqi, L. J. Lapidus, V. Muñoz, *Proc. Natl. Acad. Sci. U. S. A.* **2003**, *100*, 12117.

[22] S. Williams, T. P. Causgrove, R. Gilmanshin, K. S. Fang, R. H. Callender, W. H. Woodruff, R. B. Dyer, *Biochemistry* **1996**, *35*, 691.

[23] P. A. Thompson, W. A. Eaton, J. Hofrichter, *Biochemistry* **1997**, *36*, 9200.

[24] K. Chattopadhyay, E. L. Elson, C. Frieden, *Proc. Natl. Acad. Sci. U. S. A.* **2005**, *102*, 2385.

[25] S. J. Hagen, J. Hofrichter, A. Szabo, W. A. Eaton, *Proc. Natl. Acad. Sci. U. S. A.* **1996**, *93*, 11615.

[26] J. D. Bryngelson, J. N. Onuchic, N. D. Socci, P. G. Wolynes, *Proteins Struct. Funct. Bioinforma.* **1995**, *21*, 167.

[27] K. W. Plaxco, K. T. Simons, D. Baker, *J. Mol. Biol.* **1998**, *277*, 985.

[28] V. Muñoz, W. A. Eaton, *Proc. Natl. Acad. Sci. U. S. A.* **1999**, *96*, 11311.

[29] A. N. Naganathan, V. Muñoz, *J. Am. Chem. Soc.* **2005**, *127*, 480.

[30] M. S. Li, D. K. Klimov, D. Thirumalai, *J. Phys. Chem. B* **2002**, *106*, 8302.

[31] D. N. Ivankov, S. O. Garbuzynskiy, E. Alm, K. W. Plaxco, D. Baker, A. V. Finkelstein, *Protein Sci.* **2003**, *12*, 2057.

[32] J. X. Zhang, J. Z. Fang, W. Duan, L. R. Wu, A. W. Zhang, N. Dalchau, B. Yordanov, R. Petersen, A. Phillips, D. Y. Zhang, *Nat. Chem.* **2018**, *10*, 91.

[33] V. A. Voelz, M. Jäger, S. Yao, Y. Chen, L. Zhu, S. A. Waldauer, G. R. Bowman, M. Friedrichs, O. Bakajin, L. J. Lapidus, S. Weiss, V. S. Pande, *J. Am. Chem. Soc.* **2012**, *134*, 12565.

[34] V. Muñoz, M. Cerminara, *Biochem. J.* **2016**, *473*, 2545.

[35] C. M. Dobson, *Annu. Rev. Biochem.* **2019**, *88*, 25.

[36] I. D. Campbell, *Biophysical Techniques*, Oxford University Press, Oxford, **2012**.

[37] A. Hoffmann, K. Neupane, M. T. Woodside, *Phys. Chem. Chem. Phys.* **2013**, *15*, 7934.

[38] J. Schönfelder, D. De Sancho, R. Perez-Jimenez, *J. Mol. Biol.* **2016**, *428*,

4245.

[39] J. Schönfelder, A. Alonso-Caballero, D. De Sancho, R. Perez-Jimenez, *Chem. Soc. Rev.* **2018**, *47*, 3558.

[40] H. S. Chung, *J. Mol. Biol.* **2018**, *430*, 409.

[41] N. Q. Hoffer, M. T. Woodside, *Curr. Opin. Chem. Biol.* **2019**, *53*, 68.

[42] D. T. Edwards, H. Yu, M. G. W. Siewny, T. T. Perkins, A. W. Sanders, *Science (80-.).* **2017**, *355*, 945.

[43] K. C. Neuman, A. Nagy, *Nat. Methods* **2008**, *5*, 491.

[44] Z. N. Scholl, Q. Li, P. E. Marszalek, *Wiley Interdiscip. Rev. Nanomedicine Nanobiotechnology* **2014**, *6*, 211.

[45] A. Borgia, P. M. Williams, J. Clarke, *Annu. Rev. Biochem.* **2008**, *77*, 101.

[46] M. S. Bull, R. M. A. Sullan, H. Li, T. T. Perkins, *ACS Nano* **2014**, *8*, 4984.

[47] C. He, C. Hu, X. Hu, X. Hu, A. Xiao, T. T. Perkins, H. Li, *Angew. Chemie - Int. Ed.* **2015**, *54*, 9921.

[48] D. T. Edwards, J. K. Faulk, A. W. Sanders, M. S. Bull, R. Walder, M. A. Leblanc, M. C. Sousa, T. T. Perkins, *Nano Lett.* **2015**, *15*, 7091.

[49] H. Lei, Y. Guo, X. Hu, C. Hu, X. Hu, H. Li, *J. Am. Chem. Soc.* **2017**, *139*, 1538.

[50] P. Zheng, Y. Wang, H. Li, *Angew. Chemie - Int. Ed.* **2014**, *53*, 14060.

[51] E. J. Guinn, B. Jagannathan, S. Marqusee, *Nat. Commun.* **2015**, *6*, 1.

[52] G. Yuan, H. Liu, Q. Ma, X. Li, J. Nie, J. Zuo, P. Zheng, *J. Phys. Chem. Lett.* **2019**, *10*, 5428.

[53] Z. Wang, J. M. Jumper, K. F. Freed, T. R. Sosnick, *Biophys. J.* **2019**, *117*, 1429.

[54] D. De Sancho, J. Schönfelder, R. B. Best, R. Perez-Jimenez, V. Muñoz, *J. Phys. Chem. B* **2018**, *122*, 11147.

[55] C. Valotteau, F. Sumbul, F. Rico, *Biophys. Rev.* **2019**, *11*, 689.

[56] J. Ma, M. D. Wang, *Biophys. Rev.* **2016**, *8*, 75.

[57] M. T. J. Van Loenhout, M. V. De Grunt, C. Dekker, *Science (80-.).* **2012**, *338*, 94.

[58] A. Tempestini, V. Cassina, D. Brogioli, R. Ziano, S. Erba, R. Giovannoni, M. G. Cerrito, D. Salerno, F. Mantegazza, *Nucleic Acids Res.* **2013**, *41*, 2009.

[59] C. Gosse, T. R. Strick, D. Kostrz, *Curr. Opin. Chem. Biol.* **2019**, *53*, 192.

[60] S. Le, R. Liu, C. T. Lim, J. Yan, *Methods* **2016**, *94*, 13.

[61] H. Chen, G. Yuan, R. S. Winardhi, M. Yao, I. Popa, J. M. Fernandez, J.

Yan, *J. Am. Chem. Soc.* **2015**, *137*, 3540.

[62] D. Dulin, T. J. Cui, J. Cnossen, M. W. Docter, J. Lipfert, N. H. Dekker, *Biophys. J.* **2015**, *109*, 2113.

[63] F. Kriegel, N. Ermann, R. Forbes, D. Dulin, N. H. Dekker, J. Lipfert, *Nucleic Acids Res.* **2017**, *45*, 5920.

[64] K. Neupane, M. T. Woodside, *Biophys. J.* **2016**, *111*, 283.

[65] K. Neupane, D. A. N. Foster, D. R. Dee, H. Yu, F. Wang, M. T. Woodside, *Science (80-.).* **2016**, *352*, 239.

[66] K. Neupane, F. Wang, M. T. Woodside, *Proc. Natl. Acad. Sci.* **2017**, *114*, 1329.

[67] K. Neupane, D. B. Ritchie, H. Yu, D. A. N. Foster, F. Wang, M. T. Woodside, *Phys. Rev. Lett.* **2012**, *109*, 1.

[68] K. Neupane, N. Q. Hoffer, M. T. Woodside, *J. Phys. Chem. B* **2018**, *122*, 11095.

[69] H. Yu, D. R. Dee, X. Liu, A. M. Brigley, I. Sosova, M. T. Woodside, *Proc. Natl. Acad. Sci. U. S. A.* **2015**, *112*, 8308.

[70] A. Solanki, K. Neupane, M. T. Woodside, *Phys. Rev. Lett.* **2014**, *112*, 1.

[71] A. N. Gupta, K. Neupane, N. Rezajooei, L. M. Cortez, V. L. Sim, M. T. Woodside, *Nat. Commun.* **2016**, *7*, 1.

[72] N. Q. Hoffer, K. Neupane, A. G. T. Pyo, M. T. Woodside, *Proc. Natl. Acad. Sci. U. S. A.* **2019**, *116*, 8125.

[73] K. Neupane, N. Q. Hoffer, M. T. Woodside, *Phys. Rev. Lett.* **2018**, *121*, 18102.

[74] K. Neupane, A. P. Manuel, M. T. Woodside, *Nat. Phys.* **2016**, *12*, 700.

[75] K. Neupane, A. P. Manuel, J. Lambert, M. T. Woodside, *J. Phys. Chem. Lett.* **2015**, *6*, 1005.

[76] J. Valle-Orero, J. A. Rivas-Pardo, R. Tapia-Rojo, I. Popa, D. J. Echelman, S. Haldar, J. M. Fernández, *Angew. Chemie - Int. Ed.* **2017**, *56*, 9741.

[77] C. Gu, C. Jia, X. Guo, *Small Methods* **2017**, *1*, 1700071.

[78] Y. Zhao, D. Chen, H. Yue, J. B. French, J. Rufo, S. J. Benkovic, T. J. Huang, *Lab Chip* **2013**, *13*, 2183.

[79] G. He, J. Li, H. Ci, C. Qi, X. Guo, *Angew. Chemie - Int. Ed.* **2016**, *55*, 9036.

[80] G. He, J. Li, C. Qi, X. Guo, *Adv. Sci.* **2017**, *4*, DOI 10.1002/advs.201700158.

[81] X. Chen, C. Zhou, X. Guo, *Chinese J. Chem.* **2019**, *37*, 897.

[82] D. K. Sasmal, L. E. Pulido, S. Kasal, J. Huang, *Nanoscale* **2016**, *8*, 19928.

[83] E. Lerner, T. Cordes, A. Ingargiola, Y. Alhadid, S. Y. Chung, X. Michalet, S. Weiss, *Science (80-.).* **2018**, *359*, DOI 10.1126/science.aan1133.

[84] I. König, A. Zarrine-Afsar, M. Aznauryan, A. Soranno, B. Wunderlich, F. Dingfelder, J. C. Stüber, A. Plückthun, D. Nettels, B. Schuler, *Nat. Methods* **2015**, *12*, 773.

[85] G. Krainer, S. Keller, M. Schlierf, *Curr. Opin. Struct. Biol.* **2019**, *58*, 124.

[86] G. Bonnet, O. Krichevsky, A. Libchaber, *PNAS* **1998**, *95*, 8602.

[87] M. L. Wallace, L. Ying, S. Balasubramanian, D. Klenerman, *J. Phys. Chem. B* **2000**, *104*, 11551.

[88] M. I. Wallace, L. Ying, S. Balasubramanian, D. Klenerman, *Proc. Natl. Acad. Sci. U. S. A.* **2001**, *98*, 5584.

[89] N. L. Goddard, G. Bonnet, O. Krichevsky, A. Libchaber, *Phys. Rev. Lett.* **2000**, *85*, 2400.

[90] T. Xia, J. Yuan, X. Fang, *J. Phys. Chem. B* **2013**, *117*, 14994.

[91] A. Haller, R. B. Altman, M. F. Soulière, S. C. Blanchard, R. Micura, *Proc. Natl. Acad. Sci. U. S. A.* **2013**, *110*, 4188.

[92] R. Tsukanov, T. E. Tomov, R. Masoud, H. Drory, N. Plavner, M. Liber, E. Nir, *J. Phys. Chem. B* **2013**, *117*, 11932.

[93] R. Tsukanov, T. E. Tomov, Y. Berger, M. Liber, E. Nir, *J. Phys. Chem. B* **2013**, *117*, 16105.

[94] E. Kim, S. Lee, A. Jeon, J. M. Choi, H. S. Lee, S. Hohng, H. S. Kim, *Nat. Chem. Biol.* **2013**, *9*, 313.

[95] M. H. Seo, J. Park, E. Kim, S. Hohng, H. S. Kim, *Nat. Commun.* **2014**, *5*, 1.

[96] H. S. Chung, K. McHale, J. M. Louis, W. A. Eaton, B. Lalkens, P. Tinnefeld, *Science (80-.).* **2012**, *335*, 981.

[97] H. S. Chung, W. A. Eaton, *Nature* **2013**, *502*, 685.

[98] H. S. Chung, K. McHale, J. M. Louis, W. A. Eaton, *Science (80-.).* **2012**, *335*, 981.

[99] K. Truex, H. S. Chung, J. M. Louis, W. A. Eaton, *Phys. Rev. Lett.* **2015**, *115*, 1.

[100] I. V. Gopich, A. Szabo, *J. Phys. Chem. B* **2009**, *113*, 10965.

[101] P. C. Nelson, *Curr. Opin. Colloid Interface Sci.* **2007**, *12*, 307.

[102] D. A. Schafer, J. Gelles, M. P. Sheetz, R. Landick, *Nature* **1991**, *352*, 444.

[103] H. Qian, E. L. Elson, *Biophys. J.* **1999**, *76*, 1598.

[104] M. N. Lambert, E. Vöcker, S. Blumberg, S. Redemann, A. Gajraj, J. C. Meiners, N. G. Walter, *Biophys. J.* **2006**, *90*, 3672.

[105] S. Brinkers, H. R. C. Dietrich, F. H. De Groote, I. T. Young, B. Rieger, *J. Chem. Phys.* **2009**, *130*, 1.

[106] C. Zurla, A. Franzini, G. Galli, D. D. Dunlap, D. E. A. Lewis, S. Adhya, L. Finzi, *J. Phys. Condens. Matter* **2006**, *18*, DOI 10.1088/0953-8984/18/14/S07.

[107] B. van den Broek, F. Vanzi, D. Normanno, F. S. Pavone, G. J. L. Wuite, *Nucleic Acids Res.* **2006**, *34*, 167.

[108] C. Zurla, C. Manzo, D. Dunlap, D. E. A. Lewis, S. Adhya, L. Finzi, *Nucleic Acids Res.* **2009**, *37*, 2789.

[109] N. Laurens, S. R. W. Bellamy, A. F. Harms, Y. S. Kovacheva, S. E. Halford, G. J. L. Wuite, *Nucleic Acids Res.* **2009**, *37*, 5454.

[110] J. N. Milstein, Y. F. Chen, J. C. Meiners, *Biopolymers* **2011**, *95*, 144.

[111] F. Vanzi, C. Broggio, L. Sacconi, F. S. Pavone, *Nucleic Acids Res.* **2006**, *34*, 3409.

[112] C. Zurla, T. Samuely, G. Bertoni, F. Valle, G. Dietler, L. Finzi, D. D. Dunlap, *Biophys. Chem.* **2007**, *128*, 245.

[113] G. Lia, M. Indrieri, T. Owen-Hughes, L. Finzi, A. Podesta, P. Milani, D. Dunlap, *J. Biophotonics* **2008**, *1*, 280.

[114] D. Normanno, F. Vanzi, F. S. Pavone, *Nucleic Acids Res.* **2008**, *36*, 2505.

[115] D. Rutkauskas, H. Zhan, K. S. Matthews, F. S. Pavone, F. Vanzi, *Proc. Natl. Acad. Sci.* **2009**, *106*, 16627.

[116] C. Manzo, C. Zurla, D. D. Dunlap, L. Finzi, *Biophys. J.* **2012**, *103*, 1753.

[117] N. Laurens, D. A. Rusling, C. Pernstich, I. Brouwer, S. E. Halford, G. J. L. Wuite, *Nucleic Acids Res.* **2012**, *40*, 4988.

[118] S. Johnson, Y. J. Chen, R. Phillips, *PLoS One* **2013**, *8*, DOI 10.1371/journal.pone.0075799.

[119] K. W. Hsu, S. Y. Chow, B. Y. Su, Y. H. Lu, C. J. Chen, W. L. Chen, M. Y. Cheng, H. F. Fan, *Biochim. Biophys. Acta - Gene Regul. Mech.* **2019**, *1862*, 129.

[120] A. M. Oliveira Paiva, A. H. Friggen, L. Qin, R. Douwes, R. T. Dame, W. K. Smits, *J. Mol. Biol.* **2019**, *431*, 653.

[121] A. A. Drabek, J. J. Loparo, S. C. Blacklow, *Biochemistry* **2019**, *58*, 2509.

[122] E. W. A. Visser, L. J. Van Ijzendoorn, M. W. J. Prins, *ACS Nano* **2016**, *10*, 3093.

[123] P. F. J. May, J. N. M. Pinkney, P. Zawadzki, G. W. Evans, D. J. Sherratt,

A. N. Kapanidis, *Biophys. J.* **2014**, *107*, 1205.

[124] I. Braslavsky, R. Amit, B. M. Jaffar Ali, O. Gileadi, A. Oppenheim, J. Stavans, *Appl. Opt.* **2001**, *40*, 5650.

[125] S. Blumberg, A. Gajraj, M. W. Pennington, J. C. Meiners, *Biophys. J.* **2005**, *89*, 1272.

[126] D. T. Kovari, E. Weeks, D. Dunlap, L. Finzi, *Biophys. J.* **2017**, *112*, 70a.

[127] Michael Faraday, M. Faraday, *Phil. Trans. R. Soc.* **1857**, *147*, 145.

[128] D. R. Bohren, C. F., Huffman, **2008**.

[129] D. Aherne, D. M. Ledwith, M. Gara, J. M. Kelly, *Adv. Funct. Mater.* **2008**, *18*, 2005.

[130] G. Mie, *Ann. Phys.* **1908**, *330*, 377.

[131] W. Li, *Plasmonics* **2018**, *13*, 997.

[132] R. H. Doremus, *J. Chem. Phys.* **1964**, *40*, 2389.

[133] N. G. Khlebtsov, L. A. Dykman, *J. Quant. Spectrosc. Radiat. Transf.* **2010**, *111*, 1.

[134] K. L. Kelly, E. Coronado, L. L. Zhao, G. C. Schatz, *J. Phys. Chem. B* **2003**, *107*, 668.

[135] C. Noguez, *Opt. Mater. (Amst).* **2005**, *27*, 1204.

[136] H. Chen, L. Shao, Q. Li, J. Wang, *Chem. Soc. Rev.* **2013**, *42*, 2679.

[137] O. Schubert, J. Becker, L. Carbone, Y. Khalavka, T. Provalska, I. Zins, C. Sönnichsen, *Nano Lett.* **2008**, *8*, 2345.

[138] P. B. Johnson, R. W. Christry, *Phys. Rev. B* **1972**, *6*, 4370.

[139] C. Sönnichsen, T. Franzl, T. Wilk, G. von Plessen, J. Feldmann, O. Wilson, P. Mulvaney, *Phys. Rev. Lett.* **2002**, *88*, 774021.

[140] M. Liu, P. Guyot-Sionnest, T. W. Lee, S. K. Gray, *Phys. Rev. B - Condens. Matter Mater. Phys.* **2007**, *76*, 1.

[141] N. Gao, Y. Chen, L. Li, Z. Guan, T. Zhao, N. Zhou, P. Yuan, S. Q. Yao, Q. H. Xu, *J. Phys. Chem. C* **2014**, *118*, 13904.

[142] P. Zijlstra, P. M. R. Paulo, M. Orrit, *Nat. Nanotechnol.* **2012**, *7*, 379.

[143] A. B. Taylor, P. Zijlstra, *ACS Sensors* **2017**, *2*, 1103.

[144] M. Gluodenis, C. A. Foss, *J. Phys. Chem. B* **2002**, *106*, 9484.

[145] D. M. Solís, J. M. Taboada, F. Obelleiro, L. M. Liz-Marzán, F. J. García De Abajo, *ACS Nano* **2014**, *8*, 7559.

[146] P. Nordlander, C. Oubre, E. Prodan, K. Li, M. I. Stockman, *Nano Lett.* **2004**, *4*, 899.

[147] E. Prodan, C. Radloff, N. J. Halas, P. Nordlander, *Science (80-.).* **2003**, *302*, 419.

[148] B. M. Reinhard, M. Siu, H. Agarwal, A. P. Alivisatos, J. Liphardt, *Nano Lett.* **2005**, *5*, 2246.

[149] P. K. Jain, M. A. El-Sayed, *Nano Lett.* **2007**, *7*, 2854.

[150] U. Hohenester, A. Trügler, *Comput. Phys. Commun.* **2012**, *183*, 370.

[151] U. Hohenester, *Comput. Phys. Commun.* **2014**, *185*, 1177.

[152] F. Hao, P. Nordlander, *Chem. Phys. Lett.* **2007**, *446*, 115.

[153] Y. Ekinci, H. H. Solak, J. F. Löffler, *J. Appl. Phys.* **2008**, *104*, DOI 10.1063/1.2999370.

[154] Z. L. Yang, Q. H. Li, F. X. Ruan, Z. P. Li, B. Ren, H. X. Xu, Z. Q. Tian, *Chinese Sci. Bull.* **2010**, *55*, 2635.

[155] M. a. Yurkin, A. G. Hoekstra, *J. Quant. Spectrosc. Radiat. Transf.* **2007**, *106*, 558.

[156] M. a. Yurkin, D. De Kanter, A. G. Hoekstra, *J. Nanophotonics* **2010**, *4*, 041585.

[157] F. J. García de Abajo, A. Howie, *Phys. Rev. B* **2002**, *65*, 115418.

[158] J. Waxenegger, A. Tr??gler, U. Hohenester, *Comput. Phys. Commun.* **2015**, *193*, 138.

[159] V. Myroshnychenko, J. Rodríguez-Fernández, I. Pastoriza-Santos, A. M. Funston, C. Novo, P. Mulvaney, L. M. Liz-Marzán, F. J. García De Abajo, *Chem. Soc. Rev.* **2008**, *37*, 1792.

[160] M. Karamehmedović, R. Schuh, V. Schmidt, T. Wriedt, C. Matyssek, W. Hergert, A. Stalmashonak, G. Seifert, O. Stranik, *Opt. Express* **2011**, *19*, 8939.

[161] T. Hutter, F. M. Huang, S. R. Elliott, S. Mahajan, *J. Phys. Chem. C* **2013**, *117*, 7784.

[162] P. Nordlander, E. Prodan, *Nano Lett.* **2004**, *4*, 2209.

[163] F. Le, N. Z. Lwin, J. M. Steele, M. Käll, N. J. Halas, P. Nordlander, *Nano Lett.* **2005**, *5*, 2009.

[164] F. Benz, B. de Nijs, C. Tserkezis, R. Chikkaraddy, D. O. Sigle, L. Pukenas, S. D. Evans, J. Aizpurua, J. J. Baumberg, *Opt. Express* **2015**, *23*, 33255.

[165] J. J. Mock, R. T. Hill, A. Degiron, S. Zauscher, A. Chilkoti, D. R. Smith, *Nano Lett.* **2008**, *8*, 2245.

[166] R. T. Hill, J. J. Mock, Y. Urzhumov, D. S. Sebba, S. J. Oldenburg, S. Y. Chen, A. A. Lazarides, A. Chilkoti, D. R. Smith, *Nano Lett.* **2010**, *10*, 4150.

[167] R. T. Hill, J. J. Mock, A. Hucknall, S. D. Wolter, N. M. Jokerst, D. R. Smith, A. Chilkoti, *ACS Nano* **2012**, *6*, 9237.

[168] C. Ciracì, R. T. Hill, J. J. Mock, Y. Urzhumov, A. I. Fernández-Domínguez, S. A. Maier, J. B. Pendry, A. Chilkoti, D. R. Smith, *Science (80-.).* **2012**, *337*, 1072.

[169] T. Ding, D. Sigle, L. Zhang, J. Mertens, B. De Nijs, J. Baumberg, *ACS Nano* **2015**, *9*, 6110.

[170] C. Sonnichsen, B. M. Reinhard, J. Liphard, A. P. Alivisatos, *Nat. Biotechnol.* **2005**, *23*, 741.

[171] P. Zijlstra, M. Orrit, *Reports Prog. Phys.* **2011**, *74*, 106401.

[172] L. Xiao, E. S. Yeung, *Annu. Rev. Anal. Chem.* **2014**, *7*, 89.

[173] M. Sriram, K. Zong, S. R. C. Vivekchand, J. Justin Gooding, *Sensors (Switzerland)* **2015**, *15*, 25774.

[174] E. Ringe, B. Sharma, A. I. Henry, L. D. Marks, R. P. Van Duyne, *Phys. Chem. Chem. Phys.* **2013**, *15*, 4110.

[175] A. Zilli, W. Langbein, P. Borri, *ACS Photonics* **2019**, *6*, 2149.

[176] P. Billaud, S. Marhaba, N. Grillet, E. Cottancin, C. Bonnet, J. Lerḿ, J. L. Vialle, M. Broyer, M. Pellarin, *Rev. Sci. Instrum.* **2010**, *81*, DOI 10.1063/1.3340875.

[177] S. S. Lo, H. Y. Shi, L. Huang, G. V. Hartland, *Opt. Lett.* **2013**, *38*, 1265.

[178] D. Boyer, P. Tamarat, A. Maali, B. Lounis, M. Orrit, *Science (80-.).* **2002**, *297*, 1160.

[179] G. S. Qian, T. T. Zhang, W. Zhao, J. J. Xu, H. Y. Chen, *Chem. Commun.* **2017**, *53*, 4710.

[180] S. E. Lee, Q. Chen, R. Bhat, S. Petkiewicz, J. M. Smith, V. E. Ferry, A. L. Correia, A. P. Alivisatos, M. J. Bissell, *Nano Lett.* **2015**, *15*, 4564.

[181] H. Wang, Z. Tang, Y. Wang, G. Ma, N. Tao, *J. Am. Chem. Soc.* **2019**, *141*, 16071.

[182] W. Ye, M. Götz, S. Celiksoy, L. Tüting, C. Ratzke, J. Prasad, J. Ricken, S. V. Wegner, R. Ahijado-Guzmán, T. Hugel, C. Sönnichsen, *Nano Lett.* **2018**, *18*, 6633.

[183] P. C. Ray, Z. Fan, R. A. Crouch, S. S. Sinha, A. Pramanik, *Chem. Soc. Rev.* **2014**, *43*, 6370.

[184] Z. Qian, D. S. Ginger, *J. Am. Chem. Soc.* **2017**, *139*, 5266.

[185] B. M. Reinhard, S. Sheikholeslami, A. Mastroianni, A. P. Alivisatos, J. Liphardt, *Proc. Natl. Acad. Sci.* **2007**, *104*, 2667.

[186] C. A. Tajon, D. Seo, J. Asmussen, N. Shah, Y. W. Jun, C. S. Craik, *ACS*

Nano **2014**, *8*, 9199.

[187] L. R. Skewis, B. M. Reinhard, *Nano Lett.* **2008**, *8*, 214.

[188] D. W. Brandl, N. A. Mirin, P. Nordlander, *J. Phys. Chem. B* **2006**, *110*, 12302.

[189] Y. W. Jun, S. Sheikholeslami, D. R. Hostetter, C. Tajon, C. S. Craik, A. P. Alivisatosa, *Proc. Natl. Acad. Sci. U. S. A.* **2009**, *106*, 17735.

[190] S. J. Hurst, A. K. R. Lytton-Jean, C. a Mirkin, *Anal. Chem.* **2006**, *78*, 8313.

[191] C. a Mirkin, R. L. Letsinger, R. C. Mucic, J. J. Storhoff, *Nature* **1996**, *382*, 607.

[192] A. Ap, J. Kp, P. Xg, W. Te, L. Cj, B. Mp, S. Pg, *Nature* **1996**, *382*, 609.

[193] S. A. Claridge, H. W. Liang, S. R. Basu, J. M. J. Fréchet, A. P. Alivisatos, *Nano Lett.* **2008**, *8*, 1202.

[194] M. X. Li, C. H. Xu, N. Zhang, G. S. Qian, W. Zhao, J. J. Xu, H. Y. Chen, *ACS Nano* **2018**, *12*, 3341.

[195] J. I. L. Chen, Y. Chen, D. S. Ginger, *J. Am. Chem. Soc.* **2010**, *132*, 9600.

[196] J. W. Kim, D. Seo, J. U. Lee, K. M. Southard, Y. Lim, D. Kim, Z. J. Gartner, Y. W. Jun, J. Cheon, *Nat. Protoc.* **2017**, *12*, 1871.

[197] S. E. Kim, B. R. Lee, H. Lee, S. D. Jo, H. Kim, Y. Y. Won, J. Lee, *Sci. Rep.* **2017**, *7*, 1.

[198] K. Kim, J. W. Oh, Y. K. Lee, J. Son, J. M. Nam, *Angew. Chemie - Int. Ed.* **2017**, *56*, 9877.

[199] J. I. L. Chen, H. Durkee, B. Traxler, D. S. Ginger, *Small* **2011**, *7*, 1993.

[200] K. Lee, Y. Cui, L. P. Lee, J. Irudayaraj, *Nat. Nanotechnol.* **2014**, *9*, 474.

[201] Y. Fang, S. Chen, W. Wang, X. Shan, N. Tao, *Angew. Chemie - Int. Ed.* **2015**, *54*, 2538.

[202] X. Shan, Y. Fang, S. Wang, Y. Guan, H. Chen, N. Tao, **2014**, *27*, DOI 10.1021/nl501805e.

[203] Z. Chen, Y. Peng, Y. Cao, H. Wang, J. R. Zhang, H. Y. Chen, J. J. Hu, *Nano Lett.* **2018**, *18*, 3759.

[204] Y. Park, S. Shin, H. Jin, J. Park, Y. Hong, J. Choi, B. Jung, H. Song, D. Seo, *J. Am. Chem. Soc.* **2018**, *140*, 15161.

[205] S. Samai, T. L. Y. Choi, K. N. Guye, Y. Yan, D. S. Ginger, *J. Phys. Chem. C* **2018**, *122*, 13363.

[206] L. H. Dubois, R. G. Nuzzo, *Annu. Rev. Phys. Chem.* **1992**, *43*, 437.

[207] M. a. Beuwer, M. W. J. Prins, P. Zijlstra, *Nano Lett.* **2015**, 150406152516004.

[208] W. P. Hall, S. N. Ngatia, R. P. Van Duyne, *J. Phys. Chem. C* **2011**, *115*, 1410.

[209] Z. Wang, R. Lévy, D. G. Fernig, M. Brust, *Bioconjug. Chem.* **2005**, *16*, 497.

[210] V. Pavlov, Y. Xiao, B. Shlyahovsky, I. Willner, *J. Am. Chem. Soc.* **2004**, *126*, 11768.

[211] J. Liu, Y. Lu, *Angew. Chemie - Int. Ed.* **2005**, *45*, 90.

[212] C. Rosman, J. Prasad, A. Neiser, A. Henkel, J. Edgar, C. Sönnichsen, *Nano Lett.* **2013**, *13*, 3243.

[213] R. Elghanian, J. J. Storhoff, R. C. Mucic, R. L. Letsinger, C. A. Mirkin, *Science (80-.).* **1997**, *277*, 1078.

[214] T. M. Herne, M. J. Tarlov, *J. Am. Chem. Soc.* **1997**, *119*, 8916.

[215] J. J. Storhoff, R. Elghanian, R. C. Mucic, C. A. Mirkin, R. L. Letsinger, *J. Am. Chem. Soc.* **1998**, *120*, 1959.

[216] L. M. Demers, C. A. Mirkin, R. C. Mucic, R. A. Reynolds, R. L. Letsinger, R. Elghanian, G. Viswanadham, *Anal. Chem.* **2000**, *72*, 5535.

[217] J. Liu, Y. Lu, *Nat. Protoc.* **2006**, *1*, 246.

[218] J. Sharma, R. Chhabra, C. S. Andersen, K. V. Gothelf, H. Yan, Y. Liu, *J. Am. Chem. Soc.* **2008**, *130*, 7820.

[219] X. Zhang, M. R. Servos, J. Liu, *J. Am. Chem. Soc.* **2012**, *134*, 7266.

[220] X. Zhang, B. Liu, N. Dave, M. R. Servos, J. Liu, *Langmuir* **2012**, *28*, 17053.

[221] X. Zhang, T. Gouriye, K. Göeken, M. R. Servos, R. Gill, J. Liu, *J. Phys. Chem. C* **2013**, *117*, 15677.

[222] D. H. M. Dam, J. H. Lee, P. N. Sisco, D. T. Co, M. Zhang, M. R. Wasielewski, T. W. Odom, *ACS Nano* **2012**, *6*, 3318.

[223] N. L. Rosi, D. A. Giljohann, C. S. Thaxton, A. K. R. Lytton-Jean, M. S. Han, C. A. Mirkin, *Science (80-.).* **2006**, *312*, 1027.

[224] S. Simoncelli, H. De Alwis Weerasekera, C. Fasciani, C. N. Boddy, P. F. Aramendia, E. I. Alarcon, J. C. Scaiano, *J. Phys. Chem. Lett.* **2015**, *6*, 1499.

[225] M. Grzelczak, J. Vermant, E. M. Furst, L. M. Liz-marza, **2010**, *4*, 3591.

[226] E. Auyeung, T. I. N. G. Li, A. J. Senesi, A. L. Schmucker, B. C. Pals, M. O. De La Cruz, C. A. Mirkin, *Nature* **2014**, *505*, 73.

[227] L. Osinkina, S. Carretero-Palacios, J. Stehr, A. A. Lutich, F. Jäckel, J. Feldmann, *Nano Lett.* **2013**, *13*, 3140.

[228] D. Shi, C. Song, Q. Jiang, Z.-G. Wang, B. Ding, *Chem. Commun.* **2013**, *49*, 2533.

[229] D. H. M. Dam, H. Lee, R. C. Lee, K. H. Kim, N. L. Kelleher, T. W. Odom, *Bioconjug. Chem.* **2015**, *26*, 279.

[230] W. Wang, X. Ding, M. He, J. Wang, X. Lou, *Anal. Chem.* **2014**, *86*, 10186.

[231] J. Li, B. Zhu, X. Yao, Y. Zhang, Z. Zhu, S. Tu, S. Jia, R. Liu, H. Kang, C. J. Yang, *ACS Appl. Mater. Interfaces* **2014**, *6*, 16800.

[232] X. Zhang, M. R. Servos, J. Liu, *J. Am. Chem. Soc.* **2012**, *134*, 9910.

[233] X. Zhang, M. R. Servos, J. Liu, *Langmuir* **2012**, *28*, 3896.

[234] E. M. Nelson, L. J. Rothberg, *Langmuir* **2011**, *27*, 1770.

[235] H. Kimura-suda, D. Y. Petrovykh, M. J. Tarlov, L. J. Whitman, **2003**, *125*, 9014.

[236] H. D. Hill, J. E. Millstone, M. J. Banholzer, C. a. Mirkin, *ACS Nano* **2009**, *3*, 418.

[237] R. Gill, K. Göeken, V. Subramaniam, *Chem. Commun.* **2013**, *49*, 11400.

[238] J. W. Park, J. S. Shumaker-Parry, *J. Am. Chem. Soc.* **2014**, *136*, 1907.

[239] S. H. Brewer, W. R. Glomm, M. C. Johnson, M. K. Knag, S. Franzen, *Langmuir* **2005**, *21*, 9303.

[240] R. B. Martin, *J. Phys. Chem.* **1961**, *65*, 2053.

[241] W. D. Kumler, J. J. Eiler, *J. Am. Chem. Soc.* **1943**, *65*, 2355.

[242] V. Verdolino, R. Cammi, B. H. Munk, H. B. Schlegel, *J. Phys. Chem. B* **2008**, *112*, 16860.

[243] M. Borkowski, “ChemBuddy.com,” can be found under http://www.chembuddy.com, **2005**.

[244] S. M. E. Peters, M. W. J. Prins, P. Zijlstra, *Nanotechnology* **2015**, *27*, 24001.

[245] J. Becker, A. Trügler, A. Jakab, U. Hohenester, C. Sönnichsen, *Plasmonics* **2010**, *5*, 161.

[246] P. Guyot-Sionnest, *J. Phys. Chem. B* **2004**, *108*, 5882.

[247] M. M. Miller, A. A. Lazarides, *J. Phys. Chem. B* **2005**, *109*, 21556.

[248] T. J. Antosiewicz, M. Käll, *J. Phys. Chem. C* **2016**, *120*, 20692.

[249] A. C. Fogarty, A. C. Jones, P. J. Camp, *Phys. Chem. Chem. Phys.* **2011**, *13*, 3819.

[250] M. N. Berberan-Santos, E. N. Bodunov, B. Valeur, *Chem. Phys.* **2005**, *315*, 171.

[251] M. Abramowitz, S. Irene, **1970**, 470.

[252] J. N. Israelachvili, *Intermolecular and Surface Forces*, Elsevier, Amsterdam, **2011**.

[253] N. Arjmandi, W. Van Roy, L. Lagae, G. Borghs, **2012**, 1.

[254] E. L. C. J. Blundell, R. Vogel, M. Platt, *Langmuir* **2016**, *32*, 1082.

[255] X. Huang, I. H. El-Sayed, W. Qian, M. A. El-Sayed, *J. Am. Chem. Soc.* **2006**, *128*, 2115.

[256] D. Van Der Zwaag, N. Vanparijs, S. Wijnands, R. De Rycke, B. G. De Geest, L. Albertazzi, *ACS Appl. Mater. Interfaces* **2016**, *8*, 6391.

[257] R. Singh, J. W. Lillard, *Exp. Mol. Pathol.* **2009**, *86*, 215.

[258] R. Huschka, J. Zuloaga, M. W. Knight, L. V. Brown, P. Nordlander, N. J. Halas, *J. Am. Chem. Soc.* **2011**, *133*, 12247.

[259] A. M. Goodman, N. J. Hogan, S. Gottheim, C. Li, S. E. Clare, N. J. Halas, *ACS Nano* **2017**, *11*, 171.

[260] H. Wang, T. B. Huff, D. A. Zweifel, W. He, P. S. Low, A. Wei, J. X. Cheng, *Proc. Natl. Acad. Sci. U. S. A.* **2005**, *102*, 15752.

[261] K. E. Sapsford, W. R. Algar, L. Berti, K. B. Gemmill, B. J. Casey, E. Oh, M. H. Stewart, I. L. Medintz, *Chem. Rev.* **2013**, *113*, 1904.

[262] R. A. Sperling, W. J. Parak, *Philos. Trans. R. Soc. A Math. Phys. Eng. Sci.* **2010**, *368*, 1333.

[263] M. P. Monopoli, D. Walczyk, A. Campbell, G. Elia, I. Lynch, F. Baldelli Bombelli, K. A. Dawson, *J. Am. Chem. Soc.* **2011**, *133*, 2525.

[264] R. Oliveira-Silva, M. Sousa-Jerónimo, D. Botequim, N. J. O. Silva, D. M. F. Prazeres, P. M. R. Paulo, *Nanomaterials* **2019**, *9*, 893.

[265] S. Ritz, S. Schöttler, N. Kotman, G. Baier, A. Musyanovych, J. Kuharev, K. Landfester, H. Schild, O. Jahn, S. Tenzer, V. Mailänder, *Biomacromolecules* **2015**, *16*, 1311.

[266] A. M. Clemments, P. Botella, C. C. Landry, *ACS Appl. Mater. Interfaces* **2015**, *7*, 21682.

[267] N. A. Belsey, A. G. Shard, C. Minelli, *Biointerphases* **2015**, *10*, 019012.

[268] C. Y. Lee, P. Gong, G. M. Harbers, D. W. Grainger, D. G. Castner, L. J. Gamble, *Anal. Chem.* **2006**, *78*, 3316.

[269] M. D. Torelli, R. A. Putans, Y. Tan, S. E. Lohse, C. J. Murphy, R. J. Hamers, *ACS Appl. Mater. Interfaces* **2015**, *7*, 1720.

[270] A. Rafati, A. G. Shard, D. G. Castner, *Biointerphases* **2016**, *11*, 04B304.

[271] J. M. Rabanel, V. Adibnia, S. F. Tehrani, S. Sanche, P. Hildgen, X. Banquy, C. Ramassamy, *Nanoscale* **2019**, *11*, 383.

[272] P. M. Kelly, C. Åberg, E. Polo, A. O'Connell, J. Cookman, J. Fallon, Ž. Krpetić, K. A. Dawson, *Nat. Nanotechnol.* **2015**, *10*, 472.

[273] H. Hinterwirth, S. Kappel, T. Waitz, T. Prohaska, W. Lindner, M.

Lämmerhofer, *ACS Nano* **2013**, *7*, 1129.

[274] M. Choël, K. Deboudt, J. Osán, P. Flament, R. Van Grisken, *Anal. Chem.* **2005**, *77*, 5686.

[275] M. J. Eller, K. Chandra, E. E. Coughlin, T. W. Odom, E. A. Schweikert, *Anal. Chem.* **2019**, *91*, 5566.

[276] M. Horáček, R. E. Armstrong, P. Zijlstra, *Langmuir* **2018**, *34*, 131.

[277] L. Belfiore, L. M. Spenkelink, M. Ranson, A. M. van Oijen, K. L. Vine, *J. Control. Release* **2018**, *278*, 80.

[278] S. Dominguez-medina, L. Kisley, Δ. L. J. Tauzin, A. Hoggard, B. Shuang, A. S. D. S. Indrasekara, S. Chen, L. Wang, P. J. Derry, A. Liopo, E. R. Zubarev, C. F. Landes, S. Link, **2016**, DOI 10.1021/acsnano.5b06439.

[279] A. M. Clemments, P. Botella, C. C. Landry, *J. Am. Chem. Soc.* **2017**, *139*, 3978.

[280] X. Cheng, T. P. Anthony, C. A. West, Z. Hu, V. Sundaresan, A. J. McLeod, D. J. Masiello, K. A. Willets, *J. Phys. Chem. Lett.* **2019**, *10*, 1394.

[281] K. L. Blythe, E. J. Titus, K. A. Willets, *J. Phys. Chem. C* **2015**, *119*, 28099.

[282] N. Feiner-Gracia, M. Beck, S. Pujals, S. Tosi, T. Mandal, C. Buske, M. Linden, L. Albertazzi, *Small* **2017**, *13*, 1.

[283] T. Patiño, N. Feiner-Gracia, X. Arqué, A. Miguel-López, A. Jannasch, T. Stumpp, E. Schäffer, L. Albertazzi, S. Sánchez, *J. Am. Chem. Soc.* **2018**, *140*, 7896.

[284] R. Jungmann, M. S. Avendaño, M. Dai, J. B. Woehrstein, S. S. Agasti, Z. Feiger, A. Rodal, P. Yin, *Nat. Methods* **2016**, *13*, 439.

[285] P. Delcanale, B. Miret-Ontiveros, M. Arista-Romero, S. Pujals, L. Albertazzi, *ACS Nano* **2018**, *12*, 7629.

[286] R. Jungmann, C. Steinhauer, M. Scheible, A. Kuzyk, P. Tinnefeld, F. C. Simmel, *Nano Lett.* **2010**, *10*, 4756.

[287] I. Ament, J. Prasad, A. Henkel, S. Schmachtel, C. Sönnichsen, *Nano Lett.* **2012**, *12*, 1092.

[288] E. Wertz, B. P. Isaacoff, J. D. Flynn, J. S. Biteen, *Nano Lett.* **2015**, *15*, 2662.

[289] K. L. Blythe, K. A. Willets, *J. Phys. Chem. C* **2016**, *120*, 803.

[290] B. Fu, B. P. Isaacoff, J. S. Biteen, *ACS Nano* **2017**, *11*, 8978.

[291] M. Raab, C. Vietz, F. D. Stefani, G. P. Acuna, P. Tinnefeld, *Nat. Commun.* **2017**, *8*, 1.

[292] K. I. Mortensen, L. S. Churchman, J. A. Spudich, H. Flyvbjerg, *Nat. Methods* **2010**, *7*, 377.

[293] D. L. Mack, E. Cortés, V. Giannini, P. Török, T. Roschuk, S. A. Maier, *Nat. Commun.* **2017**, *8*, DOI 10.1038/ncomms14513.

[294] A. S. De Silva Indrasekara, B. Shuang, F. Hollenhorst, B. S. Hoener, A. Hoggard, S. Chen, E. Villarreal, Y. Y. Cai, L. Kisley, P. J. Derry, W. S. Chang, E. R. Zubarev, E. Ringe, S. Link, C. F. Landes, *J. Phys. Chem. Lett.* **2017**, *8*, 299.

[295] A. Taylor, R. Verhoef, M. Beuwer, Y. Wang, P. Zijlstra, *J. Phys. Chem. C* **2018**, *122*, 2336.

[296] L. Saemisch, M. Liebel, N. van Hulst, **2019**.

[297] B. Pérez-López, A. Merkoçi, *Anal. Bioanal. Chem.* **2011**, *399*, 1577.

[298] F. Li, H. Zhang, B. Dever, X. F. Li, X. C. Le, *Bioconjug. Chem.* **2013**, *24*, 1790.

[299] S. Enoki, R. Iino, Y. Niitani, Y. Minagawa, M. Tomishige, H. Noji, *Anal. Chem.* **2015**, *87*, 2079.

[300] M. Garai, T. Zhang, N. Gao, H. Zhu, Q. H. Xu, *J. Phys. Chem. C* **2016**, *120*, 11621.

[301] T. Förster, *Delocalization Excitation and Excitation Transfer*, TN (United States), Oak Ridge, **1965**.

[302] P. K. Jain, W. Huang, M. A. El-Sayed, *Nano Lett.* **2007**, *7*, 2080.

[303] O. Kratky, G. Porod, *Rec. Trav. Chim. Pays-Bas* **1949**, *68*, 1106.

[304] E. W. A. Visser, *Biosensing Based on Tethered Particle Motion*, Eindhoven University Of Technology, Eindhoven, **2017**.

[305] S. Geggier, A. Kotlyar, A. Vologodskii, *Nucleic Acids Res.* **2011**, *39*, 1419.

[306] M. C. Murphy, I. Rasnik, W. Cheng, T. M. Lohman, T. Ha, *Biophys. J.* **2004**, *86*, 2530.

[307] D. Garcia, *Comput. Stat. Data Anal.* **2010**, *54*, 1167.

[308] M. P. Allen, D. J. Tildesley, *Computer Simulation of Liquids*, Oxford University Press, Oxford, **1993**.

[309] Schott, “Optical Glass: Data Sheets,” can be found under https://www.schott.com/d/advanced_optics/ac85c64c- 60a0-4113-a9df-23ee1be20428/1.3/schott-optical-glass-collection-datasheets-english-17012017.pdf, **2016**.

[310] D. S. Terry, R. A. Kolster, M. Quick, M. V. LeVine, G. Khelashvili, Z. Zhou, H. Weinstein, J. A. Javitch, S. C. Blanchard, *Nat. Commun.* **2018**, *9*, DOI 10.1038/s41467-017-02202-y.

[311] K. K. Q. Nguyen, Y. K. Gomez, M. Bakhom, A. Radcliffe, L. PLa, D. Rochelle, J. W. Lee, E. J. Sorin, *Nucleic Acids Res.* **2017**, *45*, 4893.

[312] E. W. A. Visser, J. Yan, L. J. Van IJzendoorn, M. W. J. Prins, *Nat. Commun.* **2018**, *9*, 1.

[313] S. A. McKinney, C. Joo, T. Ha, *Biophys. J.* **2006**, *91*, 1941.

[314] S. R. Eddy, *Curr. Opin. Struct. Biol.* **1996**, *6*, 361.

[315] L. R. Rabiner, B. H. Juang, *IEEE ASSP Mag.* **1986**, *3*, 4.

[316] P. Zijlstra, P. M. R. Paulo, K. Yu, Q. H. Xu, M. Orrit, *Angew. Chemie - Int. Ed.* **2012**, *51*, 8352.

[317] S. J. Zhen, C. Z. Huang, J. Wang, Y. F. Li, *J. Phys. Chem. C* **2009**, *113*, 21543.

[318] S. R. Beeram, F. P. Zamborini, *J. Am. Chem. Soc.* **2009**, *131*, 11689.

[319] E. Cortés, W. Xie, J. Cambiasso, A. S. Jermyn, R. Sundararaman, P. Narang, S. Schlücker, S. A. Maier, *Nat. Commun.* **2017**, *8*, 1.

[320] J. Lahiri, L. Isaacs, B. Grzybowski, J. D. Carbeck, G. M. Whitesides, *Langmuir* **2002**, *15*, 7186.

[321] P. Harder, M. Grunze, R. Dahint, G. M. Whitesides, P. E. Laibinis, *J. Phys. Chem. B* **2002**, *102*, 426.

[322] E. Ostuni, R. G. Chapman, R. E. Holmlin, S. Takayama, G. M. Whitesides, *Langmuir* **2001**, *17*, 5605.

[323] H. He, C. Gao, *Curr. Org. Chem.* **2012**, *15*, 3667.

[324] D. A. Fleming, C. J. Thode, M. E. Williams, *Chem. Mater.* **2006**, *18*, 2327.

[325] H. Ismaili, A. Alizadeh, K. E. Snell, M. S. Workentin, *Can. J. Chem.* **2009**, *87*, 1708.

[326] J. L. Brennan, T. R. Tshikhudo, M. Brust, N. S. Hatzakis, R. J. M. Nolte, A. E. Rowan, N. Dirvianskyte, V. Razumas, S. Patkar, J. Vind, A. Svendsen, *Bioconjug. Chem.* **2006**, *17*, 1373.

[327] C. J. Thode, M. E. Williams, *J. Colloid Interface Sci.* **2008**, *320*, 346.

[328] J. M. Eeftens, J. van der Torre, D. R. Burnham, C. Dekker, *BMC Biophys.* **2015**, *8*, 1.

[329] M. F. Debets, S. S. Van Berkel, S. Schoffelen, F. P. J. T. Rutjes, J. C. M. Van Hest, F. L. Van Delft, *Chem. Commun.* **2010**, *46*, 97.

[330] P. Blumhardt, J. Stein, J. Mücksch, F. Stehr, J. Bauer, R. Jungmann, P. Schwille, *Molecules* **2018**, *23*, 1.

[331] IDT, “IDT Integrated DNA Technologies,” can be found under https://eu.idtdna.com/calc/analyzer, **2019**.

[332] H. T. Allawi, J. Santalucia, *Biochemistry* **1997**, *36*, 10581.

[333] L. Deng, M. Mrksich, G. M. Whitesides, **1996**, *7863*, 12009.

[334] R. E. Holmlin, X. Chen, R. G. Chapman, S. Takayama, G. M. Whitesides, **2001**, 2841.

[335] C. Huang, L. Wang, J. Shyue, Y. Chang, **2014**.

[336] G. Zheng, S. Liu, J. Zha, P. Zhang, X. Xu, Y. Chen, S. Jiang, **2018**, DOI 10.1021/acs.langmuir.8b02001.

[337] Y. Zhang, Y. Liu, B. Ren, D. Zhang, S. Xie, Y. Chang, J. Yang, J. Wu, L. Xu, J. Zheng, *IOP Publ.* **2019**, *'Accepted.*

[338] K. Salaita, Y. Wang, C. A. Mirkin, *Nat. Nanotechnol.* **2007**, *2*, 145.

[339] K. B. Lee, S. J. Park, C. A. Mirkin, J. C. Smith, M. Mrksich, *Science (80-.).* **2002**, *295*, 1702.

[340] V. Gatterdam, A. Frutiger, K. P. Stengele, D. Heindl, T. Lübbers, J. Vörös, C. Fattinger, *Nat. Nanotechnol.* **2017**, *12*, 1089.

[341] G. González-rubio, P. Díaz-núñez, A. Rivera, A. Prada, G. Tardajos, J. González-izquierdo, L. Bañares, P. Llombart, L. G. Macdowell, M. A. Palafox, L. M. Liz-marzán, **2017**, *644*, 640.

[342] D. Pablo, G. González-rubio, A. Prada, J. Gonzalez, A. Rivera, L. Banares, A. Guerrero-martínez, O. Peña-rodríguez, **2018**, DOI 10.1021/acs.jpcc.8b06375.

[343] R. A. Hughes, E. Menumerov, S. Neretina, *Nanotechnology* **2017**, *28*, DOI 10.1088/1361-6528/aa77ce.

[344] S. L. Westcott, J. B. Jackson, C. Radloff, N. J. Halas, *Phys. Rev. B - Condens. Matter Mater. Phys.* **2002**, *66*, 1.

[345] M. Bosman, L. Zhang, H. Duan, S. F. Tan, C. A. Nijhuis, C. W. Qiu, J. K. W. Yang, *Sci. Rep.* **2014**, *4*, 1.

[346] J. F. Beausang, P. C. Nelson, *Phys. Biol.* **2007**, *4*, 205.

[347] J. F. Beausang, P. C. Nelson, *Phys. Biol.* **2007**, *4*, 205.

[348] N. Celik, F. O'Brien, S. Brennan, R. D. Rainbow, C. Dart, Y. Zheng, F. Coenen, R. Barrett-Jolley, *Commun. Biol.* **2020**, *3*, DOI 10.1038/s42003-019-0729-3.

[349] D. E. Segall, P. C. Nelson, R. Phillips, *Phys. Rev. Lett.* **2006**, *96*, 1.

[350] T. E. Cheatham III, P. A. Kollman, *Annu. Rev. Phys. Chem.* **2000**, *51*, 435.

[351] M. De Vivo, M. Masetti, G. Bottegoni, A. Cavalli, *J. Med. Chem.* **2016**, *59*, 4035.

[352] S. F. E. M. Doi, *The Theory of Polymer Dynamics*, Clarendon Press, Oxford, **1998**.

[353] R. R. Netz, D. Andelman, *Phys. Rep.* **2003**, *380*, 1.

[354] W. R. S. W. B. Russel, D. A. Saville, *Colloidal Dispersions*, Cambridge

University Press, Cambridge, **1989**.

[355] B. H. Zimm, *J. Chem. Phys.* **1956**, *24*, 269.

9 APPENDICES

APPENDIX 1: CORE-SHELL MIE-GANZ MODEL 127

APPENDIX 2: ESTIMATION OF MAXIMUM LOADING OF NANOPARTICLES 129

APPENDIX 1: CORE-SHELL MIE-GANS MODEL

A small metal nanoparticle in an electromagnetic field can be approximated as an oscillating dipole. This results in absorption and scattering of the incident light that can be highly enhanced when a plasmon resonance is excited. Both, the scattering and the absorption, can be relatively simply calculated for particles much smaller than the wavelength of the incident light by Mie-Gans theory.

Due to the binding of molecules the refractive index surrounding the gold nanorod changes, inducing a shift of the plasmon resonance. We assume an effective medium approach in which these molecules establish a shell of finite thickness around the nanorod. The metallic nanoparticle surrounded by a shell can be modelled using a modified Mie-Gans theory that treats core-shell particles.[246] The material of the nanoparticle is determined by the dielectric function $\varepsilon(\omega)$, where Johnson and Christy's data for gold are used,[138] and the particle is immersed in water with a frequency-independent dielectric function $\varepsilon_m = 1.77$. The shell is modelled as an ellipsoid extending the core metallic nanoparticle characterized by its thickness s and frequency-independent dielectric function ε_s The polarizability of the core-shell metallic ellipsoid's longitudinal plasmon is: [246]

$$\alpha(\omega) = \varepsilon_0 V_p \cdot \frac{(\varepsilon_s - \varepsilon_m)\left[\varepsilon_s + (\varepsilon(\omega) - \varepsilon_s)\left(L_p - \frac{V_p}{V_s} L_s\right)\right] + \frac{V_p}{V_s}\varepsilon_s(\varepsilon(\omega) - \varepsilon_s)}{\left[\varepsilon_s + (\varepsilon(\omega) - \varepsilon_s)\left(L_p - \frac{V_p}{V_s} L_s\right)\right][\varepsilon_m + (\varepsilon_s - \varepsilon_m)L_s] + \frac{V_p}{V_s} L_s\, \varepsilon_s(\varepsilon(\omega) - \varepsilon_s)} \tag{9.1}$$

with L_p the depolarization factor of the metallic particle core and L_s the depolarization factor of the whole particle, which are both characterized by their own eccentricities. V_p is the volume of the metallic nanoparticle core and V_s is the volume of the shell spheroid.

Calculation of expected distribution of plasmon shifts

The magenta histogram in Figure 3.5b in the main text is calculated by evaluating the scattering cross section for a set of particle-dimensions ($n = 215$) extracted from TEM measurements. By taking the exact dimensions found in TEM images we estimate the contribution of the size dispersion to the plasmon shift. We calculated the expected shift by considering an index matched shell ($\varepsilon_s = 1.77$), and subsequently a shell with an increased dielectric function due to the presence of ssDNA. The thickness of the shell s was determined by treating the ssDNA molecule as a worm-like chain[352] giving $s = 11$ nm for our 50 nt sequence. The dielectric function of the shell is used as a fitting parameter to match the experimental results. We find an only slightly increased dielectric function for the shell ($\varepsilon_s = 1.90$), which indicates a hydrated and non-close-packed ssDNA shell. In line with the experiments, only particles that exhibit a plasmon wavelength in the range of 670 nm – 890 nm are analysed. Note that this effective medium approach neglects any higher order corrections originating from heterogeneity in ssDNA conformation.

Calculation of the expected distribution of initial rates

The magenta histogram of initial rates shown in Figure 3.9 is calculated by again evaluating the scattering spectra for particles immersed in water with an empty shell, followed by calculation of the spectra of the same particle with a shell with dielectric constant $\varepsilon_s = 1.80$. These two spectra are then assigned to time $t = 0$ s and $t = 1$ s, respectively, and the rate at which the plasmon shifts is then extracted in the same way as in the experiment, however here only from two data points. This approach takes into account that the rate at which the plasmon shifts depends on the geometry of the particle due to variations in refractive index sensitivity. Note that this yields a distribution of normalized rate constants that are then multiplied by a constant to match the average measured rate constant.

Limitations of the model

However, some remarks should be made for applying the core-shell Mie-Gans model to simulate the optical properties of the gold nanorods and the binding events. The model holds only for particles much smaller than the wavelength of light. The nanorods which are used in the experiments have dimensions around (70 nm - 20 nm), having an equivalent volume of a sphere of 60 nm in diameter. Furthermore, the rods are approximated by ellipsoids, which causes deviations of their scattering cross sections due to both the shape approximation and the reduction in volume of particles. Moreover, the nanorods in the experiments are immobilized on a glass coverslip, thus ssDNA cannot bind to the bottom of the nanorod. Because of those deviations the absolute plasmon peak positions as well as the absolute scattering cross sections will differ from the experiments. However, the plasmon shifts and their distribution will be comparable to the experimental situation.

APPENDIX 2: ESTIMATION OF MAXIMUM LOADING OF NANOPARTICLES

To be able to understand the process of gold nanoparticle functionalization with ssDNA we develop an estimate of the maximal molecular loading of employed particles. We based ourselves on the work by Hill et al.[236] and consider thiolated DNA molecules as closely-packed cones occupying the space around a particle. A simplified sketch of the system geometry is depicted in Figure 9.1a with all important variables specifically marked. Based on TEM measurements we assume our nanorods to be spherically capped cylinders neglecting any surface irregularities. Since the particle functionalization with ssDNA is performed at high ionic strength (I = 1000 mM) where ssDNA adopts "mushroom-like" conformation, we approximate ssDNA by a sphere with its hydrodynamic radius $R_{\mathrm{H}} = R_{\mathrm{DNA}}$.

To get the maximal amount of molecular spheres which could fit around a nanorod we calculate the surface area of a layer distant R_{DNA} from the nanorod surface and divide this by the molecular footprint on the layer ($A_{\mathrm{DNA}} \approx \pi R_{\mathrm{DNA}}^2$). For the case of particles immobilized on a substrate their significant part of surface area is shielded from molecular binding. We correct for this effect by finding the minimal angle α:

$$\alpha = \cos^{-1}\left(\frac{d - 2R_{\mathrm{DNA}}}{d + 2R_{\mathrm{DNA}}}\right) - \frac{\varphi}{2} \quad , \quad \varphi = 2\sin^{-1}\left(\frac{2R_{\mathrm{DNA}}}{d + 2R_{\mathrm{DNA}}}\right), \qquad 9.2$$

marking the inaccessible space, and discard the corresponding particle's surface area. The geometrical derivations lead to a following expression for maximal number of molecules on the surface a nanorod:

$$N_{\mathrm{max}} = \frac{(d + 2R_{\mathrm{DNA}})^2}{R_{\mathrm{DNA}}^2}\frac{(1 + \cos\alpha)}{2} + \frac{(d + 2R_{\mathrm{DNA}})(h - d)}{R_{\mathrm{DNA}}^2}\frac{(\pi - \alpha)}{\pi}. \qquad 9.3$$

The Eqn. 9.3 clearly shows that particle loading is dependent on two parameters: the particle dimensions and the size of employed molecule. We obtained diameters and height of our nanorod using TEM in previous section. However, a reliable estimate of molecular size for employed ssDNA is required. Single stranded DNA consists of individual nucleotides connected together through a phosphate backbone via flexible covalent bonds. This makes ssDNA an ideal candidate to be modeled using worm-like chain model.[352] In this model a polymer is considered to consist of n solid segments of which movement is allowed due to flexible linkers. In such case the measure of polymer length is the contour length $L_n = nl_{\mathrm{b}}$ which is the distance between the chain ends measured along the helical axis for each segment of length length l_{b} (for ssDNA $l_{\mathrm{b}} = 0.63$ nm[304]). However the practical insight into the molecular size is given by the end-to-end length R_n which is the vector sum of each segment length[352]

$$\langle R_n^2 \rangle = 2P\left(L_n - P + Pe^{-\frac{L_n}{P}}\right), \tag{9.4}$$

where P is the persistence length of the molecule. Since we deal with charged polymer we correct the persistence length for electrostatic charges[353]

$$P \cong P_0 + P_{\mathrm{OSF}} = P_0 + \frac{\lambda_{\mathrm{B}} f}{4\kappa^2}, \tag{9.5}$$

where P_0 is the bare persistence length (for ssDNA $P_0 \approx 2$ nm[304]), and $\lambda_{\mathrm{B}} = e^2/4\pi\varepsilon_{\mathrm{r}}\varepsilon_0 k_{\mathrm{B}}T$ is the Bjerrum length at which the electrostatic interaction between two point charges e is equal to the thermal energy $k_{\mathrm{B}}T$, and $f = z/l_{\mathrm{b}}$ is the fractional number of charges per segment length. Here, for the case of ssDNA $z = 1$ corresponding to one charge per nucleotide. The Debye length κ is the length at which salt ions screen the electric field, and for a monovalent electrolyte as i.e. NaCl is defined as:[354]

$$\frac{1}{\kappa} = \sqrt{\frac{\varepsilon_{\mathrm{r}}\varepsilon_0 k_{\mathrm{B}}T}{2N_{\mathrm{A}}e^2 I}}. \tag{9.6}$$

Here, ε_0 is the permittivity of vacuum, ε_{r} is the relative permittivity of the liquid (for water $\varepsilon_{\mathrm{r}} = 78.3$), k_{B} is the Boltzmann constant, T the temperature (here we consider $T = 298$ K), N_{A} the Avogadro constant and I is the ionic strength of the liquid.

The model shows that for low ionic strength the electrostatic interaction play significant role and extend the molecules in a stretched form characterized by long end-to-end distance. However, for the case of high ionic strength ($I > 100$ mM) the ions in the solution effectively shield the electrostatic repulsions between individual polymer segments reducing the end-to-end distance giving molecule a "mushroom-like" conformation. We approximate this complex shape by a hard sphere characterized by its hydrodynamic radius $R_{\mathrm{H}} = R_{\mathrm{DNA}}$ since this allows us to include electrostatic[353] and hydrodynamic[355] interactions. The diffusion coefficient D of such sphere is defined by Stokes-Einstein equation:[252]

$$D = \frac{k_{\mathrm{B}}T}{6\pi\eta_0 R_{\mathrm{DNA}}}. \tag{9.7}$$

and the diffusion coefficient of flexible polymers in dilute solutions is then given by the Zimm model:[355]

$$D = \frac{8k_{\mathrm{B}}T}{3\sqrt{6\pi^3}\eta_0 R_n}. \tag{9.8}$$

where η_0 is the viscosity of water $\eta_0 = 8.9 \cdot 10^{-4}\ \mathrm{Pa \cdot s}$ at $T = 298$ K). The Eqn. 9.7 and Eqn. 9.8 result in the expression for the molecular radius:

$$R_{\mathrm{DNA}} = \frac{3\sqrt{\pi}}{8\sqrt{6}} R_n \cong 0.271 R_n \,. \qquad 9.9$$

We directly recalculate the molecular radius to ssDNA footprint for 30 nt long molecule and 1000 mM of buffer ionic strength and obtain $A_{\mathrm{DNA}} \approx 16\ \mathrm{nm}^2$ matching well the literature.[236] We further test our model against experimental results for ensemble measurements of ssDNA binding to gold spheres published by Hill et al.[236] and find an excellent match (Figure 9.1b). Note, that here we did not assume shielding by a present substrate. Having the confidence about reliability of our model we determine the maximal molecular loading for all nanorods measured with TEM. In Figure 9.1c we obtain a „normal-like“ distribution of number of molecules over individual particles of $N_{\max} = 338 \pm 85$ characterized by a relative spread of 25 % owing to the size distribution of the sample that leads to a distribution of surface areas available for binding.

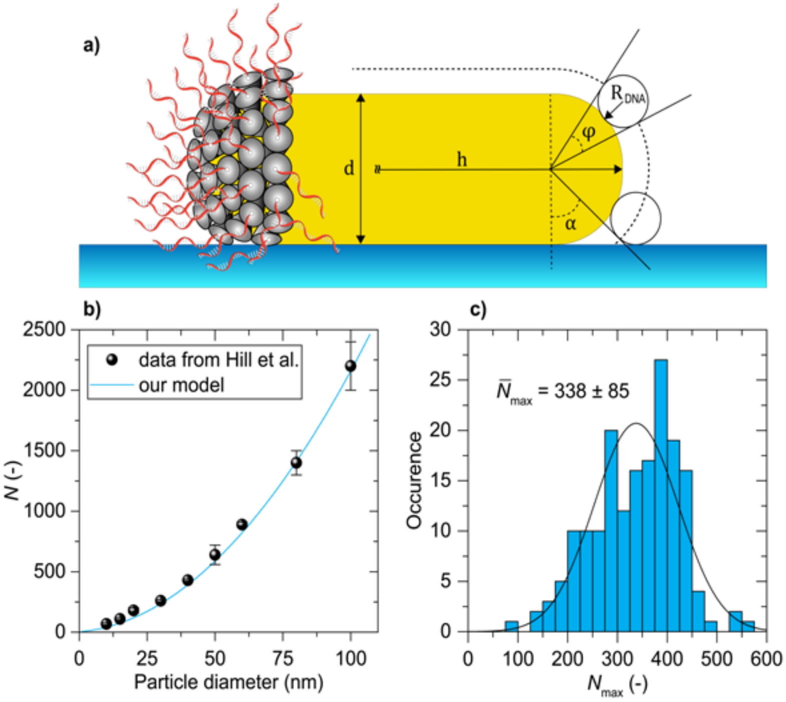

Figure 9.1: a) Illustration of conical representation of thiolated ssDNA bounded to a nanoparticle with specified geometry of the system. **b)** Testing our model against experimental data for ssDNA functionalization of gold spheres measured by Hill et al.[236] In this case we do not assume the presence of a substrate. **c)** Histogram of maximal number of ssDNA molecules on individual gold nanorods for dimensions measured by TEM.

LIST OF PUBLICATIONS

1. “Heterogeneous kinetics in the functionalization of single plasmonic nanoparticles”, Horáček, M., Armstrong, R.E., Zijlstra, P., Langmuir **2018**, 34, 131-138.
   DOI: 10.1021/acs.langmuir.7b04027

2. "Plasmon Rulers as a Probe for Real-Time Microsecond Conformational Dynamics of Single Molecules", Visser, E.W.A., Horáček, M., Zijlstra, P., Nano Letters **2018**, 18, 7927–7934.
   DOI: 10.1021/acs.nanolett.8b03860

3. "Dynamic single-molecule counting for the quantification and optimization of nanoparticle functionalization protocols", Horáček, M., Engels, D.J., Zijlstra, P., Nanoscale **2020**, 12, 4128-4136.
   DOI: 10.1039/C9NR10218C

4. "Plasmonic Assemblies for Real-time Single-molecule Sensing", Armstrong, R.E., Horáček, M., Zijlstra, P., Small **2020**, submitted.
   DOI: -

5. "Strong Plasmon-enhancement of the Saturation Photon Count Rate of Single Molecules", Wang, Y., Horáček, M., Zijlstra, P., J. Phys. Chem. Lett. **2020**, 11, 1962-1969.
   DOI: 10.1021/acs.jpclett.0c00155

CURRICULUM VITAE

Matěj Horáček was born on 20th of August 1991 in Vyškov in what is today called Czech Republic. He is a proud citizen of his home village Hrušky. Matěj studied high school in Brno at Gymnázium Elgartova, where he followed general education with emphasis on Mathematics and Physics.

In 2010 Matěj started his bachelor studies at Brno University of Technology (BUT), Faculty of Mechanical Engineering, Institute of Physical Engineering focusing on Applied Physics and Physical Engineering. He graduated with honours ('cum laude') in 2013 with bachelor thesis "Design of the atomic source producing carbon beams for deposition of graphene in UHV conditions".

Matěj continued with his master studies at the same institute at BUT focusing on Applied Physics. During the master studies Matěj visited Eindhoven twice (2014, and 2015) to work at Eindhoven University of Technology (TU/e) on Erasmus project "Graphene solar cell based on plasmonics" supervised by Dr. Kees Flipse and Dr. Peter Zijlstra. The results obtained during his time in Eindhoven were used for Matěj's master thesis "Graphene photodetector based on plasmonic effects" which Matěj defended with honours ('cum laude') in June 2015 under supervision of Prof. Dr. Tomáš Šikola.

In September 2015, Matěj moved to Eindhoven where he started his PhD in the group of Molecular Biosensing for Medical Diagnostics (MBx) under the supervision of Dr. Peter Zijlstra and Prof. Dr. Menno Prins. During his PhD Matěj worked on the development of a new type of molecular ruler based on plasmonic nanoparticles and a hybridization of their plasmons. In 2016 he received the Onderwijsprijs from the student education organization (STOOR) as the best supervisor for second year bachelor students. The main results of the work during Matěj's PhD are summarized in this thesis.

ACKNOWLEDGEMENTS

This long journey has come to its end. I'd like to dedicate this section of my thesis to express my gratitude to all people who helped me and influenced me along the way. Further, I'd like to thank here all committee members for excepting my proposal to be part of my PhD committee, for taking their time to read my thesis and for a critical feedback I'll surely get during the defense.

First of all, I'd like to express my deepest gratitude to you, Peter. Years ago you gave me the opportunity to work on such exciting project. I still remember when I asked you about your open positions during a borrel back in spring 2015, and after a proper meeting we could start to work! It has been a great journey of my professional development and you guided me through the whole process. You always critically approached me and discussed my drawbacks allowing me to grow, and also helped me during my lows. Thank you for all your patience, help and input for my overall research, my articles, and especially for this thesis. I wish you all success and luck to achieve your research and personal goals!

Further I'd like to thank Menno for all his support and warm welcoming in MBx group. I was always looking forward for your questions during my talks at group meetings and I am very much grateful for all your input into my research work. You kept my moral up when I needed it most, I truly appreciate it.

Next, I thank the rest of MBx stuff - Leo, Arthur, Lorentzo, Khulan - thank you so much for all productive discussions during or outside group meetings, for all your questions making me think and your feedback to my work. I'd like to especially thank to Claudia, the MBx mother figure, for all her kind help, for keeping the facilities in excellent conditions, and for our "stealthy" gossiping. You guys, have no idea how many things we actually know!

I'd like to acknowledge the entire "old gang" who welcome me so warmly to the group, taught me how to work in chemical lab, and gave me so many tips and experiences. It was a blast being with you, thank you, Fabiola, Stefano, Christian and Roland. Particularly thank you, Emiel, for all support you've been giving me over last years. It was a great experience to work with you on Chapter 5 of this thesis, I learnt so much from you during this time. You are the true friend, as well as Markéta, thank you, guys. You helped me to adapt in new country, comforted me when I needed it, and forced me to take some breaks from time to time. I wish you all best with your lives and with your future careers.

With many of you I have worked for almost whole four and half years - Junhong, Adam, Michael, Rachel, Max and Yuyang. I'd like to thank Junhong for our discussions in the chemical lab about literally everything, and Adam for his help and pushing my buttons with his cleaning habits in chemical lab. Thank you, Michael, for all cooperation on scripts and setup, discussions about sport and for an insight into the running world (still not willing to run though!). Thank you, Rachel, for all help you've been giving me, you are great friend! We discussed our work practically every day and I truly believe that without your help my PhD would take a year longer. We could always talk about daily stuff and also complain about the work stuff together, I’ve always appreciated that. Speaking of Rachel, I'd like to acknowledge all insane people (Emiel, Junhong, Marianna, Michael, Khulan and many others) and her especially for organizing the insanity workout sessions.

Thank you, Yuyang and Max! We had started our PhD projects together at the same day being just three young little scared perspective scientists, and few years later, while being just scientists, we finished practically at the same week. How amazing is that?! You've been the best comrades I could wish for. Good luck with your following careers and your lives!

Next, I'd like to thank all the "youngsters", people who started to work in our group later during my project. Thank you, Rafiq, Natalia, Laura W., Roger, Mannos, Tina, Paul, Joost, Willeke, Adrianna, Sjoerd, Max, Stein, Maartje, Rosan, Judith, Annabel, Laura v/S. and Alissa, for all the great time, interesting conversations, help, and fun. I wish you good luck with your projects! Special thanks then go to Rui, who visited our group just temporarily because he's from Portugal, as we all know. Deepest thanks for all your support, keep waving, bro!

Further I'd like to thank all students I supervised for their help with my project - Vojtěch, Willemijn, Frank. I thank to Linde for your work on the core-shell Mie-Ganz model, and especially thank to Dion for all discussions dealing with DNA-PAINT, for your absolutely independent experimental work, and your hell of contribution to the theoretical qPAINT model.

There are also many people I’ve met during my time in Eindhoven who I didn't directly worked with, but their presence, help and friendship have influenced me significantly. Thank you Hjůí, Marianna, Calvin, Peťo, Filip, Samo, Nuno, Andrey, Igor, Seva, Kees, Harm, Mohamed, Marco, Wijnand, Imre, Karel, and whole Midnight Mooners Eindhoven team!

Last, but not least, I'd like to express my deepest gratitute to my family in my mother language. Mami, Tati, Áďo, Kryštofe a Danko, Babi a oba Dědové, děkuju vám neskutečně moc za to, kam až jste mi pomohli se dostat. Bez vás bych to nikdy nemohl dokázat, bez vaší podpory, starosti o mě a vaší nekonečné lásky. I přes tu dálku jste tu byli vždy se mnou. Neuvěřitelně moc si toho vážím, mám vás všechny moc rád

Děkuju Ti, Terezo, za veškerou pomoc, kterou jsi mi během těch let dala. Navštěvovala jsi mě, kdy jsi mohla, a vždy ses snažila mi být nablízku. Za to Ti budu vždy vděčný.

… and I'd like to apologize, to you, lab-people, for all the crap I was singing the entire time in the lab!

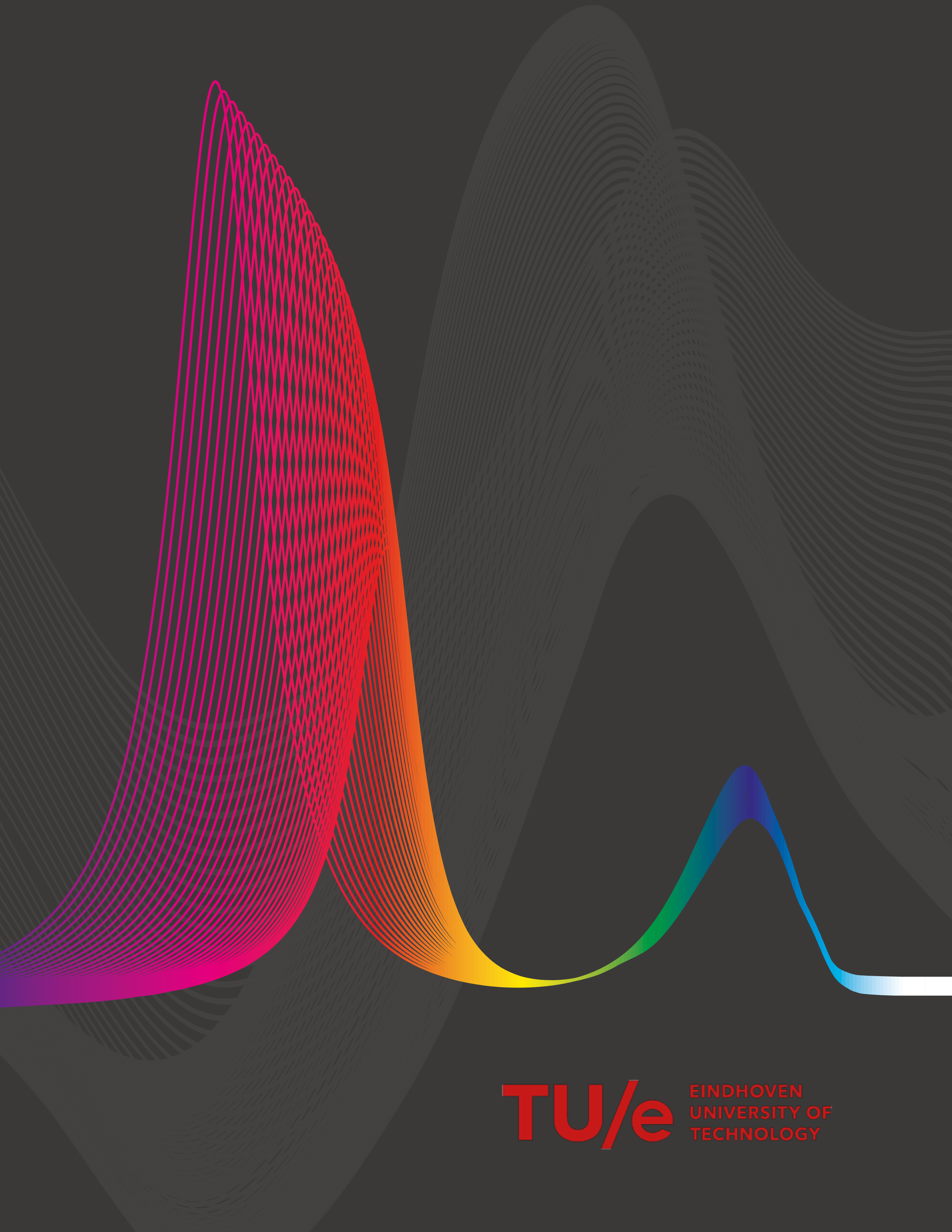

TU/e EINDHOVEN UNIVERSITY OF TECHNOLOGY